CIVIL ENGINEERING STUDIES
Illinois Center for Transportation Series No. 18-001
UILU-ENG-2018-2001
ISSN: 0197-9191

Repair & Strengthening of Distressed/Damaged Ends of Prestressed Beams with FRP Composites

Prepared By
Bassem Andrawes
Ian D. Shaw
Hang Zhao
University of Illinois at Urbana-Champaign

Research Report No. FHWA-ICT-18-001

A report of the findings of

ICT PROJECT R27-156
Repair & Strengthening of Distressed/Damaged Ends of Prestressed Beams with FRP Composites

Illinois Center for Transportation

February 2018

ILLINOIS CENTER FOR TRANSPORTATION

TECHNICAL REPORT DOCUMENTATION PAGE

1. Report No. FWHA-ICT-18-001	**2. Government Accession No.** N/A	**3. Recipient's Catalog No.** N/A
4. Title and Subtitle Repair & Strengthening of Distressed/Damaged Ends of Prestressed Beams with FRP Composites		**5. Report Date** February 2018 **6. Performing Organization Code** N/A
7. Author(s) Bassem Andrawes, Ian D. Shaw and Hang Zhao		**8. Performing Organization Report No.** ICT-18-001 UILU-ENG-2018-2001
9. Performing Organization Name and Address Illinois Center for Transportation Department of Civil and Environmental Engineering University of Illinois at Urbana-Champaign 205 North Mathews Avenue, MC-250 Urbana, IL 61801		**10. Work Unit No.** N/A **11. Contract or Grant No.** R27-156
12. Sponsoring Agency Name and Address Illinois Department of Transportation (SPR) Bureau of Research 126 East Ash Street Springfield, IL 62704		**13. Type of Report and Period Covered** Final Report November 1, 2014 – February 16, 2018 **14. Sponsoring Agency Code** FHWA

15. Supplementary Notes

Conducted in cooperation with the U.S. Department of Transportation, Federal Highway Administration.

16. Abstract

Over the past few decades, fiber reinforced polymer (FRP) composites have emerged as a lightweight and efficient material used for the repair and retrofit of concrete infrastructures. FRP can be applied to concrete as either externally bonded laminates or near-surface mounted (NSM) bars or plates. One problem afflicting bridge girders in cold climates is the deterioration of the girder ends due to deicing salt exposure, thus reducing their shear strength. This report presents the results of an Illinois Department of Transportation (IDOT) sponsored study to use FRP materials to repair and retrofit the damaged ends of prestressed concrete beams. In the first phase of the study, direct shear pull-out tests are performed on glass-FRP (GFRP) laminates, carbon-FRP (CFRP) laminates and NSM CFRP bars. An accelerated aging scheme consisting of freeze/thaw cycling in the presence of a deicing salt solution is implemented to determine the effects of long-term environmental exposure on the FRP/concrete interface. In the next phase, three-point bending tests are performed on small and full-scale prestressed concrete beams. End region deterioration is simulated by imposing damage to the concrete cover; then mortar and FRP repairs are applied to test their effectiveness. Finally, a 3D finite element (FE) model of a full-scale prestressed concrete (PC) I-girder is developed and used in a parametric study. The numerical study is performed by using externally bonded CFRP shear laminates to determine the most effective repair schemes for the damaged end region. The results of the shear pull-out tests of CFRP laminates that have undergone accelerated aging are used to calibrate a bond stress-slip model for the interface between the FRP and concrete substrate. The shear pull-out test results also help to approximate the reduced bond stress-slip properties associated with exposure to the environment that causes this type of end region damage. The results of this study indicate the effectiveness of FRP in repairing this type of damage. Based on the study's experimental results, a design method of FRP laminates is proposed for PC girders with damaged end regions.

17. Key Words Prestressed Concrete, Small and full-scale Girders, Bond Behavior, Accelerated aging, Pull-out tests, FRP	**18. Distribution Statement** No restrictions. This document is available through the National Technical Information Service, Springfield, VA 22161.		
19. Security Classif. (of this report) Unclassified	**20. Security Classif. (of this page)** Unclassified	**21. No. of Pages** 79 pp + appendices	**22. Price** N/A

Form DOT F 1700.7 (8-72) **Reproduction of completed page authorized**

ACKNOWLEDGMENT, DISCLAIMER, MANUFACTURERS’ NAMES

This publication is based on the results of **ICT-R27-156, Repair of Damaged End Regions of Prestressed Concrete Girders using Fiber Reinforced Polymer Composite Materials**. ICT-R27-156 was conducted in cooperation with the Illinois Center for Transportation; the Illinois Department of Transportation; and the U.S. Department of Transportation, Federal Highway Administration.

Members of the Technical Review panel were the following:

- Victor H. Veliz - Bureau of Bridges and Structures, IDOT
- Dan Brydl - FHWA
- Jeff Burke - Bureau of Bridges and Structures, IDOT
- Mark Eckhoff - District 4, IDOT
- Mahmoud Etemadi - District 2, IDOT
- Kevin Riechers - Bureau of Bridges and Structures, IDOT
- Mark Shaffer - Bureau of Bridges and Structures, IDOT
- Ryan Sheley - Bureau of Construction, IDOT
- Dan Tobias - Bureau of Materials and Physical Research, IDOT

EXECUTIVE SUMMARY

Over the past few decades, fiber reinforced polymer (FRP) composites have emerged as a lightweight and efficient material used for the repair and retrofit of concrete infrastructures. FRP can be applied to concrete as either externally bonded laminates or near-surface mounted (NSM) bars or plates. One problem afflicting bridge girders in cold climates is the deterioration of the girder ends due to deicing salt exposure, thus reducing their shear strength. This report presents the results of an Illinois Department of Transportation (IDOT) sponsored study to use FRP materials to repair and retrofit the damaged ends of prestressed concrete (PC) beams.

In the first phase of the study, direct shear pull-out tests are performed on glass-FRP (GFRP) laminates, carbon-FRP (CFRP) laminates and NSM bars. An accelerated aging scheme consisting of freeze/thaw cycling in the presence of a deicing salt solution is implemented to determine the effect of long-term environmental exposure on the FRP/concrete interface. In the next phase, three-point bending tests are performed on small and full-scale prestressed concrete beams. End region deterioration is simulated by imposing damage to the cover concrete; then mortar and FRP repairs are applied to test their effectiveness.

Finally, a 3D finite element (FE) model of a full-scale prestressed concrete I-girder is developed and used in a parametric study. The numerical study is performed by using externally bonded CFRP shear laminates to determine the most effective repair schemes for the damaged end region. The results of the shear pull-out tests of CFRP laminates that have undergone accelerated aging are used to calibrate a bond stress-slip model for the interface between the FRP and concrete substrate. The shear pull-out test results also help to approximate the reduced bond stress-slip properties associated with exposure to the environment that causes this type of end region damage.

The results of this study indicate the effectiveness of FRP in repairing this type of damage. Based on the study’s experimental results, a design method of FRP laminates is proposed for PC girders with damaged end regions.

TABLE OF CONTENTS

CHAPTER 1: INTRODUCTION

1.1 MOTIVATION FOR RESEARCH PROJECT

Much of the existing concrete infrastructure in the United States is near the end of its design life and needs to be replaced, rehabilitated, or repaired. Over 58,000 bridges have been deemed structurally deficient in 2016 (ARTBA 2016). Many of these structurally deficient bridges are located in the Northeast and Midwest, where harsh climates cause deterioration in concrete structures at an accelerated rate. One specific problem that plagues concrete bridge girders is the deterioration of girders' end regions. This deterioration is due to the failure of expansion joints, which allows water containing deicing salts to flow onto the girder ends. The normal freezing and thawing cycles of these saturated girder ends cause scaling and spalling of the cover concrete. This can directly expose the steel reinforcement to chlorides, which can lead to severe corrosion and further spalling of concrete. Because of the localized nature of this damage, which may extend only a few feet from the bearing location, the primary concern is shear failure. In practice, mortar repairs are often used to replace this damaged cover concrete caused by exposure to deicing salts and freeze/thaw cycling (Figure 1.1). While aesthetically restorative, a mortar repair alone may not be sufficient in restoring the original shear capacity and stiffness at the end of the girder. Thus, supplemental external reinforcement may be required in order to continue to use these girders in the field and avoid costly replacement.

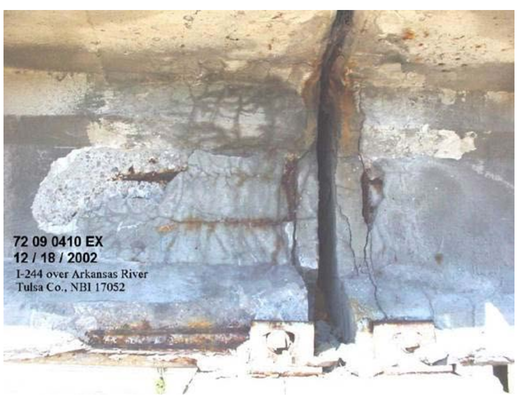

(a) End damage of girder (Ramseyer and Kang 2012)

(b) Typical mortar repair of girder end

Figure 1.1. End region damage and mortar repair of concrete bridge girder.

1.2 REPORT OUTLINE

This report presents the experimental and analytical research findings of an IDOT sponsored study performed at the University of Illinois at Urbana-Champaign (UIUC). The goals were to study the application of FRP to repair deteriorated end regions of PC bridge girders. The following is the outline of the report:

Chapter 1 provides the motivation and background for this study.

Chapter 2 presents an overview of literature relevant to the research interests of this study. This includes more information on FRP systems used in civil infrastructure. Specifically, we analyze previous uses of FRP materials as shear reinforcement for concrete beams. We also examine previous research on the effects of environmental exposure on the bond between concrete and FRP.

Chapter 3 presents experimental test results of shear pull-out tests for two types of FRP systems investigated in this project. An accelerated aging scheme is introduced to determine the effects of deicing salt exposure and freeze/thaw cycling on the bond-slip behavior of the concrete/FRP interface.

Chapter 4 presents experimental test results of three-point bending tests performed on small-scale PC T-beams. This includes information on the design and fabrication of the beams. This series of tests investigates the effects on the shear behavior due to concrete cover damage at the beam end regions followed by a mortar repair and the application of several types of FRP repairs.

Chapter 5 presents experimental test results of three-point bending tests conducted on full-scale PC I-Girders. This contains the girder specimen description and test preparation performed on girder specimens. This data is used to investigate the effectiveness of mortar and FRP repair in full-scale prestressed girders.

Chapter 6 outlines the development of a finite element model of a full-scale PC I-Girder using Abaqus (Dassault Systèmes 2013). This model is used to perform parametric studies using CFRP laminates to determine the most effective scheme for repairing the damaged end region of a PC concrete girder in shear.

Chapter 7 proposes a design methodology of FRP repair system based on the experimental test results. Two examples are presented using the proposed design approach.

Chapter 8 summarizes the important findings of the project and provides recommendations for practical application.

Three appendices are included at the end of the report. Appendix A contains figures of the post-failure surfaces of all GFRP and CFRP NSM bar specimens. Appendix B contains figures of the cross-sectional dimensions of the small-scale beam and details of the corresponding steel reinforcement. Appendix C contains figures of the cross-sectional dimensions of the full-scale girder and details of the corresponding steel reinforcement.

CHAPTER 2: LITERATURE REVIEW

2.1 FRP COMPOSITES FOR CONCRETE INFRASTRUCTURE REPAIR

There are two advantages of FRP composite materials over conventional steel reinforcement. The first is its high strength to weight ratio and the second is its resistance to corrosion. These two qualities make FRP composites ideal materials for repair and rehabilitation of civil infrastructure, specifically concrete infrastructure. The two primary FRP systems used for these types of applications are externally bonded laminates and NSM bars or plates. Externally bonded systems are comprised of a fiber sheet or mat (typically glass or carbon), which is filled with a resin to create the composite material. One method of applying the laminates to the concrete surface is through a wet layup approach (Alkhrdaji 2015), in which the resin serves to both saturate the fibers and bind the sheet to the concrete surface at the same time (Figure 2.1(a-b)). The flexibility of the fiber sheets makes the wet layup approach an effective option for adding external FRP shear reinforcement to a beam. This requires the wrapping of FRP around the beam's contour, typically done with a U-wrap around the bottom of the beam. Another approach is to glue pre-cured laminates to the concrete surface using an epoxy resin (Figure 2.1(c-d)). One disadvantage to this method is that it can only be used in situations with flat geometries, since the rigidity of a pre-cured laminate prevents it from bending around corners.

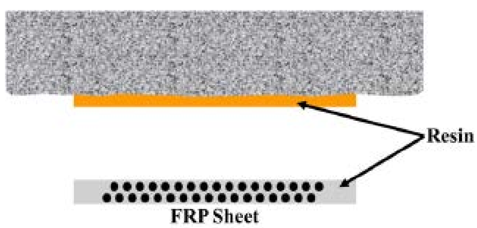

(a) Wet layup application

(b) Wet layup of CFRP on column

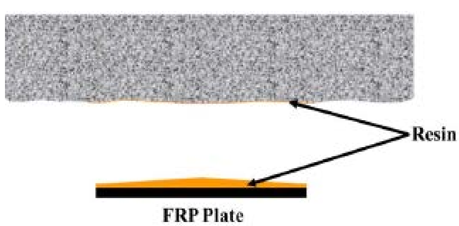

(c) Pre-cured FRP plate application

(d) CFRP plate flexural reinforcement of slab

Figure 2.1. Externally bonded FRP laminates (Mojarrad 2015).

NSM FRP systems use thin pre-cured strips or pultruded bars. However, the installation process differs from that of externally bonded plates. First, a groove is cut into the concrete surface, and the concrete in between the cuts is chiseled away. The groove is cleaned and all dust is removed with compressed air. Tape is applied to the sides of the groove for a clean final appearance. Then, the bar or thin strip is fastened into the groove with a filler material, such as an epoxy resin or cement grout. After leveling the adhesive with a trowel, the tape is removed (prior to curing of adhesive). One advantage of NSM systems compared to externally bonded laminates is that they protect the FRP reinforcement from direct environmental exposure.

Externally bonded FRP laminate and NSM FRP systems for concrete bridge girders were originally developed for flexural applications. Recently, externally bonded laminates have also emerged as an effective means of strengthening beams in shear. Guidelines and codes for designing these types of systems have been produced by many organizations (AASHTO 2017; ACI 2008; Belarbi et al. 2011; CSA 2012; Darby et al. 2012; FIB 2001; Zureick et al. 2010). Research has been performed on NSM bars and strip systems for shear applications (De Lorenzis and Teng 2006; Nanni et al. 2003; Nanni 2004; Dias and Barros 2009; Dias and Barros 2012; Islam 2008; Rizzo and DeLorenzis 2007; Al-Mahmoud et al. 2015). However, at this point, these results have been less codified than externally bonded laminates in shear. Pellegrino and Sena-Cruz (2015) detail two design approaches for NSM strips in shear that have emerged thus far. Dias and Barros (2013) provide a simple design approach based on an extensive experimental program, while Bianco et al. (2010, 2014) provide a more complicated design approach based on equilibrium, kinematic compatibility, and the constitutive behaviors of the bonded materials. Overall, both externally bonded FRP laminate and NSM FRP bars/strips have been shown to be effective for general flexural and shear applications for both reinforced and prestressed concrete girders.

2.2 FAILURE MODES AND BOND BEHAVIOR OF FRP/CONCRETE INTERFACE

Current design guidelines for FRP repairs for flexure and shear are largely based on studies of the bond between FRP and concrete. Understanding this bond behavior and the associated failure modes is crucial in determining the effective strains which can be achieved in the FRP. This also impacts the stresses which can be developed within the FRP at the design load of the member.

2.2.1 Failure Modes of FRP Reinforcement

The addition of external FRP reinforcement introduces several new failure modes for a structural member, depending on the application. Externally bonded FRP flexural reinforcement introduces three new possible failure modes: FRP rupture, delamination of the concrete cover, and debonding of FRP from the concrete substrate (ACI 2008). Cover delamination initiates at the termination point of the FRP, while FRP debonding is prompted by flexural and/or shear cracks. These two failure modes are frequently lumped together and referred to as FRP debonding. At a local level, failure can occur one of four ways: (1) the cement matrix, (2) the adhesive, (4) the FRP/adhesive interface, or (4) the adhesive/concrete interface.

Similar failure modes exist when externally bonded FRP reinforcement is used for shear. There are three FRP wrapping schemes commonly used: complete wrapping, 3-sided U-wraps, and 2-sided face plies (Figure 2.2). The complete wrapping scheme is the most efficient, and is capable of achieving a FRP rupture failure mode, even though debonding most likely occurs first (Chen and Teng 2003). However, due to loss of aggregate interlock prior to FRP rupture, ACI 440.2R-08 limits the design strain of completely wrapped members to 0.004. Most U-wrap and nearly all 2-sided schemes result in a FRP debonding failure mode with very little ductility (Chen and Tang 2003).

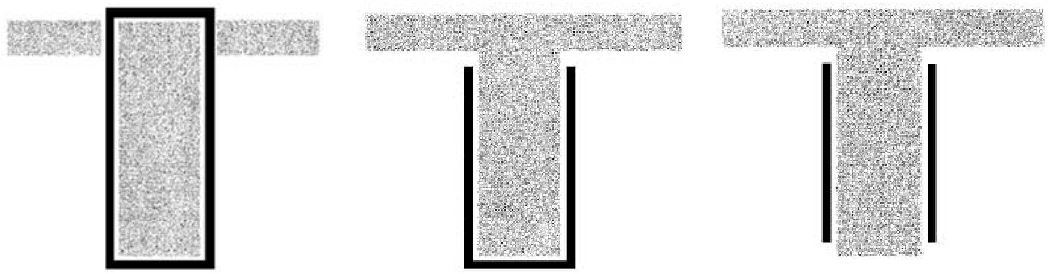

(a) Complete wrap (b) 3-sided U-wrap (c) 2-sided face plies

Figure 2.2. Wrapping schemes for FRP shear laminates (ACI 2008).

For NSM FRP bars and strips, the additional structural failure modes introduced are largely the same as externally bonded FRP, FRP rupture, and FRP debonding. Similarly, local level debonding issues can occur due to the cement matrix, the adhesive, the FRP/adhesive interface, or the adhesive/concrete interface. A mixed failure mode is possible, although one structural or one local failure mode will be dominant (Coelho et al. 2015).

2.2.2 Bond Behavior of FRP/Concrete Interface

Local bond vs. slip behavior at the FRP/concrete interface ultimately controls the debonding capacity of any externally bonded FRP laminate application. Much experimental and analytical research has been performed on the bond-slip behavior of FRP laminates/plates (Chen and Teng 2001; Yao et al. 2004; Lu et al. 2005) and NSM bars/strips (De Lorenzis 2004; De Lorenzis et al. 2002; De Lorenzis and Nanni 2002; De Lorenzis et al. 2004; Novidis and Pantazopoulou 2008; Lee et al. 2013). A key difference between these systems can be observed by looking at the bond-slip models developed in the literature. Lu et al. (2005) proposed three local bond-slip models for FRP sheets or plates bonded to concrete. These models consist of an ascending branch to the maximum bond stress τ_{max} at a corresponding slip s_0 and a descending branch that ends at $\tau = 0$ and an ultimate slip s_f. The interfacial fracture energy (area under the bond-slip curve) can be used to compare the bond strengths of different FRP-concrete interfaces. All three models are compared to finite element results and an extensive database of test results. These models accurately predict the strain distribution in FRP sheets as well as the bond strength of the FRP-concrete joint. Because of its ease of implementation without significant loss in accuracy, the bilinear bond-slip model has been used by many researchers in FE models of reinforced and prestressed concrete structures repaired with FRP laminates. As a consequence of the local bond-slip descending branch terminating at $\tau = 0$, the stress that any given FRP laminate configuration can develop prior to debonding is limited. Generally, these configurations fall below the ultimate rupture stress of the FRP material itself. This leads to the concept of effective bond length; the active bonded zone at which the majority of the interfacial shear stresses are transmitted from the FRP to the concrete. Beyond the effective bond length, no further increase in failure load can be achieved (Ouezdou et al. 2008). As cracking in the concrete occurs at the loaded end of the laminate, the effective bond length shifts to another active bonding zone. This process continues until the FRP laminate is completely debonded. This phenomenon explains the low ratios of stress in FRP at failure to ultimate tensile strength observed in experimental tests. On average, FRP laminates only achieve 28% of their ultimate tensile strength at failure (Chen and Teng 2001).

Bond-slip behavior for NSM FRP bars in concrete is similar to that of FRP laminates. De Lorenzis (2004) proposes three bond-slip models with varying shapes affected by exponential parameters. The shape of the descending branch of the bond-slip curve is dependent on factors such as failure mode (epoxy-concrete interface, epoxy splitting, or bar pull-out) and bar surface texture (ribbed, spirally wound, or sandblasted). One key difference between the bond-slip models of FRP laminates and that of the NSM FRP bars is the presence of a residual nonzero bond stress that exists after the descending branch of the curve. This is due to either a frictional bond stress τ_f for specimens with an epoxy-concrete interface failure mode or aggregate interlock at the location of longitudinal concrete cracks for specimens with an epoxy splitting failure mode. The presence of this nonzero descending branch allows for the FRP bar to develop to its ultimate tensile strength given a long enough bond length, similar to steel rebar. This gives the NSM FRP system an inherent advantage over externally bonded FRP for applications in which a long development length can be achieved.

2.3 REVIEW OF PERTINENT STUDIES

The use of externally bonded and NSM FRP for the flexural and shear strengthening of concrete girders has been proven effective for most general purpose applications. The particular application being investigated in this study, however, presents additional challenges and introduces factors that may not be addressed in current design guidelines. Due to the localization of damage at the girder ends, a concentration of FRP material near the girder end is needed. Since the FRP material may only extend just past the bearing area, the behavior of FRP laminate repairs when tested with a low shear span-to-depth ratio should be investigated. This would ensure shear cracks develop within the damaged zone. As a result, the behavior will be governed by arch action rather than beam action. Previous research has concluded that the effectiveness of externally bonded FRP shear reinforcement decreases as shear span-to-depth ratio decreases (Ary and Kang 2012; Bousselham and Chaallal 2006; Belarbi et al. 2011). This could further limit the usefulness of FRP shear laminates in this particular application. In their design guidelines for FRP shear reinforcement systems, Belarbi et al. (2011) state that the design provisions are only applicable to beams with a shear span-to-depth ratio greater than 2.5. That is because reduction factors were developed from tests with sufficient shear span-to-depth ratios to assume plane sections remain plane after deformation. Additionally, the effectiveness of an FRP repair when combined with a conventional mortar repair should be investigated to determine the material's suitability for this particular application. The interactions between the base concrete, mortar, and FRP may generate a complex strain field within the girder web, differing from that seen in cases where the FRP is added to an undamaged girder.

Research for this specific application has been very limited thus far. Ramseyer and Kang (2012) performed shear tests on AASHTO Type II girders that had been damaged and repaired with CFRP and GFRP laminates. In these tests, the girders were tested in shear using a shear span-to-depth ratio of

1. Damage was imposed by first loading the girder to its maximum load in shear, which simulated a corrosively failed end region. Post-damage repair consisted of application of rapid set cement, epoxy-injecting cracks (for some tests), and application of externally bonded wet layup CFRP and GFRP 90° U-wraps. Grooves were cut at the top of the web and metal bars were inserted to anchor the fiber sheets. Figure 2.3 illustrates this repair process. This study concluded that CFRP has the greatest amount of stiffness recovery while GFRP has the highest percentage of strength recovery. Only one test, however, was able to recover the original shear strength of the girder (GFRP with epoxy injected cracks).

(a) Damaged girder

(b) Rapid set cement repair

(c) Epoxy injection tubes

(d) Primer and putty

(e) Grooves cut in top of beam web

(f) CFRP U-wrap application

Figure 2.3. Post-Damage repair of PC girders (Ramseyer and Kang 2012).

Furthermore, while FRP composite materials are generally considered environmentally resistant, the bond between the FRP and concrete may be adversely affected by the exposure to high levels of water, deicing salts, and freeze/thaw cycling applied to the end regions of these concrete bridge girders. ACI 440.2R-08 (ACI 2008) gives environmental reduction factors for various FRP systems and exposure conditions which limit their design rupture strains. However, for shear design, even the most stringent of these reduction factors (0.5 for GFRP systems in an aggressive environment) might not actually reduce the effective strain in shear applications, which is capped at 0.004. This is due to loss of aggregate interlock of the concrete. Thus, it is important to investigate further the effects of environmental exposure on the bond behavior of externally bonded and NSM FRP systems in order to determine if these systems will retain effectiveness over time at the end regions of concrete girders.

Much research on the environmental aging effects of the FRP-concrete interface has been performed, but conclusions vary significantly. Colombi et al. (2009) conducted pull-out debonding tests on CFRP plates and wraps subjected to 100 and 200 freeze-thaw cycles. They concluded that the conditioning did not significantly affect the ultimate load. Silva et al. (2014) subjected reinforced concrete beams with CFRP and GFRP laminate systems to salt fog and wet-dry cycles for 10,000 hours. Salt fog cycles were more detrimental than moisture cycles for either CFRP or GFRP. Davalos et al. (2008) investigated the fracture energy behavior of GFRP-concrete interfaces subjected to freeze-thaw cycling in the presence of a 4% $CaCl_2$ solution. This aging protocol resulted in fracture energy decreases of 38.5%, 50.5%, and 59% for normal strength concrete specimens at 100, 200, and 300 cycles, respectively. Subramaniam et al. (2008) conducted direct shear tests on CFRP sheets bonded to concrete and saw a 17% reduction in ultimate load and a 35% reduction in fracture energy after 300 freeze-thaw cycles. Al-Mahmoud et al. (2014) performed hinged beam tests with CFRP sheets and plates subjected to either 300 freeze-thaw cycles or 120 days of salt water immersion. The freeze-thaw cycles caused a 25% decrease in ultimate force for both the sheets and plates, while the salt water caused a deterioration of 48% for the sheets but negligible change in the plate specimens. Salt water immersion also changed the failure mode of the interface from debonding in a thin concrete layer to failure at the concrete/resin interface. Garzón-Roca et al. (2015) performed pull-out tests on NSM CFRP strips with different bond lengths, groove widths, groove depths, and an aging scheme with 90 wet-dry cycles. The wet-dry cycling caused a decrease of 12% in the maximum pull-out force for specimens with 15 mm (0.59 in.) groove depth, 4 mm (0.16 in.) groove width, and 60 mm (2.4 in.) bond length. However, the effect was significantly reduced or became negligible with increased bond length or groove width, respectively. Soliman et al. (2011) performed pull-out tests on NSM CFRP and GFRP bars subjected to 200 freeze-thaw cycles. Prior to freeze-thaw cycling, service cracks with a maximum width of 0.3 mm (0.012 in.) were developed in the specimens by tensioning up to 30% of the failure load. The conditioning caused hair cracks to form in the epoxy adhesive, which resulted in pull-out force reductions of 8-14% compared to the reference specimens. The wide range of testing setups, materials used, aging protocols, and failure modes observed in the literature make it difficult to definitively characterize the effects of long-term aging on the FRP-concrete interface. Tests which consider the combination of freezing/thawing and salt water exposure on the FRP/concrete interface are lacking, specifically with regards to CFRP laminates and both GFRP and CFRP NSM bar systems. Thus, the accelerated aging tests carried out in this study were focused on filling these knowledge gaps.

CHAPTER 3: ACCELERATED AGING AND PULL-OUT TESTS

In this chapter, the experimental results of shear bond-slip tests involving both FRP externally bonded laminate and NSM bar specimens are presented. An accelerated aging scheme was developed and applied to a set of these specimens in order to determine the effects of long-term exposure to water containing deicing salts and freeze/thaw cycling. The results are analyzed to determine the most effective and efficient FRP material type and system from the perspective of long-term durability of the FRP/concrete interface in harsh environmental conditions.

3.1 FRP MATERIAL DESCRIPTION

In this study, GFRP laminate, CFRP laminate, and NSM bar systems were tested. The dimensions of the FRP systems used in the tests and the material properties are summarized in Table 3.1. For the FRP laminates and bars, both the manufacturers' properties and those acquired from laboratory tests are presented. The laboratory tests were conducted using ASTM D3039/D3039M-14 (2014) and ASTMD7565/D7565M-10 (2010) for the FRP laminates and ASTM D7205/D7205M-06 (2011) for FRP bars. The GFRP laminates have a lower elastic modulus and tensile strength, so any given field repair would likely require more GFRP material than CFRP. Since the main purpose of this study is to determine how accelerated aging will affect different FRP repair systems for the same application, two plies of GFRP were used compared to one ply of CFRP for the laminate tests. The GFRP and CFRP bars used were the Aslan 100 series (Hughes Brothers 2011a) and Aslan 200 series (Hughes Brothers 2011b) manufactured by Hughes Brothers, Inc. The bars were sandblasted in order to provide increased bond with the epoxy filler. The GFRP bars had a spiral winding as well, and the sand coating was slightly coarser than that of the CFRP bars. Hilti HIT-RE 500 epoxy adhesive (Hilti 2014) was used as the groove filler material for the NSM bar specimens, per recommendation by Hughes Brothers. The average 28-day compressive strength of the concrete specimens was 44.8 MPa (6,500 psi).

Table 3.1. Material Properties of FRP Systems

Material	Size[a], mm (in.)	Area, mm² (in.²)	Source	Elastic Modulus, GPa (ksi)	Tensile Strength, MPa (ksi)	Tensile Strain, mm/mm (in./in.)
GFRP laminate	2.54 x 76.2 (0.1 x 3)	193.55 (0.3)	Manufacturer	27.4 (3,980)	587 (85.2)	0.023
			Laboratory	22.2 (3,200)	399 (58)	0.018
CFRP laminate	1.24 x 76.2 (0.049 x 3)	94.49 (0.15)	Manufacturer	86.9 (13,000)	930 (135)	0.0098
			Laboratory	91.7 (13,000)	1,020 (148)	0.011
GFRP bar	6.35 (0.25)	31.67 (0.049)	Manufacturer	46 (6,700)	896 (130)	0.0194
			Laboratory	50.3 (7,300)	1,062 (154)	0.0255
CFRP bar	6.35 (0.25)	31.67 (0.049)	Manufacturer	124 (18,000)	2,241 (325)	0.0181
			Laboratory	137.9 (20,000)	2,461 (357)	0.0213
Epoxy filler	--	--	Manufacturer	1.493 (220)	43.5 (6.31)	0.020

[a]Thickness by width for laminates, diameter for bars

3.2 SPECIMEN DESCRIPTION AND TEST SETUP

Experimental tests on the bond-slip behavior of FRP laminates and NSM bars are generally performed using either a direct pull-out configuration (De Lorenzis et al. 2002; Lee et al. 2013; Novidis and Pantazopoulou 2008; Yao et al. 2004; Soliman et al. 2011; Columbi et al. 2009; Garzón-Roca et al. 2015; Subramaniam et al. 2008) or a hinged/split beam approach (Al-Mahmoud et al. 2014; Silva et al. 2014). The direct pull-out configuration was chosen in this study due to its simplicity and ease at which the accelerated aging scheme could be implemented. A total of 36 concrete blocks with dimensions of 305 x 89 x 89 mm (12 x 3.5 x 3.5 in.) were cast. The concrete specimen dimensions and test setup were designed to accommodate the testing of both FRP laminate and NSM bar specimens (Figure 3.1). The top and bottom fixture plates included openings for both the laminates and NSM bars. The FRP laminate specimens were tested on a machine with an 89 kN (20 kip) load cell, and a set of 120 mm (4.7 in.) wide serrated grips were used to grip the FRP laminate. FRP tabs were glued to the gripping end of the laminates prior to testing in order to prevent FRP rupture at the grip location. The FRP NSM bar specimens were tested on a machine with a 222 kN (50 kip) load cell with hydraulically pressurized grips. To prevent crushing of the FRP bars by the hydraulic grips, a steel pipe filled with high strength non-shrink grout was used as an anchor at the loading end of the bar. For both FRP systems, slip at the free end of the laminate/bar was measured using an extensometer.

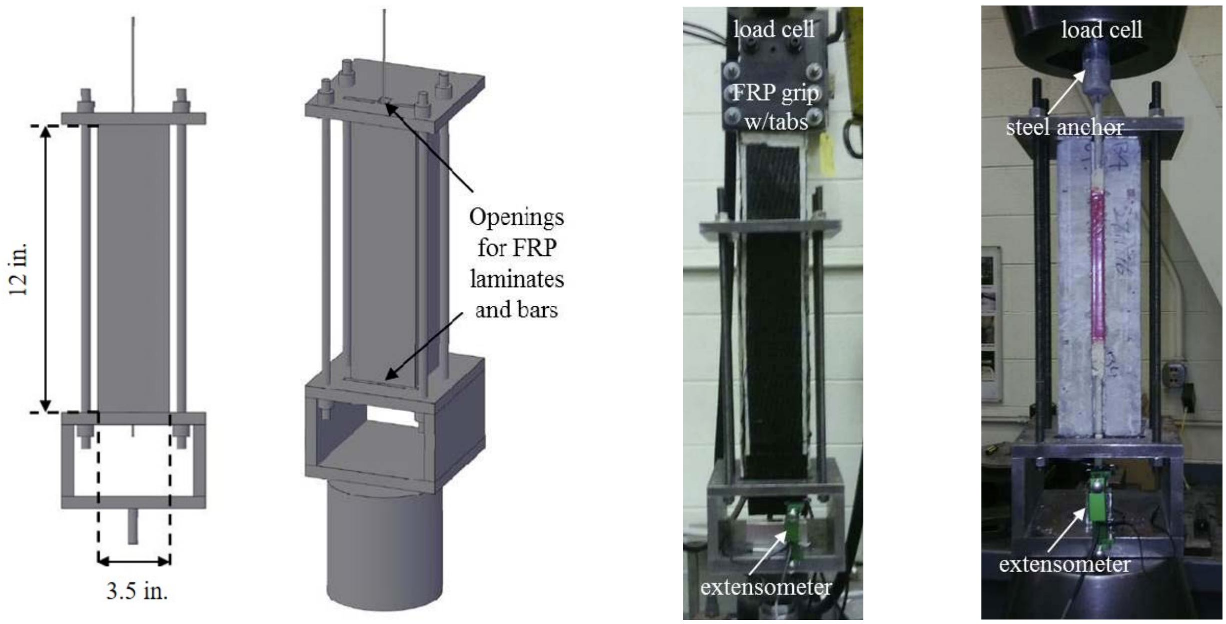

(a) Specimen dimensions (b) Test fixture (c) Laminate specimen (d) NSM bar specimen

Figure 3.1. Shear pull-out test setup.

In addition to FRP system and material type, two other variables were investigated: bond length and accelerated aging duration. In order to reduce the influence of the concrete compressive stresses on the FRP/concrete interface under the loading plate, all bond lengths were started 51 mm (2 in.) from the top edge of the concrete specimens. For the laminates, bond length was prescribed by marking the bonded area on one face of the concrete block and applying clear tape outside of the marked area. The surface of the bonded area was textured with a hard steel wire brush before applying the FRP laminate. For the NSM bar specimens, a 9.5 x 9.5 mm (0.38 x 0.38 in.) groove was cut down the center of a face of the concrete block. This groove size meets the minimum groove dimensions ($1.5d_b$) and minimum clear edge distance ($4d_g$) as prescribed by ACI 440.2R-08 (ACI 2008), where d_b is the diameter of the FRP bar and dg is the groove depth. Bond length was prescribed by placing clay at the termination points of the epoxy filler. The complete test matrix is presented in Table 3.2.

Table 3.2. Test Matrix

Specimen	Material/System	Bond Length, mm (in.)	Aging (# cycles)
G-4-A0	GFRP laminate	101.6 (4)	0
G-6-A0		152.4 (6)	0
G-8-A0		203.2 (8)	0
G-4-A40		101.6 (4)	40
G-6-A40		152.4 (6)	40
G-8-A40		203.2 (8)	40
G-4-A100		101.6 (4)	100
G-6-A100		152.4 (6)	100
G-8-A100		203.2 (8)	100
C-4-A0	CFRP laminate	101.6 (4)	0
C-6-A0		152.4 (6)	0
C-8-A0		203.2 (8)	0
C-4-A40		101.6 (4)	40
C-6-A40		152.4 (6)	40
C-8-A40		203.2 (8)	40
C-4-A100		101.6 (4)	100
C-6-A100		152.4 (6)	100
C-8-A100		203.2 (8)	100
G-b-4-A0	GFRP bar	101.6 (4)	0
G-b-6-A0		152.4 (6)	0
G-b-8-A0		203.2 (8)	0
G-b-4-A40		101.6 (4)	40
G-b-6-A40		152.4 (6)	40
G-b-8-A40		203.2 (8)	40
G-b-4-A100		101.6 (4)	100
G-b-6-A100		152.4 (6)	100
G-b-8-A100		203.2 (8)	100
C-b-4-A0	CFRP bar	101.6 (4)	0
C-b-6-A0		152.4 (6)	0
C-b-8-A0		203.2 (8)	0
C-b-4-A40		101.6 (4)	40
C-b-6-A40		152.4 (6)	40
C-b-8-A40		203.2 (8)	40
C-b-4-A100		101.6 (4)	100
C-b-6-A100		152.4 (6)	100
C-b-8-A100		203.2 (8)	100

3.3 ACCELERATED AGING PROTOCOL

The aggressive aging scheme used in these tests was designed to represent the harsh conditions that cause deterioration at the end regions of concrete bridge girders. During the winter season, deicing salts leak onto the ends of the girders and multiple freezing/thawing cycles occur. To incorporate the effect of aging in the pull-out tests carried out in this study, an aging protocol similar to that of Davalos et al. (2008) was applied. This protocol combined aspects of ASTM C666/C666M-15 (2015) and ASTM C672/C672M-12 (2012). Specimens were placed laminate/bar side down in trays containing 6 mm (0.25in.) of solution of deicing salt and water. ASTM C672/C672M-12 (2012) specifies the use of $CaCl_2$ with a concentration of 4 g/100 ml (0.33 lb/gal) of solution, but states that other chemical deicers may be used. Since rock salt is commonly used as a deicing chemical, NaCl was used as a substitute, with an equivalent concentration of Cl^- (4.21 g/100 ml (0.35lb/gal) of NaCl). One freeze/thaw cycle was performed per day ranging from -18 to 4 °C (0 to 40 °F). The cycle consisted of 16 hours to lower the temperature from 4 to -18 °C (40 to 0 °F), 6 hours at -18 °C (0 °F), and 2 hours to raise the temperature from -18 to 4 °C (0 to 40 °F) (Figure 3.2). Freeze/thaw cycling was performed in a conventional chest freezer (Figure 3.3), with the use of an electric resistance heater to thaw the specimens. The trays were rotated throughout the cycling process in order to account for any uneven distribution of heat within the freezer. After 40 cycles, the concrete specimens showed moderate scaling, and half of the aged specimens were tested along with the unaged specimens. The rest of the specimens were continued on to 100 cycles, at which point they were tested.

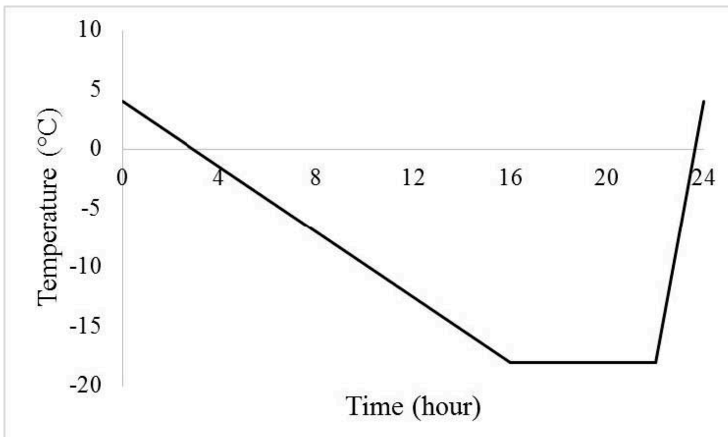

Figure 3.2. Freeze-thaw cycle protocol.

Figure 3.3. Specimens in freezer during freeze cycle.

3.4 TEST RESULTS

3.4.1 Effect of aging on specimen condition

Compared to the 40 cycle specimens, the 100 cycle specimens showed increased scaling of the concrete (moderate to severe), and in many cases coarse aggregate had been exposed and/or completely spalled off. Figure 3.4(a) compares a set of concrete specimens with no aging, 40 freeze/thaw cycles, and 100 freeze/thaw cycles. The most severe of concrete damages occurred mainly at the ends of the specimens (Figure 3.4(b)), which generally left the bonded portions of FRP intact. One laminate specimen (G-6-A100) had scaling on one side that resulted in loss of a minor portion of bonded area, as shown in Figure 3.4(c). There were also two 100 cycle CFRP laminate specimens that had severely damaged ends that rendered the specimens untestable due to lack of bearing area against the plates in the test fixture, one of which is shown in Figure 3.4(d). For this reason, the results for these 100 cycle CFRP laminates are omitted. Other than some salt depositions on the laminates, the FRP laminates, bars, and epoxy filler had no visible signs of deterioration.

(a) G-b-4 specimens: A0, A40, A100

(b) Scaling/spalling at specimen ends

(c) Scaling induced loss of bonded area

(d) Severe end damage on C-6-A100

Figure 3.4. Effect of accelerated aging on concrete specimens.

3.4.2 FRP Laminates

Table 3.3 summarizes the test results for the FRP laminates. Figure 3.5 presents the pull-out force data for the FRP laminates in a manner in which comparisons can easily be made between different bond lengths and aging durations. The maximum stress in the laminate σ_{max} was calculated by dividing the pull-out force by the laminate cross-sectional area. The maximum strain in the laminate was computed by dividing σ_{max} by the modulus of the material. Average bond stress is the pull-out force divided by the bonded area of the laminate. The failure mode for all specimens was sudden delamination at the FRP/concrete interface with complete debonding of the FRP laminate. Typically, this type of failure mode occurs a few millimeters below the interface for normal strength concrete. In these tests, however, the delamination occurred through a layer of concrete less than 1 mm (0.039 in.). This indicates that surface preparation was likely insufficient, as the concrete failed in its weakest, outermost layer.

Table 3.3. Test Results for FRP Laminates

Specimen	Pull-out Force, kN (kips)	σ_{max}, MPa (ksi)	ε_{max}, (%)	Average Bond Stress, MPa (psi)	Difference[b], (%)
G-4-A0	16.92 (3.80)	87.4 (12.7)	0.32	2.19 (318)	--
G-6-A0	18.37 (4.13)	94.9 (13.8)	0.35	1.58 (229)	--
G-8-A0	20.51 (4.61)	106.0 (15.4)	0.39	1.32 (191)	--
G-4-A40	13.50 (3.04)	69.8 (10.1)	0.25	1.74 (252)	-20.2
G-6-A40	18.09 (4.07)	93.5 (13.6)	0.34	1.56 (226)	-1.5
G-8-A40	17.60 (3.96)	90.9 (13.2)	0.33	1.14 (165)	-14.2
G-4-A100	14.17 (3.19)	73.2 (10.6)	0.27	1.83 (265)	-16.2
G-6-A100	14.42 (3.24)	74.5 (10.8)	0.27	1.24 (180)	-21.5
G-8-A100	17.93 (4.03)	92.6 (13.4)	0.34	1.16 (168)	-12.6
C-4-A0	20.83 (4.68)	219.7 (31.9)	0.25	2.69 (390)	--
C-6-A0	18.98 (4.27)	200.2 (29.0)	0.22	1.63 (236)	--
C-8-A0	20.71 (4.66)	218.4 (31.7)	0.24	1.34 (194)	--
C-4-A40	13.82 (3.11)	145.7 (21.1)	0.16	1.78 (258)	-33.7
C-6-A40	14.32 (3.22)	151 (21.9)	0.17	1.23 (178)	-24.6
C-8-A40	15.45 (3.47)	162.9 (23.6)	0.18	1.00 (145)	-25.4
C-4-A100	18.08 (4.06)	190.7 (27.7)	0.21	2.34 (339)	-13.2
C-6-A100[a]	--	--	--	--	--
C-8-A100[a]	--	--	--	--	--

[a]Specimen was untestable after aging due to severe deterioration at ends of concrete block

[b]With respect to unaged specimens

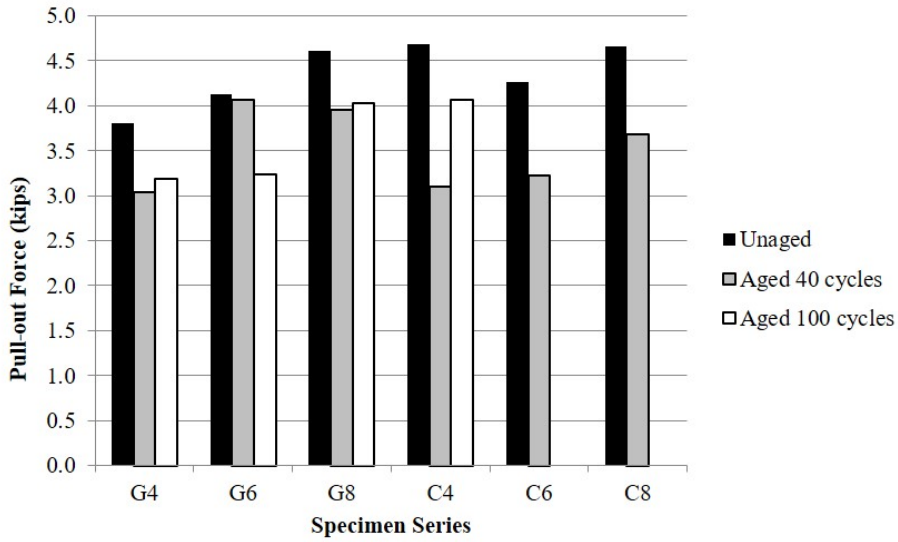

Figure 3.5. Pull-out force comparison for FRP laminates.

For the unaged specimens, the GFRP laminates saw an increase in pull-out force with increased bond length, while the CFRP laminates did not show this trend. Theoretically, the maximum pull-out force of any given FRP/concrete interface is achieved once the bonded length exceeds the effective bond length (Ouezdou et al. 2008). These results imply that effective bond length of the GFRP laminates was greater than 152 mm (6 in.), while the effective bond length of the CFRP laminates was less than or equal to 102mm (4 in.). From Figure 3.5, an increase in pull-out force with increased bond length for both GFRP and CFRP (with G-6-A40 being the only outlier) implies that the effective bond length was increased due to aging.

The effect of aging was more severe in the CFRP laminates than the GFRP. Across all bond lengths of GFRP specimens, 40 cycles and 100 cycles of aging resulted in average pull-out force decreases of 11.9% and 16.7%, respectively, from the unaged specimens. For the CFRP specimens, 40 cycles of aging resulted in an average pull-out force decrease of 26.4%. This discrepancy could be attributed to many factors, including differences in stiffness of the FRP laminates, thicknesses of the FRP, or material type. One likely cause was the difference in thickness. Deeper immersion of CFRP specimens could have more adversely affected the interface on the specimens.

Figures 3.6 and 3.7 show the pull-out force vs. end-slip curves for all of the GFRP and CFRP laminate specimens. In general, the specimens with accelerated aging had a decreased stiffness and greater end-slip at failure than their respective unaged specimens. This was the case for the 102 and 152 mm (4 and 6 in.) bond lengths of GFRP and all three bond lengths of CFRP. For the 203 mm (8 in.) bond length A0 and A100 GFRP specimens, nonlinear force vs. end-slip behavior resulted in a much higher end-slip at failure than any other case. Another observed trend was that the increased bond length generally results in a stiffer interface. The unaged series of CFRP laminates clearly exhibits this trend, in which the stiffness increases as the bond length increases from 102 to 203 mm (4 to 8 in.).

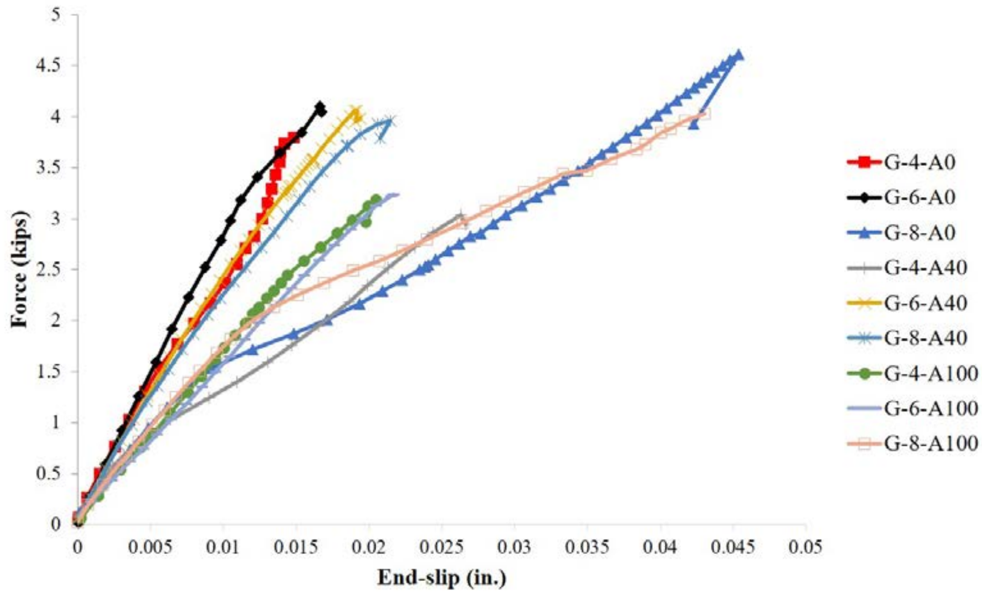

Figure 3.6. Pull-out force vs. end-slip for GFRP laminates.

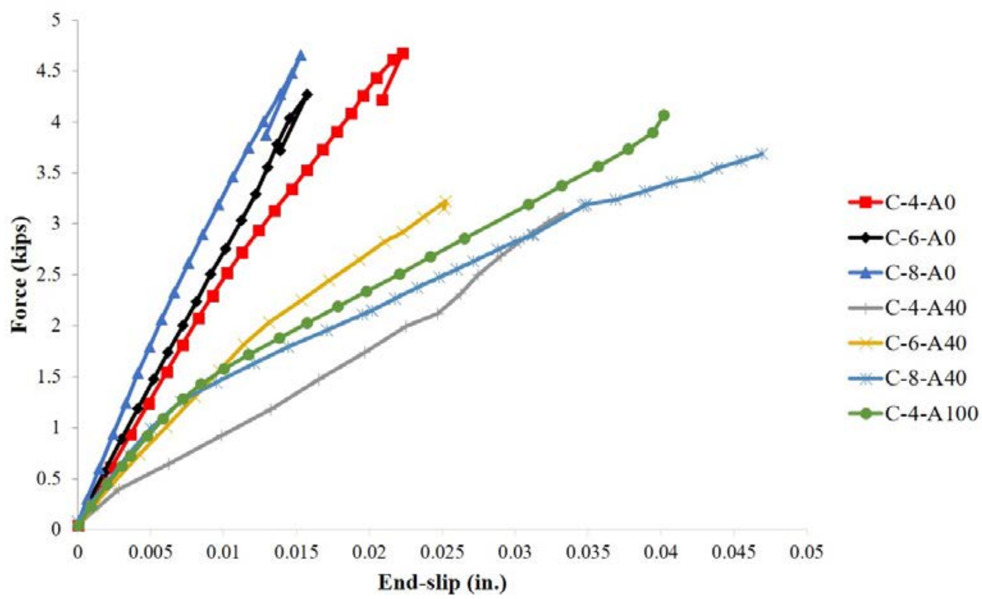

Figure 3.7. Pull-out force vs. end-slip for CFRP laminates.

3.4.3 NSM FRP Bars

Table 3.4 summarizes the test results for the FRP NSM bars, including the various failure modes. Figure 3.8 presents the pull-out force data for the FRP NSM bars to compare results between different bond lengths and aging durations. The post-failure surfaces of all GFRP and CFRP NSM bar specimens are shown in Figures A.1 and A.2 in Appendix A.

Table 3.4. Test Results for FRP NSM Bars

Specimen	Pull-out Force, kN (kips)	σ_{max}, MPa (ksi)	ε_{max}, (%)	Average Bond Stress[a], MPa (psi)	Difference[d], (%)	Failure Mode[b]
G-b-4-A0	28.61 (6.43)	905.1 (131)	1.96	14.14 (2,100)	--	EB, CS, FS
G-b-6-A0	30.15 (6.78)	953.9 (138)	2.06	9.94 (1,400)	--	FR
G-b-8-A0	30.68 (6.90)	970.6 (141)	2.10	7.58 (1,100)	--	FR
G-b-4-A40	26.88 (6.04)	850.3 (123)	1.84	13.29 (1,900)	-6.0	EB+CS+FS
G-b-6-A40	28.12 (6.32)	889.7 (129)	1.93	9.27 (1,300)	-6.7	EB+CS+FS
G-b-8-A40	32.63 (7.34)	1032.4 (150)	2.23	8.07 (1,200)	+6.4	FR
G-b-4-A100	27.99 (6.29)	885.5 (128)	1.92	13.84 (2,000)	-2.2	EB+CS+FS
G-b-6-A100	29.32 (6.59)	927.6 (135)	2.01	9.66 (1,400)	-2.8	EB+CS+FS
G-b-8-A100	31.97 (7.19)	1011.5 (147)	2.19	7.90 (1,100)	+4.2	FR+CF
C-b-4-A0	41.55 (9.34)	1314.6 (191)	1.06	0.54 (3,000)	--	EB+CS
C-b-6-A0	37.39 (8.41)	1182.8 (172)	0.95	12.32 (1,800)	--	EB+CS+CF
C-b-8-A0	49.10 (11.0)	1553.2 (225)	1.25	12.13 (1,800)	--	EB+CS+CF
C-b-4-A40	28.23 (6.35)	893.0 (130)	0.72	13.95 (2,000)	-32.1	CC+EC
C-b-6-A40	43.01 (9.67)	1360.7 (197)	1.10	14.17 (2,100)	+15.0	EB+CC
C-b-8-A40	34.76 (7.81)	1099.7 (159)	0.89	8.59 (1,200)	-29.2	ES+CC+EC
C-b-4-A100	27.07 (6.09)	856.2 (124)	0.69	13.38 (1,900)	-34.9	ES+CC+EC
C-b-6-A100	41.71 (9.38)	1319.6 (191)	1.06	13.75 (2,000)	+11.6	EB+CC+EC
C-b-8-A100[c]	26.80 (6.03)	847.9 (123)	0.68	6.62 (960)	-45.4	ES+CC+EC

[a]Bond stress is calculated at the epoxy/bar interface for all specimens, regardless of failure mode

[b]ES = epoxy splitting; EB = failure at epoxy/bar interface with epoxy breakage; CC = concrete cracking; CS = concrete spalling; CF = concrete fracture at top of specimen; EC = failure at the epoxy/concrete interface; FS = FRP bar spiral winding splitting; FR = FRP bar rupture

[c]Specimen shifted during testing, causing bar to be pulled at an angle

[d]With respect to unaged specimens

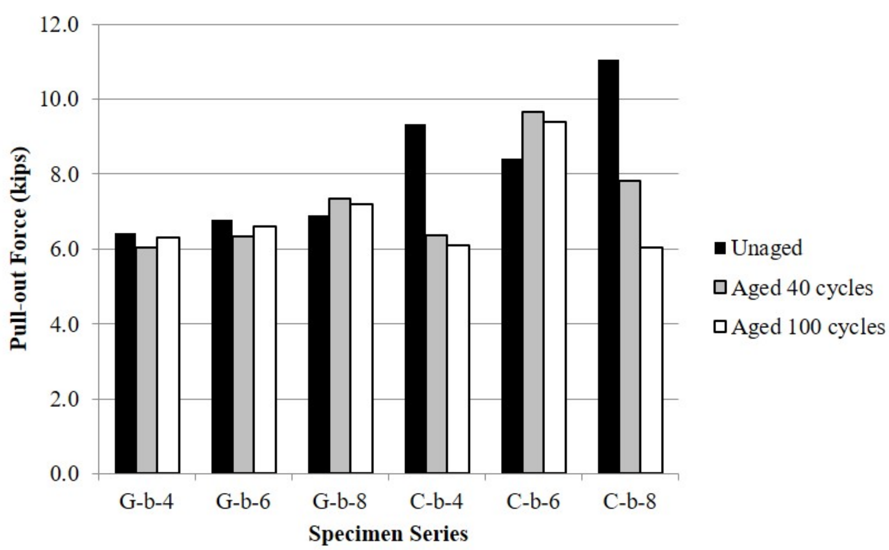

Figure 3.8. Pull-out force comparison for FRP NSM bars.

As was observed with the FRP laminates, an increase in bond length generally corresponded to an increase in pull-out force. This was the case for unaged, 40 cycle, and 100 cycle GFRP bar series. The CFRP bars, however, did not explicitly follow this trend.

Figures 3.9 and 3.10 show the pull-out force vs. end-slip curves for all of the GFRP and CFRP NSM bar specimens. As with the laminates, the specimens with accelerated aging had a decreased stiffness compared to their respective unaged specimens. This was true for all bond lengths of GFRP and CFRP. For the GFRP bars with 152 and 203 mm (6 and 8 in.) bond lengths, the end-slip at failure after 40 cycles was over twice that of the unaged specimens. Even though the failure mode was EB or FR for the aged GFRP bars, the additional end-slip may be attributed to the epoxy/concrete interface, which likely suffered from the accelerated aging while the epoxy/bar interface did not. The plateaus close to the peak load seen in Figure 3.10 for C-b-6-A0 and C-b-8-A0 are likely due to the concrete fracture that occurred at the top of these specimens, which caused a slight rotation of the concrete block, resulting in an increase in the displacement measured by the extensometer that is not actually end-slip.

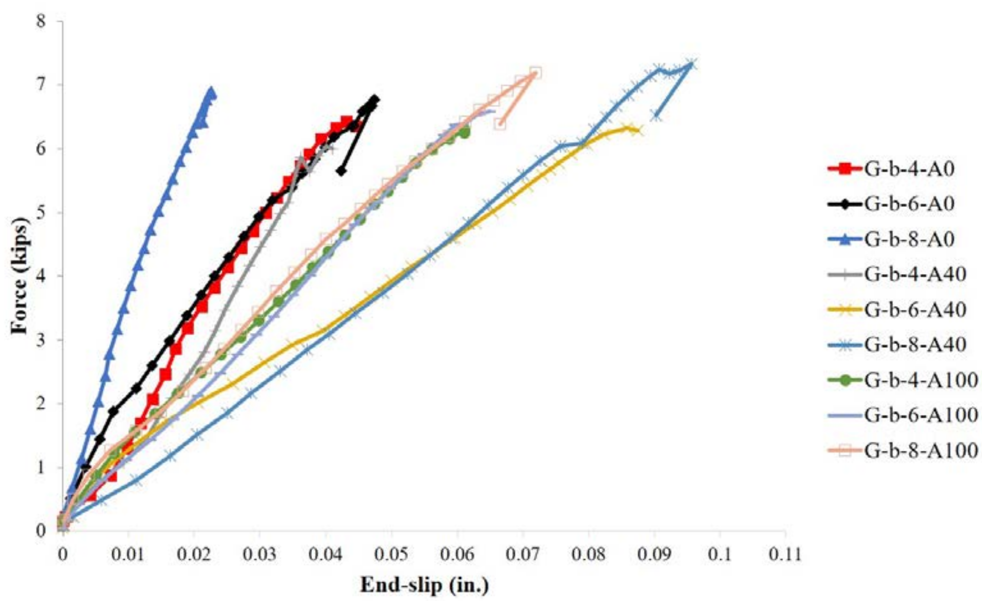

Figure 3.9. Pull-out force vs. end-slip for GFRP NSM bars.

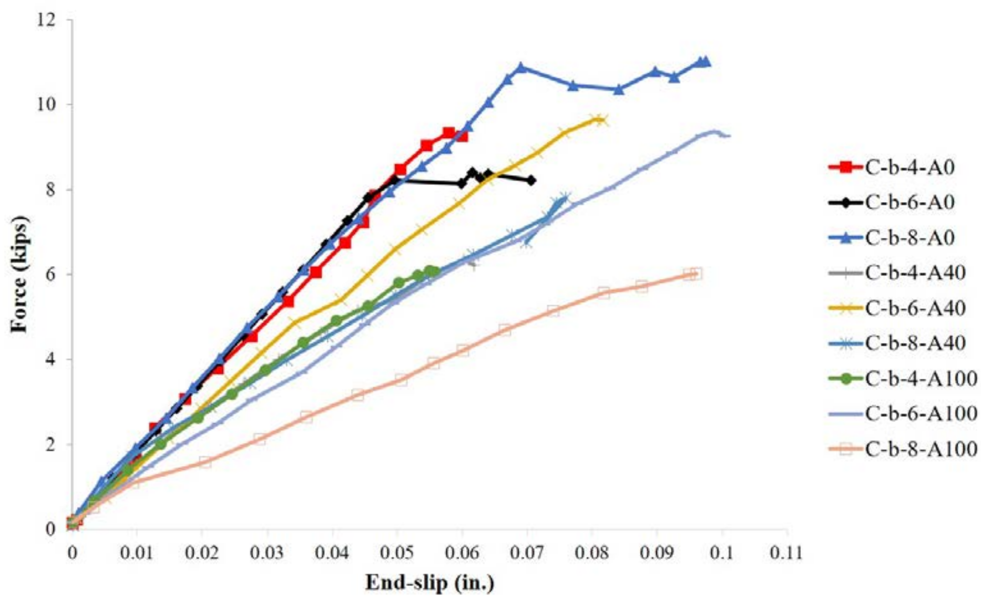

Figure 3.10. Pull-out force vs. end-slip for CFRP NSM bars.

CHAPTER 4: FLEXURAL TESTS OF SMALL-SCALE BEAMS

This chapter presents the description and results of the experimental tests that were carried out to investigate the application of FRP composite materials as a means of repairing and retrofitting damaged end regions of prestressed bridge girders. Three-point bending tests were carried out on three small-scale PC beams that had been damaged then reinforced with CFRP and GFRP externally bonded laminates and CFRP NSM bars. First, we tested the ability of a basic mortar repair to restore the shear strength of the beam. Then, FRP laminate repairs were performed in combination with the mortar repair to investigate their effectiveness for this type of application.

4.1 TEST DESCRIPTION AND TEST SETUP

4.1.1 Beam Specimen Design

Three 7 m (23 ft.) long small-scale PC beams were cast in the laboratory. The cross-sectional dimensions of the beam, which details the steel reinforcement, are shown in Figure B.1 in Appendix B. The cross-section of the beam was sized approximately as a half-scale AASHTO Type II I-girder. A top flange was added to represent a portion of slab and to give the beam a greater flexural capacity. The bottom flange retained the geometry and proportions of the AASHTO Type II girder. The beam was cast using concrete with a 28-day cylinder compressive strength of 48.1 MPa (7 ksi). The beam was prestressed with three 12.7 mm (0.5 in.) diameter 7-wire strands with an elastic modulus of 197.9 GPa (28,700 ksi) and ultimate strength of 1862 MPa (270 ksi). The strands were pretensioned to 1234 MPa (179 ksi), or 66% of the ultimate strength. Additional longitudinal mild steel was provided in the form of 6.35 mm (0.25 in.) diameter bars with a yield strength of 414 MPa (60 ksi). Shear reinforcement consisted of bent 6.35 mm (0.25 in.) diameter 414 MPa (60 ksi) bars in both the web and bottom flange spaced at 88.9 mm (3.5 in.) over the central portion of the beam.

At the ends of the beams, which were tested in three-point bending, stirrup area was reduced to ensure shear failure. The objective was to reduce the amount of shear reinforcement while keeping the stirrup spacing at or below 127 mm (5 in.). In doing so, this helped to ensure shear cracks would propagate across multiple stirrups during testing. This required using bars with less cross-sectional area than that of a 6.35 mm (0.25 in.) rebar. To obtain a cross-sectional area below that of 6.35 mm (0.25 in.) rebar and retain a textured surface with good bond characteristics, threaded rod was used for stirrups in the beam ends. 5 mm (0.2 in.) diameter threaded rod stirrups with a cross-sectional area of 14.2 mm^2 (0.022 in^2) were spaced at 127 mm (5 in.) over the first 1130 mm (44.5 in.) of the beam on one end and 2260 mm (89 in.) on the other end. The spacing was not increased any further in order to ensure shear cracks would still propagate across multiple stirrups. The Grade B7 threaded rod had a minimum tensile strength of 860 MPa (125 ksi) as supplied by the manufacturer. Thus, the threaded rod was heat treated to achieve a yield strength close to that of 414 MPa (60 ksi) mild steel. The heat treatment consisted of raising the temperature to a specified level and heating for one hour, followed by air cooling to room temperature. A range of temperatures from 566 to 816 °C (1050 to 1500 °F) were tested to determine the treatment temperature which would cause yielding closest to 414 MPa (60 ksi). At 760 °C (1400 °F), the yield strength of the threaded rod was reduced to 420 MPa (60.9 ksi). Figure 4.1 shows the stress-strain curves obtained from tensile tests of untreated and heat treated threaded rod. After determining the ideal temperature, the heat treatment was applied to all of the threaded rod used for stirrups in the beam ends. Figure 4.2 shows the casting process of the beam specimens.

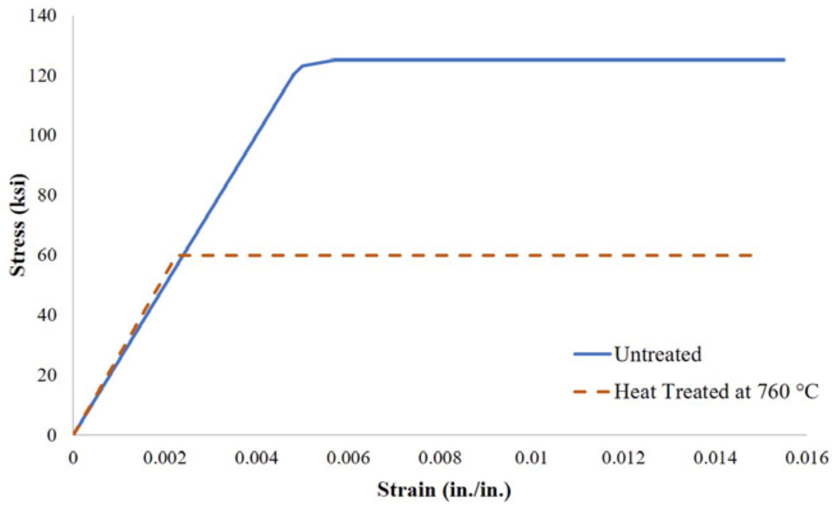

Figure 4.1. Stress-strain curves for threaded rod.

(a) Formwork construction

(b) Bent rebar (c) Concrete pouring (d) Completed pouring

Figure 4.2. Beam specimen casting.

4.1.2 Test Setup

To test the shear capacity of the beams in this study, three-point bending tests were carried out near the ends of the beams. Movable supports were utilized to adjust the length of the tested portion of the beam. A temporary support was placed under the untested cantilever portion of the beam prior to loading to prevent overturning, However, as the load was applied, only the two supports shown in Figure 4.3 transmitted the load to the floor. Due to the localized nature of the damage being considered in this study, a low shear span-to-depth ratio was used in this study to investigate the shear behavior of the beam when cracks develop through the damaged end region. The depth to the prestressing strands (d_p) of the beam is 394 mm (15.5 in.). The shear span was set to 508 mm (20 in.), or approximately 1.3dp, from center to center of the 152 mm (6 in.) wide support/loading plates. A support-to-support distance of 2,896 mm (114 in.) was used to ensure the portion of the beam outside of the shear span was undamaged during testing. In order to get more than two tests per beam, foam pieces were placed at multiple locations in the bottom flange of the beam during the casting process. The purpose of these notches was to allow for the cutting of the prestressing strands after testing the exterior shear span, after which the supports could be moved and an interior shear span could be tested. This process is illustrated in Figure 4.3. Due to the stress transfer having already taken place when cutting the strands at the notches, the exterior spans were inherently weaker due to the transfer length of the strands. Thus, the results from exterior and interior spans were compared separately. After testing one end, the beams were flipped and the other end was tested using the same configuration.

Testing was conducted in displacement control mode, and load was supplied by a 445 kN (100 kips) capacity actuator. Deflection was measured at the loading point using a linear variable displacement transformer (LVDT). An LVDT rosette was placed on the web at the center of the shear span to measure the average strains in the web at 0°, 45°, and 90°. This data was then used to calculate principal strains over this portion of the web. Strain gages were placed under the loading point at the top and bottom flanges to monitor the compressive and tensile strains, respectively. An LVDT was clamped to the central prestressing strand to monitor the end-slip of the strand during loading. For interior span tests, end-slip was not monitored due to the inaccessibility of the strands at the notch location. Figure 4.4 shows the locations of the instrumentation used in the test.

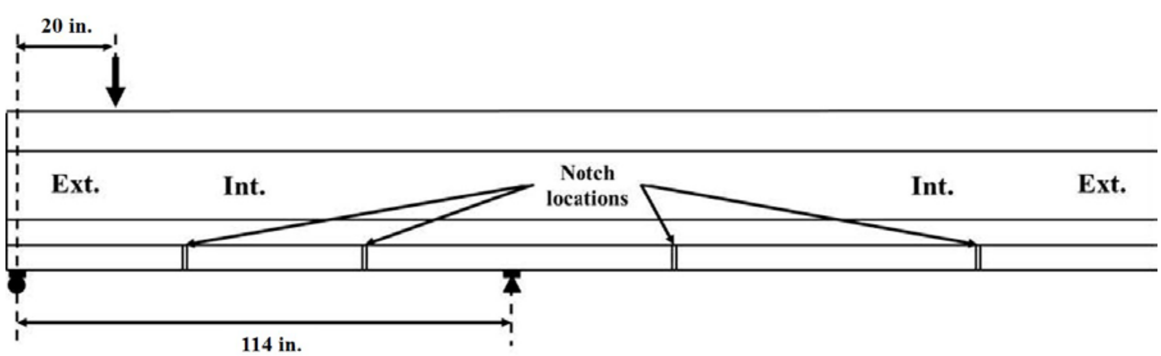

(a) Exterior span

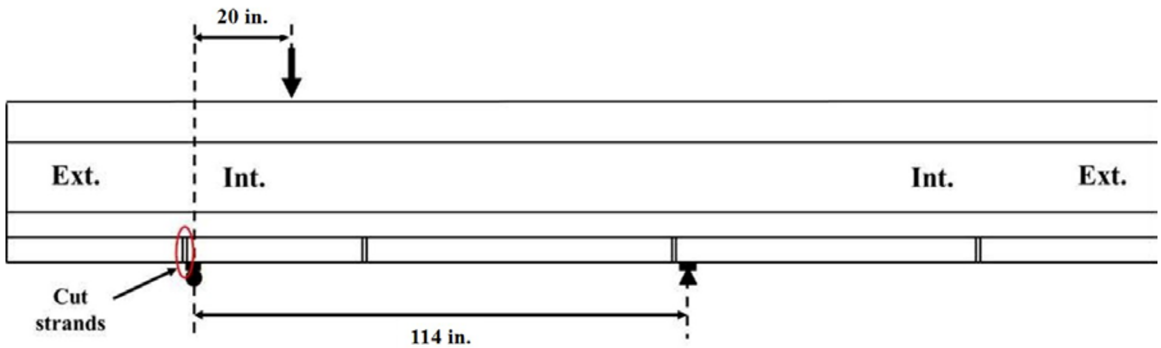

(b) Interior span

Figure 4.3. Three-point bending support locations.

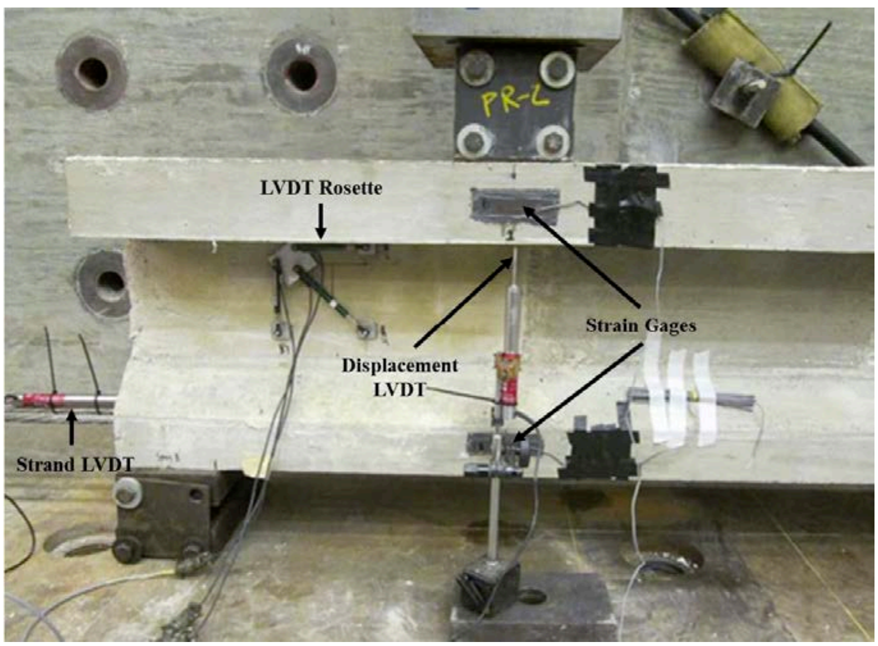

Figure 4.4. Beam instrumentation.

4.2 TEST MATRIX AND BEAM PREPARATION

4.2.1 Test Matrix

The test matrix for this study is shown in Table 4.1. A series of control, damaged, and mortar repaired tests was performed on both exterior and interior spans. GFRP and CFRP laminate repairs were performed on exterior spans, and a CFRP NSM bar repair was performed on an interior span. The compressive strengths of the beam concrete and mortar (if applicable) on the day of testing are shown as well.

Table 4.1. Test Matrix

Test	Cover Damage	Mortar Repair	FRP Repair	Concrete Compressive Strength, MPa (ksi)	Mortar Compressive Strength, MPa (ksi)
Ext. Control	--	--	--	49.4 (7.16)	--
Ext. Damaged	X	--	--	48.7 (7.06)	--
Ext. Mortar	X	X	--	49.4 (7.16)	23.4 (3.39)
Int. Control	--	--	--	48.7 (7.06)	--
Int. Damaged	X	--	--	49.4 (7.16)	--
Int. Mortar	X	X	--	49.6 (7.19)	27.2 (3.94)
GFRP Laminate	X	X	X	49.8 (7.22)	29.0 (4.21)
CFRP Laminate	X	X	X	48.7 (7.06)	27.5 (3.99)
CFRP NSM Bars	X	X	X	49.8 (7.22)	29.0 (4.21)

4.2.2 Damage and Repair of Beam Ends

In order to observe the effect on shear capacity of the types of deterioration seen in the field, damages were imposed on the beam ends for all tests but the control. Since shear capacity is the critical component being investigated, damages were only applied to the web of the beams prior to testing. This also allowed the damages to be easily reproduced for consistency between the different spans tested. Over the entire shear span for all tests with cover damage, the concrete cover was removed to a depth of 12.7 mm (0.5 in.), or to approximately the centerline of the threaded rod stirrups, from the entire web. The concrete cover removal process is illustrated in Figure 4.5. First, a grid of holes was drilled 12.7 mm (0.5 in.) deep using a hammer drill with a 9.5 mm (0.375 in.) diameter drill bit. Then, the cover was removed using a hammer drill with a chisel attachment, being careful not to damage the stirrups. The damaged region was vacuumed and air blasted to remove any concrete particles and dust from the surface. The removal of the concrete cover resulted in a 33% reduction in the width and cross-sectional area of the beam web.

(a) Grid of 12.7 mm (0.5 in.) deep holes

(b) Beam after cover removal

Figure 4.5. Concrete cover removal.

When repairing the concrete cover, it was necessary to choose a fast setting mortar that would allow for quick application of the FRP material. A target compressive strength of around 27.6 MPa (4 ksi) on the day of testing was desired, typical of normal strength concrete. Rapid Set Mortar Mix provided by CTS Cement, Inc. was selected to meet these requirements. The manufacturer's data (CTS Cement 2016) claims strength of 34.5 MPa (5 ksi) at 24 hours and 37.9 MPa (5.5 ksi) at 7 days. The mortar strength was tested at 3 days (the day of beam testing) for all tests where a mortar repair was implemented. The mortar strengths achieved were close to the27.6 MPa (4 ksi) target strength, which was lower than the strength provided by the manufacturer. In addition to a quick setting mortar, both GFRP and CFRP externally bonded laminates and CFRP bars were used as repair materials in this study. The dimensions of the FRP systems used in the tests and the material properties are summarized in Table 4.2. The material properties are based on coupon tests performed in the laboratory. The FRP laminate and FRP bar materials were provided by QuakeWrap, Inc. (QuakeWrap 2016b,c) and Hughes Brothers, Inc. (Hughes Brothers 2011b), respectively.

Due to the presence of the bearing plate, externally bonded U-wrap schemes may not be feasible in the field due to limited access to the bottom of the girder. Therefore, this study focused on bonded face ply FRP repair schemes. Due to this limitation, only bonded face ply FRP laminate repair schemes are investigated in this study, and the FRP shear reinforcement is terminated at the bottom edge of the bottom flange. Vertical fiber orientation (90°) is used for the FRP shear reinforcement. Eight 152.4 mm (6 in.) wide panels of FRP shear reinforcement (four per side) were placed starting 12.7 mm (0.5 in.) from the beam end, with 12.7 mm (0.5 in.) between each panel. Due to the relative stiffness of the GFRP compared to the CFRP, more plies of GFRP were used in order to obtain similar loads in the FRP for similar effective strain values. Three plies of GFRP were chosen based on the ratio of the manufacturer's elastic modulus for CFRP to that of GFRP.

Table 4.2. Material Properties of FRP Systems

Material	Size[a], mm (in.)	Shear Reinforcement Details[b]	Source	Elastic Modulus, GPa (ksi)	Tensile Strength, MPa (ksi)	Tensile Strain, mm/mm (in./in.)
GFRP laminate	1.27 (0.05)	8 x 152.44 mm (6 in.) x 3 plies	Manufacturer	27.4 (3,980)	587 (85.2)	0.023
			Laboratory	22.2 (3,200)	399 (57.9)	0.018
CFRP laminate	1.24 (0.049)	8 x 152.4 mm (6 in.) x 1 ply	Manufacturer	86.9 (13,000)	930 (135)	0.0098
			Laboratory	91.7 (13,296)	1,020 (147.9)	0.011
CFRP bars	6.35 (0.25)	8 bars in web (90°), 2 bars in bottom flange (0°)	Manufacturer	124 (18,000)	2,241 (325)	0.0181
			Laboratory	137.9 (20,000)	2,461 (357)	0.0213

[a]Ply thickness for laminates, bar diameter for bar

[b]Quantity x width x number of plies for laminates

In an effort to delay debonding of the FRP shear reinforcement, an anchoring scheme was implemented at the points of termination as well as at the web/bottom flange junction. Khalifa et al.

(2000) used an anchorage system that consisted of embedding a portion of the FRP shear wrap into a groove cut into the top flange. The FRP laminate is anchored in place by inserting an FRP bar into the longitudinal notch and filling the notch with epoxy. While shown to be effective, this method requires considerable labor in cutting the notch and installing the FRP bar. Mechanical anchorage schemes were implemented by Schuman (2004), including the use of bonded steel anchors with bearing plates and GFRP plate anchors. Mechanical anchorages also require increased labor to drill and anchor the bolts through the beam web. Belarbi et al. (2011) used mechanical anchorage systems (continuous and discontinuous CFRP plates) as well as horizontal FRP strips. Hutchinson and Rizkalla (1999) also used horizontal strips, and reported an increase in shear contribution of FRP by 16%. Miller (2006) used horizontal strips over 45°CFRP shear reinforcement as web-flange connectors to distribute the forces caused by tension in the diagonal CFRP at the web-bottom flange interface. The horizontal strip anchorage technique, unlike others, is simple to apply and requires little labor and none of the extra tools or skills associated with the other anchorage systems. For these reasons, this anchorage system was chosen for these tests.

Figure 4.6 shows the design of the FRP laminate repairs used in this study. Longitudinal anchors of the same FRP material used for shear reinforcement were placed at the top of the web, the bottom of the web, and along the bottom edge of the bottom flange. In order to increase development of the anchors at the beam end, the anchors were wrapped around the end of the beam and continued along the other side. It is possible that the space constraints could prevent the proper adherence of the FRP anchor to the end of the beam. As a result, the anchors were left unsaturated with epoxy and unbonded to the web where they loop around the beam end. Horizontal fiber orientation (0°) was used for the anchors. The widths of the two web anchors were 50.8 mm (2 in.), while the width of the bottom flange anchor was 38.1 mm (1.5 in.) to allow it to pass underneath the prestressing strands, which protruded from the end of the beam. In addition to the instrumentation shown in Figure 4.4, a strain gage was placed vertically on the FRP shear laminate closest to the center of the shear span (see Figure 4.6) to measure the strain obtained in the FRP laminate.

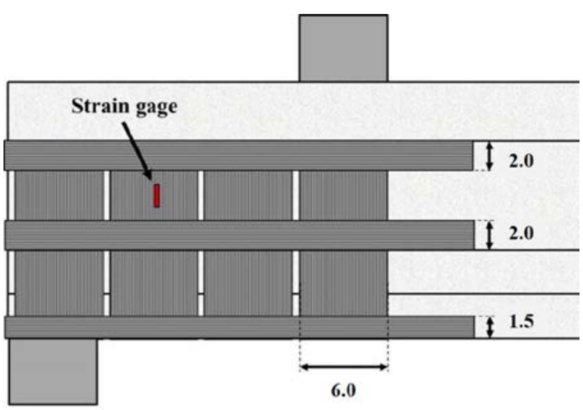

(a) FRP repair dimensions (in.)

(b) FRP strain gage

Figure 4.6. FRP laminate repair design.

The FRP laminate repair process is illustrated in Figure 4.7. After the mortar had set for 24 hours, the surface was prepared using an angle grinder with a diamond tipped concrete blade. Surface preparation was performed on both the mortar repaired surface web and the original concrete along the bottom flange. The surface was vacuumed and air blasted to remove dust and laitance. Next, the concrete surface was saturated with the two-part epoxy resin. Once the resin became tacky, FRP sheets were applied. The FRP sheets were then saturated with epoxy resin, and in the case of GFRP more plies were added. When applying multiple layers of GFRP, we observed that the increased thickness caused a tendency for the laminate to detach from the concrete at both of the angles in the bottom flange. We were extra careful to make sure the first layer was sufficiently bonded to the concrete before adding subsequent plies. After the FRP shear wraps were saturated, the longitudinal anchors were applied and fully saturated. The epoxy was allowed to set for 48 hours prior to testing.

(a) Surface grinding (b) Epoxy saturation of concrete (c) Applying shear CFRP

(d) Saturating CFRP anchors (e) Applying shear GFRP (f) Saturating GFRP anchors

Figure 4.7. FRP laminate repair process.

Figure 4.8 shows the design of the CFRP NSM bar repair used in this study. Eight vertical CFRP bars were placed within the web portion of the beam, evenly spaced across the shear span at 50.8 mm (2 in.). Due to the inability of the bars in the web to bridge cracks in the bottom flange, two longitudinal bars were placed in the bottom flange. The 610 mm (24 in.) long bars were placed starting at the notch location (which was functioning as the beam end). This allowed for some development of the bar before the region of anticipated shear cracks. In addition to the instrumentation shown in Figure 4.4 (minus the LVDT measuring strand end-slip), strain gages were placed on one vertical and one longitudinal CFRP bar (see Figure 4.8) to measure the strain obtained in the CFRP bars. These strain gages were located in regions of the highest expected strains based on the cracking patterns observed in previous tests.

The CFRP bar repair process is illustrated in Figure 4.9. One difficulty presented by the small-scale of the beam was cutting the notches for in the web for the vertical CFRP NSM bars. Due to the geometry of the top flange, it was not possible to cut a notch all the way to the bottom of the top flange using a circular saw with an 86 mm (3.38 in.) diamond grit blade. Therefore, we needed to maximize the development length and thus the strain capacity of the NSM bar repair. In order to accomplish this, an alternative technique was used to create these notches. During the mortar repair process for this span, 11.1 x 11.1 x 190 mm (0.44 x 0.44 x 7.5 in.) stiff foam pieces were placed within the repaired web region in order to preform notches in the mortar repair. The width and depth of these foam pieces were slightly greater than the minimum groove dimension 1.5db (9.5 mm, or 0.38 in.) required by ACI 440.2R-08(ACI 2008) for NSM FRP bar reinforcement. This was to ensure that the CFRP bars would fit in the resulting groove, even if any slight misalignment or deformation in the foam was caused by the mortar application. After the mortar repair had set, the foam was removed from the groove using a flathead screwdriver. Since the bottom flange was both easily accessible and not affected by the damage/mortar repair process, the two longitudinal grooves were cut using the circular saw with a diamond grit blade. Two longitudinal cuts were made at the furthest extents of the groove, and the remaining portion of concrete along the middle of the groove was chiseled away. From here, the same repair process explained in Chapter 2 was performed. The interior surfaces of the grooves were vacuumed and air blasted to remove dust and laitance. Then, masking tape was applied along the edges of the grooves. The grooves were filled halfway with epoxy, the CFRP bars were inserted, and then the groove was completely filled. The excess epoxy was then troweled away and the tape removed. The repair was allowed to set for 48 hours prior to testing.

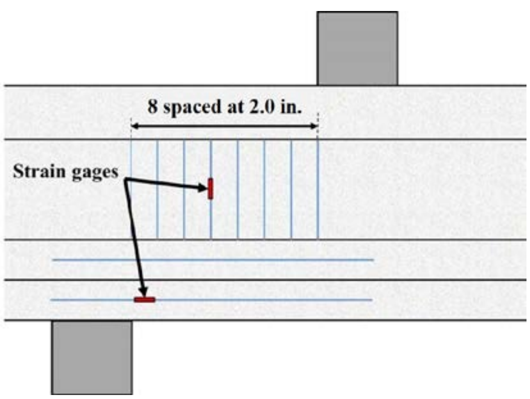

(a) FRP NSM bar layout and spacing

(b) Strain gage locations

Figure 4.8. FRP NSM bar repair design and instrumentation.

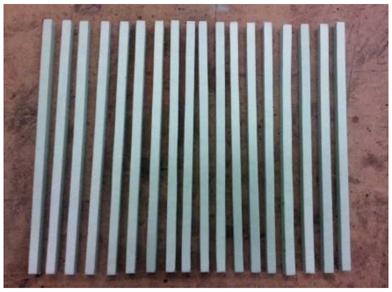

(a) Foam notch fillers cut

(b) Mortar repair with foam notch placed

(c) Foam removed and longitudinal notches marked

(d) Notches taped after cutting longitudinal notches

(e) Applying Hilti HIT-RE 500 epoxy

(f) Final repair after troweling and removing tape

Figure 4.9. FRP NSM bar repair process.

4.3 TEST RESULTS

A summary of the test results is presented in Table 4.3. Figure 4.10 shows the load vs. deflection curves for all five tests involving exterior spans. Figure 4.11 shows the load vs. strand end-slip curves for these five tests. Figure 4.12 shows the load vs. deflection curves for the four tests involving interior spans. Stiffness was calculated as the secant line from the origin to the point on the load vs. deflection curve corresponding to approximately 2 mm (0.08 in.) of deflection (where nonlinear behavior initiates for some tests). The beam failures were caused by one of two reasons. The first is shear cracking along the diagonal compression strut of the beam as in the cases of Control, Damaged, and Mortar specimens. The other reason could have been the debonding of the FRP as in the GFRP, CFRP, and CFRP NSM bar specimens. The strand end-slip did not seem to influence the failure mode of the beams. Strand end-slip at peak load generally correlated with the amount of deflection reached at peak load, regardless of failure mode.

Table 4.3. Test Results

<table>
<tr><th>Specimen</th><th>Peak Load, kN (kips)</th><th>% of Control Peak Load</th><th>% of Control Stiffness</th><th>Strand Slip at Peak Load, mm (in.)</th><th>Max. Principle Strain in the Web at Peak Load, mm/mm (in./in.)</th><th>Max. FRP Strain, mm/mm (in./in.)</th></tr>
<tr><td>Ext. Control</td><td>282.9 (63.6)</td><td>100.0</td><td>100.0</td><td>1.81 (0.071)</td><td>0.0153</td><td>--</td></tr>
<tr><td>Ext. Damaged</td><td>206.4 (46.4)</td><td>73.0</td><td>75.9</td><td>0.46 (0.018)</td><td>0.0063</td><td>--</td></tr>
<tr><td>Ext. Mortar</td><td>229.5 (51.6)</td><td>81.1</td><td>78.9</td><td>0.51 (0.020)</td><td>0.0062</td><td>--</td></tr>
<tr><td>GFRP</td><td>288.7 (64.9)</td><td>102.0</td><td>74.4</td><td>2.03 (0.080)</td><td>0.0108</td><td>0.0012</td></tr>
<tr><td>CFRP</td><td>338.0 (76.0)</td><td>119.5</td><td>106.0</td><td>1.33 (0.052)</td><td>0.0065</td><td>0.0034</td></tr>
<tr><td>Int. Control</td><td>405.9 (91.3)</td><td>100.0</td><td>100.0</td><td>--</td><td>0.0228</td><td>--</td></tr>
<tr><td>Int. Damaged</td><td>289.8 (65.1)</td><td>71.4</td><td>86.5</td><td>--</td><td>0.0204</td><td>--</td></tr>
<tr><td>Int. Mortar</td><td>326.9 (73.5)</td><td>80.5</td><td>88.4</td><td>--</td><td>0.0136</td><td>--</td></tr>
<tr><td rowspan="2">CFRP NSM Bars</td><td rowspan="2">319.1 (71.7)</td><td rowspan="2">78.6</td><td rowspan="2">92.5</td><td rowspan="2">--</td><td rowspan="2">0.0087</td><td>0.00098 (vert.)</td></tr>
<tr><td>0.0063 (long.)</td></tr>
</table>

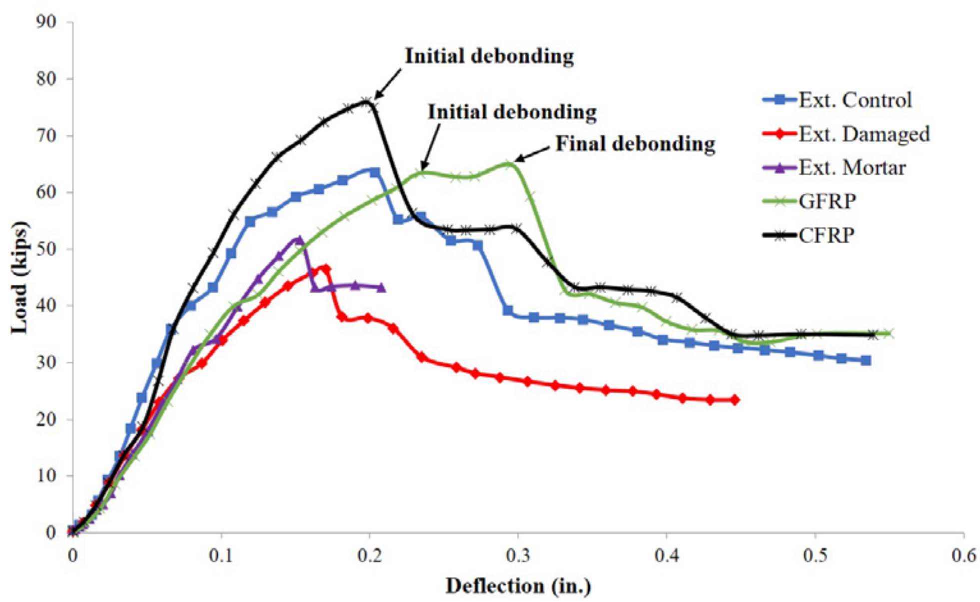

Figure 4.10. Load vs. deflection curves for exterior spans.

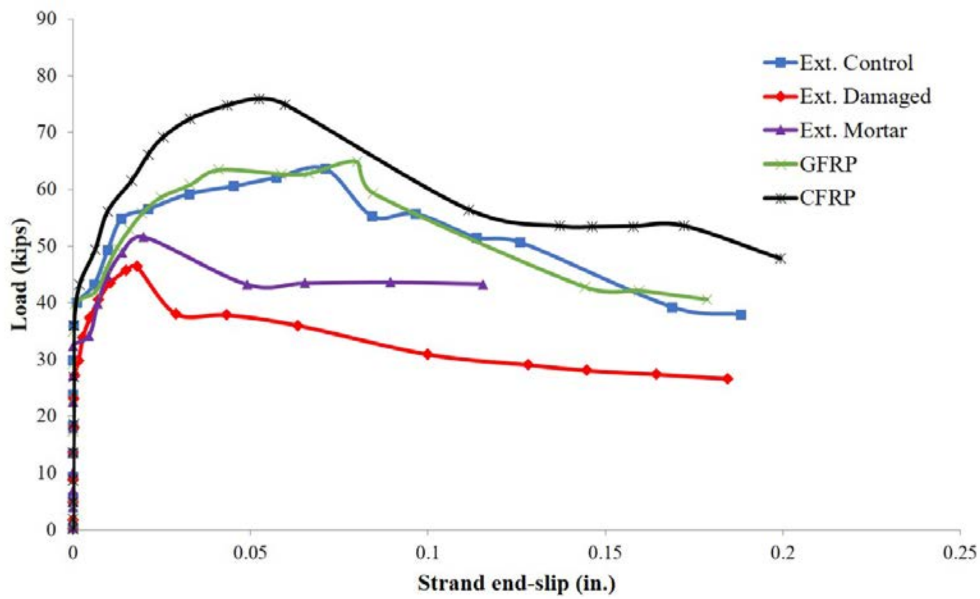

Figure 4.11. Load vs. strand end-slip curves for exterior spans.

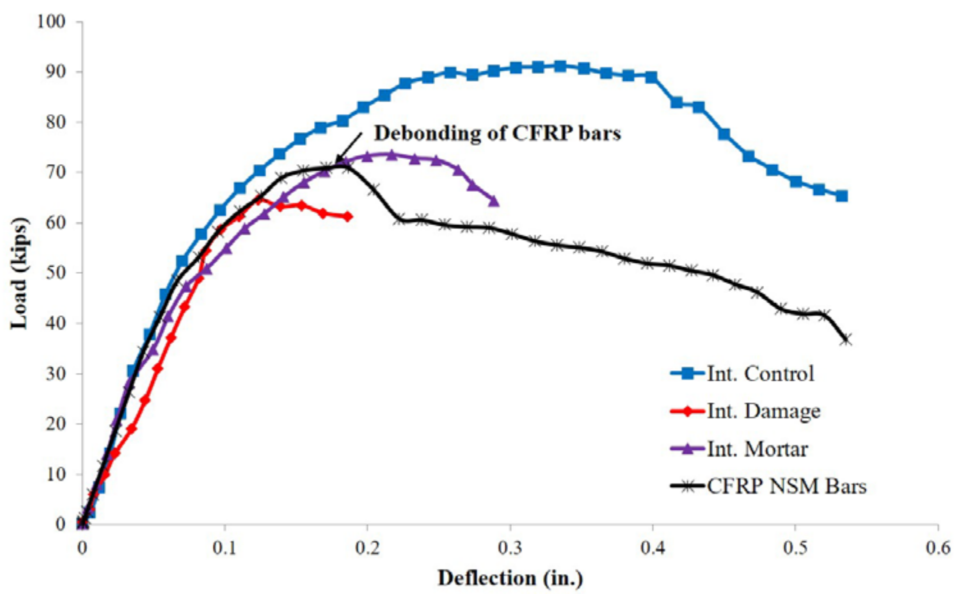

Figure 4.12. Load vs. deflection curves for interior spans.

4.4 DISCUSSION

4.4.1 Effect of Cover Damage and Mortar Repair

As illustrated in Figures 4.10 and 4.12, the removal of the concrete cover resulted in decreases in both peak load and stiffness from the control. For example, the Exterior Damaged test reached 73% of the peak load and 75.9% of the stiffness of the Exterior Control. The additional mortar repair recovered some of the strength and stiffness lost due to the cover damage. The Exterior Mortar test reached 81.1% of the peak load and 78.9% of the stiffness of the Exterior Control. The series of interior span tests performed similarly as the exterior spans in terms of comparing the Control, Damaged, and Mortar tests. However, these spans were slightly stronger and stiffer overall. This could be attributed to the fact that the stress transfer had already taken place at the time of strand cutting, so more pretensioning was applied to the interior spans than the exterior spans. The maximum principal strains at peak load for the Exterior Control and Exterior Damaged cases were .0153 and .0063, respectively. However, the maximum principal strain did not increase with the addition of the mortar repair, suggesting the mortar cover is not engaging with the core concrete. The fact that the compressive strength of the mortar was less than that of the beam concrete (23.4 MPa (3.39 ksi) for mortar vs. 49.4 MPa (7.16 ksi) for concrete), offers a conservative estimation of the effect which a normal strength mortar would have if used in the repair of damaged end regions of beams similar to the ones tested in this study.

In addition to the reduced mortar compressive strength, the contribution of the applied mortar to the shear capacity of the repaired end region could also be limited. This is due to the cold joint that exists between the exposed core concrete and the mortar repair. At this interface, reduced aggregate interlock diminishes the strength recovery effect of the mortar repair. This phenomenon is also suggested by looking at the cracking patterns shown in Figure 4.13 for the Control and Mortar tests. In the case of Control test (Figure 4.13(a)), the shear cracks propagate in a nearly direct path from the support to the loading plate. In the case of Mortar test (Figure 4.13(b)), the shear cracks travel along the web/bottom flange junction in the region above the support before proceeding up through the web at an approximately 45° angle in the center of the shear span. This change in cracking pattern shows the propensity of cracks to propagate through the weak interface between the concrete and mortar, thus reducing the ability of the mortar repair to contribute to the shear strength of the beam. The cracking patterns for the interior spans were similar to their respective exterior span tests. Overall, this series of tests illustrates that a conventional mortar repair alone is not sufficient to recover the shear strength and stiffness of a beam with severely damaged cover concrete at the beam end.

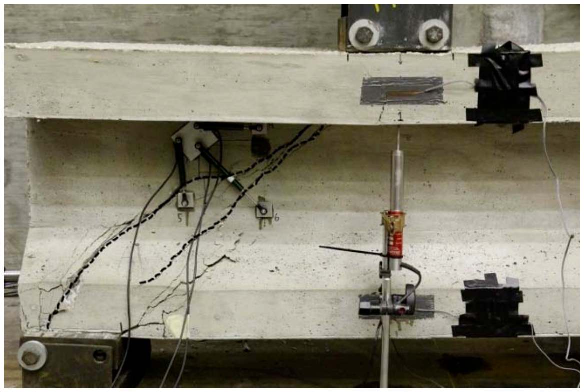

(a) Control

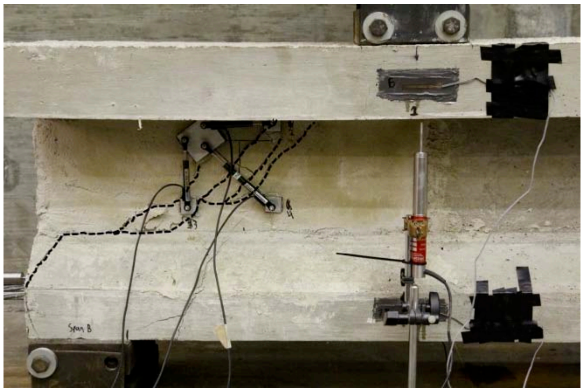

(b) Mortar

Figure 4.13. Cracking patterns in Exterior Control and Mortar tests.

4.4.2 Discussion on the Effect of FRP Laminate Repair

As illustrated in Figure 4.10 and Table 4.3, the addition of externally bonded FRP shear reinforcement resulted in increases in stiffness and strength from the Mortar test for CFRP, but only an increase in strength for GFRP. The GFRP test reached 102% of the peak load and 74.4% of the stiffness of the Control, whereas the CFRP test reached 119.5% of the peak load and 106.0% of the stiffness of the Control. The immediate drop in the force vs. deflection curves after peak load for each of these tests was associated with the debonding of the FRP shear reinforcement and is considered the failure point for these tests. For the CFRP test, debonding initiated in the endmost FRP shear panel, just above the web/bottom flange junction anchor (see Figure 4.14(a)), causing the first drop in the curve (see Figure 4.10).

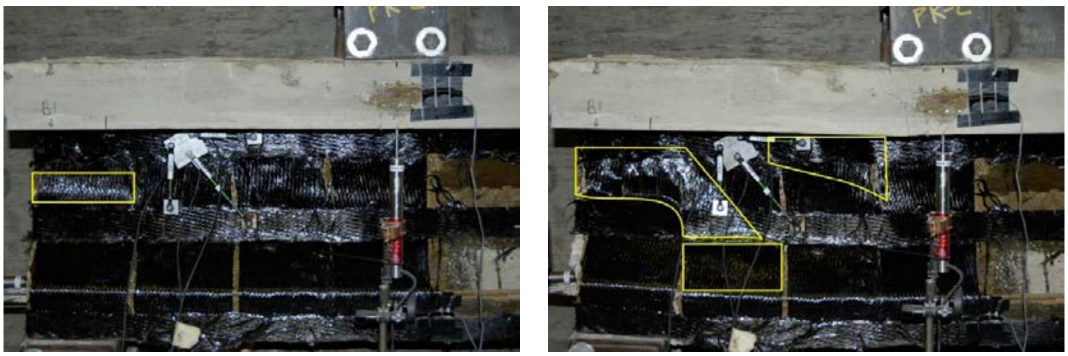

(a) CFRP: initial debonding (b) CFRP: final debonding

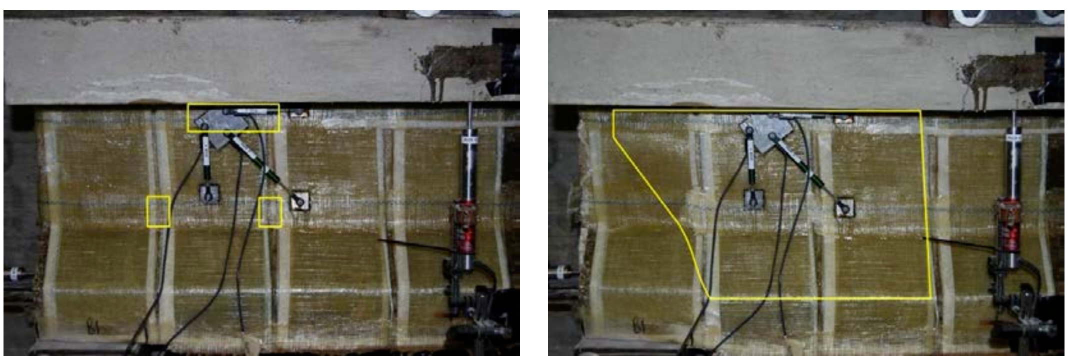

(c) GFRP: initial debonding (d) GFRP: final debonding

Figure 4.14. Debonding in FRP repairs.

As debonding in the first panel proceeded up the web, stresses were shifted to the adjacent shear panel, in which debonding subsequently initiated (see Figure 4.14(b)). The top web anchor was able to prevent complete delamination of the FRP reinforcement at the top of the web, at least until the beam had been loaded significantly past failure. The test was stopped after deformation caused a complete shearing of the beam between the first and second shear panels (which coincided with the edge of the support), causing the second panel from the end to delaminate along the sloped portion of the bottom flange.

In the GFRP test, the debonding initiated almost simultaneously at web/bottom flange junction on either side of the second panel and the top of the web along the second panel (see Figure 4.14(c)). In this case, the horizontal anchors were ineffective in preventing complete debonding. The first three panels ultimately debonded together from the top of the web (see Figure 4.14(d)), at strains much lower than those which were achieved in the CFRP (see Table 4.3). Unlike the CFRP test, the peak load was not controlled by initial debonding (see Figure 4.10), but by subsequent debonding.

The ineffectiveness of the anchors in the case of GFRP can be attributed to the increased thickness of the FRP shear reinforcement due to having three plies. This created difficulty in getting the anchors to bond to the concrete in the 12.7 mm (0.5 in.) gap between shear panels. Without sufficient anchor development between the shear panels, the anchors were essentially effective only at the furthest extents of the FRP repair, where there was either the loop around the beam end or sufficient development. It is possible that the horizontal anchors were actually detrimental in the case of the GFRP. Once debonding initiated at the top of the web for one panel, the anchor could have prompted debonding at an adjacent panel due to its direct connection between the two panels and insufficient development between the panels.

The overall effectiveness of both types of FRP laminates could also have been limited by the low shear span-to-depth ratio used in these tests. Since the arching action mechanism for shear transfer governs over traditional shear transfer, the cracking and debonding behavior likely differs from situations in which a larger shear span-to-depth ratio is used. Externally bonded FRP shear reinforcement has already been proven in other studies to be effective for larger a/d ratios. The purpose of this study was to examine if any effectiveness could be observed using this technique for localized end region damage, thus limiting the results of these tests to this specific application.

4.4.3 Discussion on the Effect of CFRP NSM Bar Repair

As illustrated in Figure 4.12 and Table 4.3, the addition of the CFRP NSM bar repair resulted in only a slight increase in stiffness and a slight decrease in strength from the interior Mortar test. The CFRP NSM bar repaired span reached just 78.6% of the peak load and 92.5% of the stiffness of the interior Control. The drop in the force vs. deflection curves after peak load for this test was associated with the debonding of the vertical CFRP bars in the web at the epoxy/mortar interface and is considered the failure point for this test. Debonding also occurred at the epoxy/mortar interface for the longitudinal bars, but this occurred after the failure of the beam.

The cause of the overall ineffectiveness of the CFRP NSM bar repair is evident when observing the cracking patterns in the span. As shown in Figure 4.15(a), the longitudinal CFRP bars in the bottom flange were successful in bridging the shear cracks. The vertical bars in the web, however, were largely ineffective. A large crack initiated at the termination point of the uppermost longitudinal bar and proceeded along the web/bottom flange interface, which was also the line of termination for the mortar repair. Once reaching the 5th vertical bar from the end, the crack turned sharply upwards and proceeded along the epoxy/concrete interface of this bar (see Figure 4.15(b)). The shear cracks that were bridged along the bottom flange also joined this crack at this location. Because the vertical bars were unable to bridge the cracks in the web, the shear capacity of the beam was not increased. There are several factors that may have contributed to this phenomenon. Due to the small-scale of the beam, the development length of the vertical bars may have been insufficient. Additionally, the weak interface between the mortar repair and the existing concrete coincided with the bottom of the notches for the vertical bars. This weak interface promoted cracking at the mortar/concrete interface, which undermined any potential effectiveness of these bars since stresses were not transferred evenly through the concrete and mortar. On one side of the beam large pieces of the mortar repair spalled away from the beam web. This was due to the combination of the weak mortar/concrete interface and the tendency for the cracking in the web to propagate between the vertical bars (see Figures 4.16(c)-(d)).

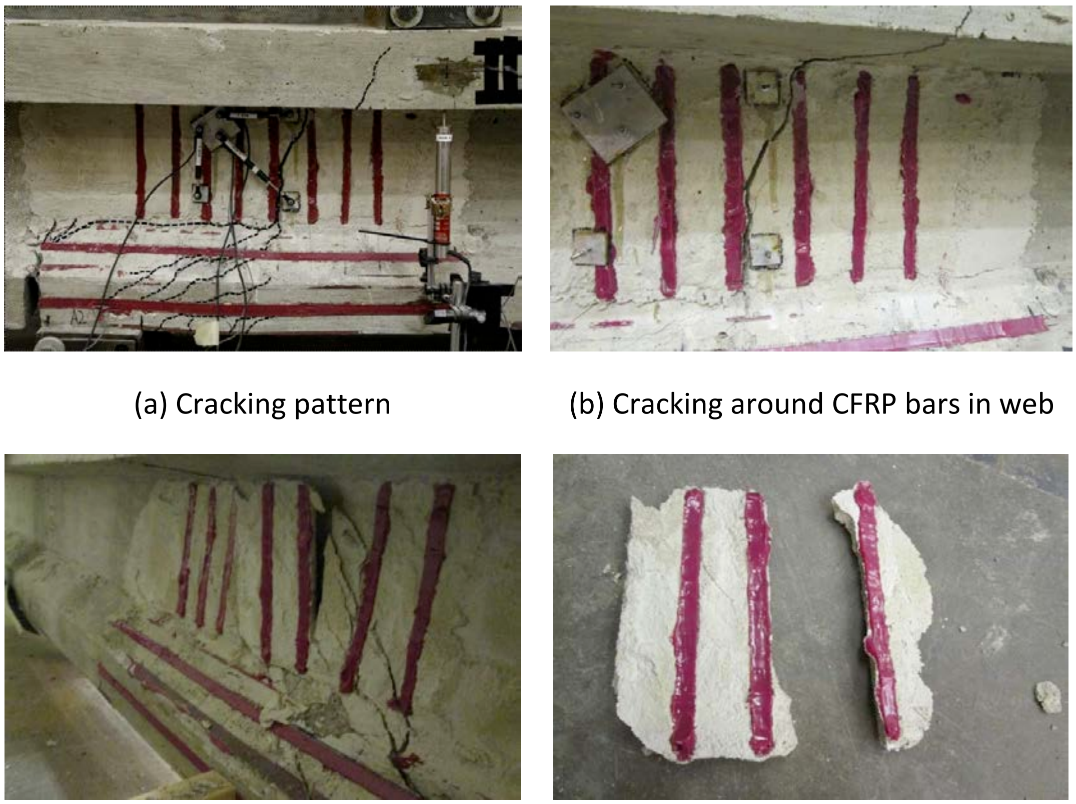

(a) Cracking pattern

(b) Cracking around CFRP bars in web

(c) Debonding at epoxy/concrete interface

(d) Debonded section of mortar

Figure 4.15. Cracking and debonding in CFRP NSM bar repair.

As shown in Table 4.3, the strain in the bottom longitudinal bar reached 6300 $\mu\varepsilon$ compared to just 980 $\mu\varepsilon$ for the vertical bar. This furthers the notion that presence of the mortar repair was the main cause for the ineffectiveness of the vertical bars and the CFRP NSM bar repair as a whole. Because the notches in the bottom flange were cut in the original concrete, there was no weak interface coinciding with the bottom of the notch. This allowed the stresses in the concrete to be transferred effectively to the CFRP bars. The longitudinal bars also benefited from an increased development length over the vertical bars. Additionally, the termination points for the longitudinal bars were not located in region of high stress like the termination points for the vertical bars. This forced the cracks to propagate across the bars, instead of taking an easier path around the ends of the bars. Because of the high strains observed in the longitudinal bars, this repair method shows potential to be effective despite the results of this test. In a full-scale beam test, the bars in the web would have greater development length, similar to that of the longitudinal bars used in this small-scale beam test. Using bars at 45° in the web would both increase the development length further and promote crack propagation across the bars. However, in the case of severe cover concrete damage requiring an extensive mortar repair, the results of these tests indicate that the NSM bar repair technique would likely be an inferior repair scheme to FRP laminates.

CHAPTER 5: FLEXURAL TESTS OF FULL-SCALE GIRDERS

In this chapter, three-point bending tests were conducted on Full-scale prestressed girders retrieved from the field. The girders were tested before and after being repaired using CFRP laminates. The purpose of the tests was to examine if the repair technique that was effective in repairing and retrofitting damaged small-scale beams could also improve the shear behavior of the damaged full-scale girders. Therefore, the same preparation process and testing procedure was adopted to investigate the effectiveness of CFRP laminates to restore the shear capacity of the girders with damaged end regions.

5.1 SPECIMEN DESCRIPTION AND TEST SETUP

5.1.1 Girder Specimen Description

Five AASHTO Type II prestressed girders that were in service in the State of Illinois for over 40 years were extracted from a bridge and shipped to lab at the University of Illinois at Urbana-Champaign as shown in Figure 5.1. Two of the girders has length equal to 7.9 m (26 ft.) and the rest of the girders were 8.5 m (28 ft.) long. All the girders shared the same cross-section as depicted in Figure C.1 in Appendix C.

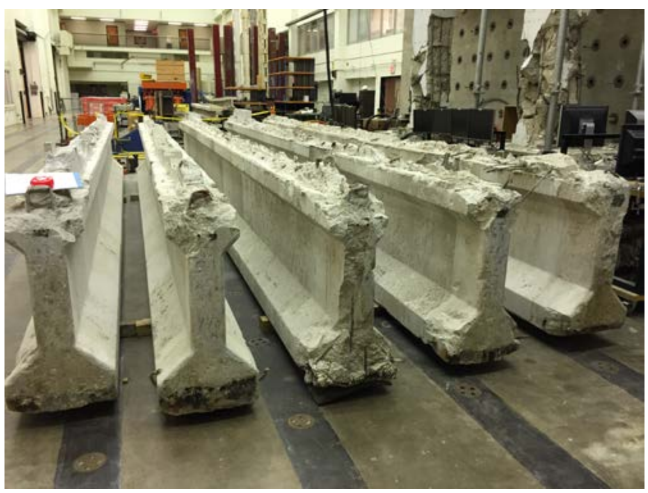

Figure 5.1. AASHTO Type II prestressed girders.

Since the top of the girders were uneven, it was not feasible to apply the load directly on the girders top using an actuator. Therefore, to provide an even bearing area for the actuator, uneven concrete was removed from the top and a 304.8 x 304.8 x 101.6 mm (12 x 12 x 4 in.) block was cast using high strength mortar (Rapid Set Mortar Mix from CTS Cement, Inc.) as shown in Figure 5.2. As per the design plans, the girders were prestressed with six 12.7 mm (0.5 in.) diameter 7-wire stress relieved prestressing strands with an elastic modulus of 186.2 GPa (27,000 ksi) and ultimate strength of 1862 MPa (270 ksi). The strands were pretensioned to 1303 MPa (189 ksi), approximately 70% of their ultimate strength. The mild steel used was Grade 40 with yield strength equal to 276 MPa (40 ksi). With a service life of over 40 years, the compressive strength of the concrete was unknown.

Therefore, after one of the girders was tested, cylinders were drilled from the web of the girder and tested to obtain the compressive strength of the concrete as shown in Figure 5.3. The average compressive strength of concrete was found to be 60.3 MPa (8.75 ksi).

(a) Removal of uneven concrete (b) Casting of grout block

Figure 5.2. Casting of the load bearing grout block.

(a) Drilling cylinder from web (b) Cylinders obtained from web

Figure 5.3. Testing of concrete compressive strength.

5.1.2 Test Setup

Similar to small-scale beam testing, three-point flexural tests were performed on the ends of the girders to obtain the shear capacity of the girder. Due to the localized nature of end damage, a short shear span of 1.25d_p was selected to investigate the shear behavior of the girder. Considering the depth to the prestressting strand from top (d_p) is 863 mm (34 in.), the distance from the center of the support to the center of loading plate was 1079 mm (42.5 in.). The distance from center to center of the support was chosen as 6400 mm (252 in.) such that the other end of the girder was unaffected from the loading. The test setup is illustrated in Figure 5.4.

An actuator with capacity of 1200 kN (270 kips) was used to apply vertical displacement to conduct flexural testing. The vertical deflection of the girder was measured by placing a LVDT under the girder at loading point. Three LVDTs installed on the web at 0°, 45°, and 90° formed a rosette configuration to measure the averaged strain within web during loading and calculate the principal strain afterwards. Two strain gages were placed at top and bottom flange to measure the compressive and tensile strain of concrete during loading. Figure 5.5 shows the instrumentation used in the test.

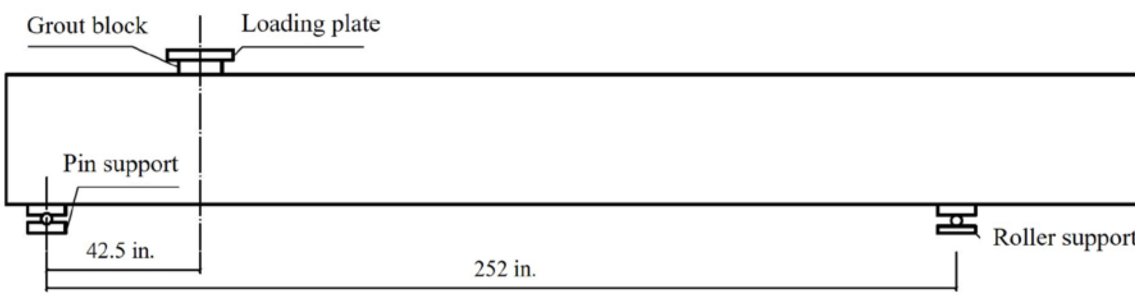

Figure 5.4. Three-point flexural testing.

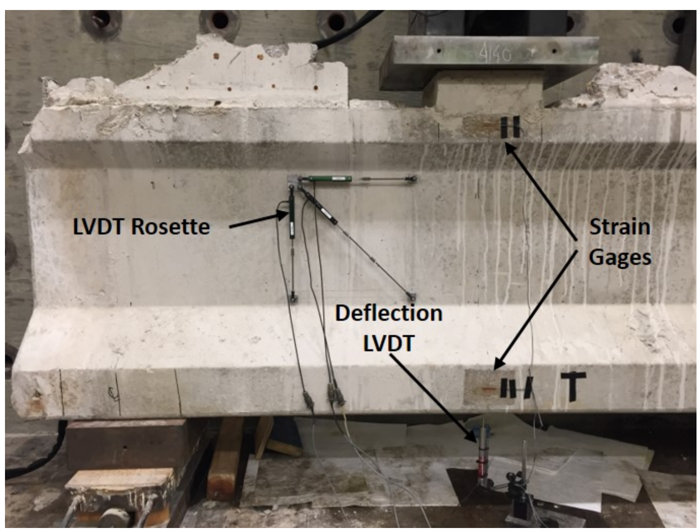

Figure 5.5. Girder instrumentation.

5.2 TEST MATRIX AND GIRDER PREPARATION

5.2.1 Test Matrix

The test matrix for full-scale girder testing is listed in Table 5.1. The testing included control, damaged, and mortar repair cases. Based on test results of small-scale beams, CFRP laminate repair showed more promising results than GFRP laminate and CFRP NSM bar repairs, therefore, in full-scale girder testing, only CFRP laminate repair was considered. The mortar compressive strength on the day of testing that was used in the repair process is also listed in the table.

Table 5.1. Test Matrix

Test	Cover Damage	Mortar Repair	FRP Repair	Concrete Compressive Strength, MPa (ksi)	Mortar Compressive Strength, MPa (ksi)
Control	--	--	--	60.3 (8.75)	--
Damaged	X	--	--	60.3 (8.75)	--
Mortar	X	X	--	--	41.7 (6.05)
CFRP Laminate	X	X	X	--	54.1 (7.82)

5.2.2 Damage and Repair of Girder Ends

To mimic the damage/deterioration that girders are subjected to at their end regions during service life, the concrete cover was removed. Unlike the small-scale beams, for full-scale girders, the concrete cover was removed from the web through bottom flange. This is needed in order to introduce a more severe and practical damage pattern. For all the cases except the Control case, concrete cover was removed to approximately the centerline of the stirrups. To remove the cover, first, a grid of holes with a depth to the centerline of stirrups was drilled. The grid served two purposes: one was to control the depth of the concrete cover removed; the other was to ease the removal process after drilling. Then, a hammer drill with a chisel was utilized to remove the cover. The removal procedure is shown in Figure 5.6.

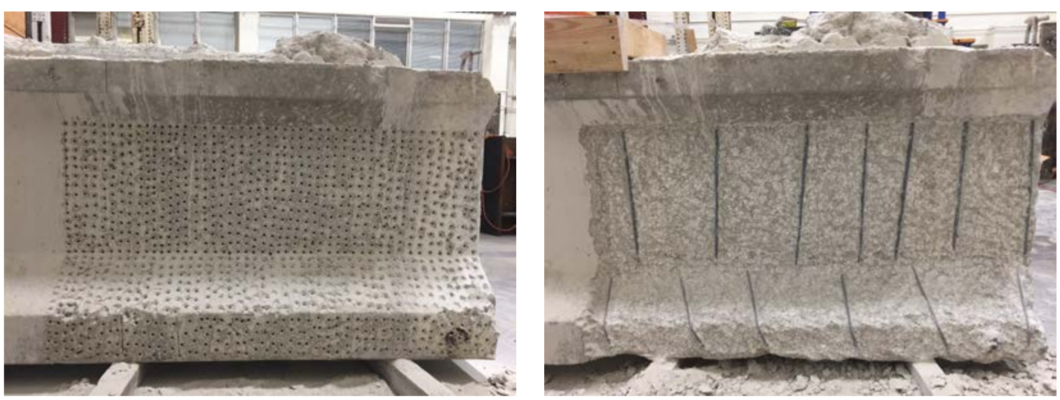

(a) Grid of drilled holes (b) Girder after cover removal

Figure 5.6. Concrete cover removed from web to bottom flange.

After the cover was removed, the exposed surface was air blasted and vacuumed to provide a clean surface for the following repair. It is essential to restore the shape of the damage end before any other repair material such as FRP laminate is applied. To obtain a fast repair, same mortar mix (Rapid Set Mortar Mix from CTS Cement, Inc.) that has been used for repairing small-scale beams was utilized to repair full-scale girders. With a large amount of concrete being removed, it is of great importance to achieve a uniform thickness within the entire shear span. As a result, the following process was adopted. First, a narrow strip of mortar with thickness equal to that of original cover was placed at the edge of the girder. The mortar strip served as the thickness marker to ensure the mortar filled within the shear span would yield same thickness throughout the repaired region. Then, water was sprayed to wet exposed surface and enhance the bond between the mortar and base concrete. A trowel was used to place mortar and obtain the shape of the girder. A long straight wood piece was used to remove extra mortar and smoothen the surface. Hence a roughly even and flat surface was achieved. Last, the mortar surface was wet cured for 1 hour to provide crack-free surface.

After mortar repair, CFRP laminate was applied to the girder. The CFRP laminate used had the same material properties listed in Table 4.2. Due to the blockage of bearing plate and limited space under the girder near end region, an externally bonded U-wrap scheme was not feasible in such case. As a result, the 2-sided FRP repair approach was adopted. The design process of CFRP laminate was as follows. First, the drop in the force (ΔF) between Control and Damage throughout the loading history was obtained from force-deflection curves. Second, corresponding principal tensile strain values (ε_1) were obtained from rosette reading. Since the shear crack was at an angle of about 45° with respect to longitudinal axis of the beam, the vertical component (ε_y) was approximated as $\varepsilon_1 \times cos45°$. Then, the required area of FRP laminate on each side was calculated as $A_{FRP} = \frac{\Delta F/2}{E_{FRP} \times \varepsilon_y}$, where E_{FRP} is the Young's modulus of CFRP and could be obtained from Table 4.2. Finally, the number of CFRP laminates was obtained by dividing A_{FRP} by the length of repaired shear span, *L*. The results calculated using the design process are listed in Table 5.2. An example of this process at deflection of 0.1 in. is shown below.

- ΔF = 11.7 kips at deflection of 0.1 in.
- $\varepsilon_1 = 454\ \mu\varepsilon$ at same deflection
- $\varepsilon_y = \varepsilon_1 \times cos45° = 454 \times cos45° = 321\ \mu\varepsilon$
- $A_{FRP} = \frac{11.7/2}{13000 \times 321 \times 10^{-6}} = 1.40\ in^2$
- No. of FRP laminate = $\frac{1.40}{42.5 \times 0.049} = 1$

Table 5.2. Design of CFRP laminate

Deflection, mm (in.)	ΔF, kN (kips)	ε_1, $\mu\varepsilon$	ε_y, $\mu\varepsilon$	Area of CFRP, mm^2 (in^2)	No. of CFRP laminate
1.5 (0.06)	89.0 (20.0)	150	106.11	4574.2 (7.09)	4
2.5 (0.1)	52.0 (11.7)	454	321.15	883.9 (1.37)	1
5.1 (0.2)	30.7 (6.9)	1500	1061.08	154.8 (0.24)	< 1
7.6 (0.3)	17.8 (4.0)	2450	1733.1	58.1 (0.09)	< 1
10.2 (0.4)	16.5 (3.7)	3469	2453.93	38.7 (0.06)	< 1

It should be noted that using the maximum value of ΔF in this process is not practical as it corresponds to a very small ε_1 value (notice the sudden jump in the number of CFRP laminates between deflections of 0.06 in. and 0.1 in.). This will result in the overdesign of CFRP. Therefore, based on the results shown in Table 5.2, it was deemed sufficient and more economical to use one layer of CFRP laminate.

FRP laminate with vertical fiber orientation (90°) started from the web and terminated at bottom of the beam. On each side of the girder, four panels of one layer of FRP sheet with a width of 279 mm (11 in.) were applied starting from the center of the supporting plate and spaced at 25.4 mm (1 in.). Three longitudinal strips of CFRP laminate with horizontal fiber orientation (0°) were placed above panels, serving as anchorage system. Each strip was 1498 mm (59 in.) long and 76.2 mm (3 in.) wide. Unlike the small-scale beam where longitudinal strip looped around the end of the beam, the longitudinal strip applied to full-scale girder extended 152.4 mm (6 in.) from the first and last panel. This is because in the field it might not be feasible to wrap FRP strip around the end of the girder when there is limited space around the end region. A strain gage was attached to the third panel to measure the strain developed within FRP sheet. The CFRP repair system is depicted in Figure 5.7.

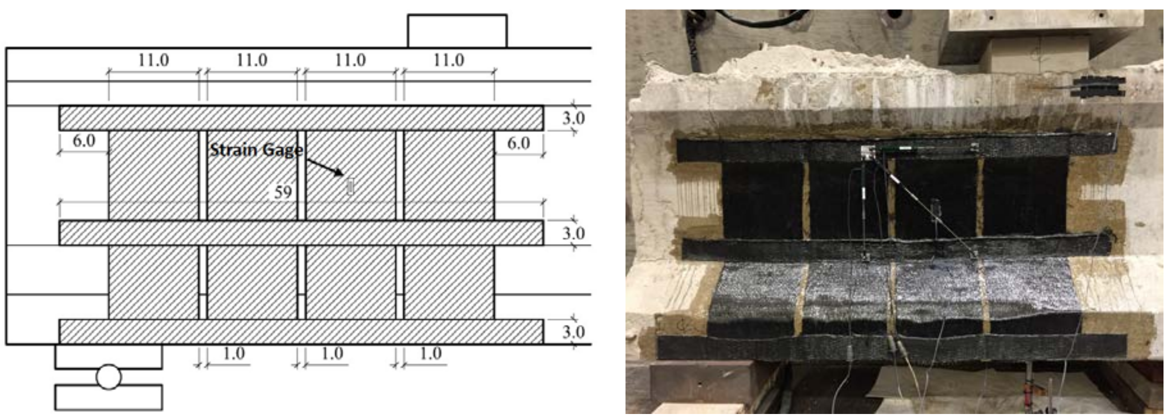

(a) CFRP laminate dimensions (in.)　　　　(b) CFRP test setup

Figure 5.7. CFRP laminate repair design.

To apply CFRP laminates using the wet layup method, first, the mortar surface was grinded using a diamond tipped blade to provide a rough surface and increase the bond between epoxy and mortar. Then, a thin layer of two-part epoxy was applied to saturate the surface. Afterwards, a CFRP panel was placed to the surface and pressured by hand to remove any air bubbles under the panel. After four panels were attached, epoxy was applied to saturate the laminates.

The same process was repeated to apply longitudinal strip. The epoxy was allowed to set for 48 hours. The procedure is shown in Figure 5.8.



(a) Surface grinding (b) Resin application (c) FRP laminates application


(d) Saturating laminates with resin (e) Applying longitudinal strips

Figure 5.8. Process of applying CFRP laminates.

5.3 TEST RESULTS

Only two girders were needed to complete the four tests required for the study. A summary of the four three-point flexural test results is presented in Table 5.3. The yielding point is selected as the point where the load vs. deflection curve showed significant nonlinearity. The ductility is defined as the ratio between ultimate deflection and deflection at yielding point. The load vs. deflection curve is plotted in Figure 5.9. Figure 5.10 shows the relationship between strand slip and loading force. For Control, Damage and Mortar cases, the girders all failed in shear with wide opening of inclined shear cracks and pull-out of longitudinal strands combined with minor flexural cracks observed under loading point. For the CFRP case, the girder mainly failed in flexure due to strong resistance in shear. Although the strand slip of the Control case was not monitored. In other strand slip cases, it is noted that strand did not show significant slip until the failure point, which indicated that strand slip had minimal effect on the behavior of the girder.

Table 5.3. Test Results

Specimen	Peak Load, kN (kips)	% of Control Peak Load	% of Control Initial Stiffness	% of Control Secant Stiffness at Yielding	% of Control Ductility	Strand Slip at Peak Load, mm (in.)	Max. FRP Strain, mm/mm (in./in.)
Control	543.1 (122.1)	100.0	100.0	100.0	100.0	--	--
Damage	536.4 (120.6)	98.8	85.6	77.8	60.7	0.34 (0.013)	--
Mortar	496.4 (111.6)	91.4	84.7	80.0	46.5	0.40 (0.016)	--
CFRP	557.3 (125.3)	102.6	97.7	81.2	109.6	0.01 (0.000)	0.0011

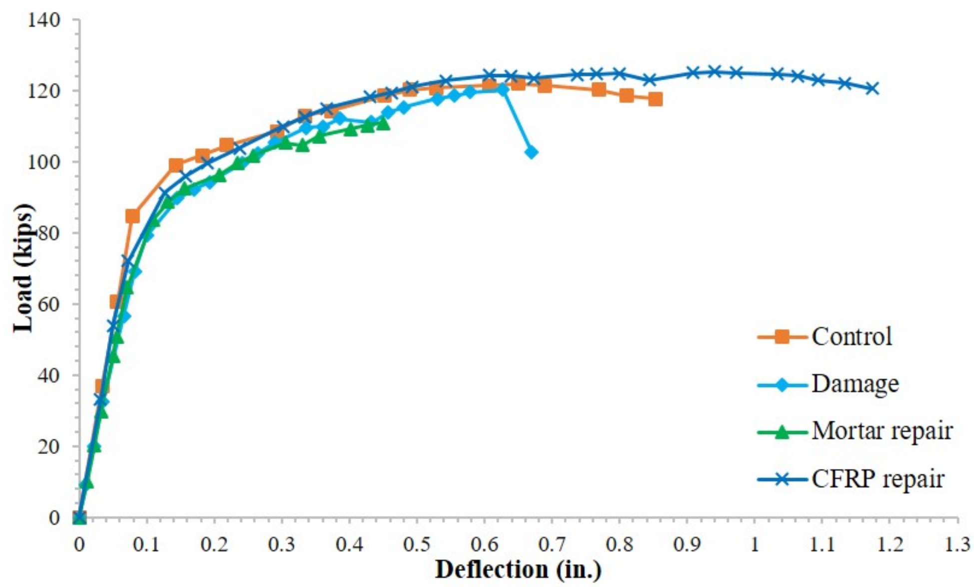

Figure 5.9. Load vs. deflection curves.

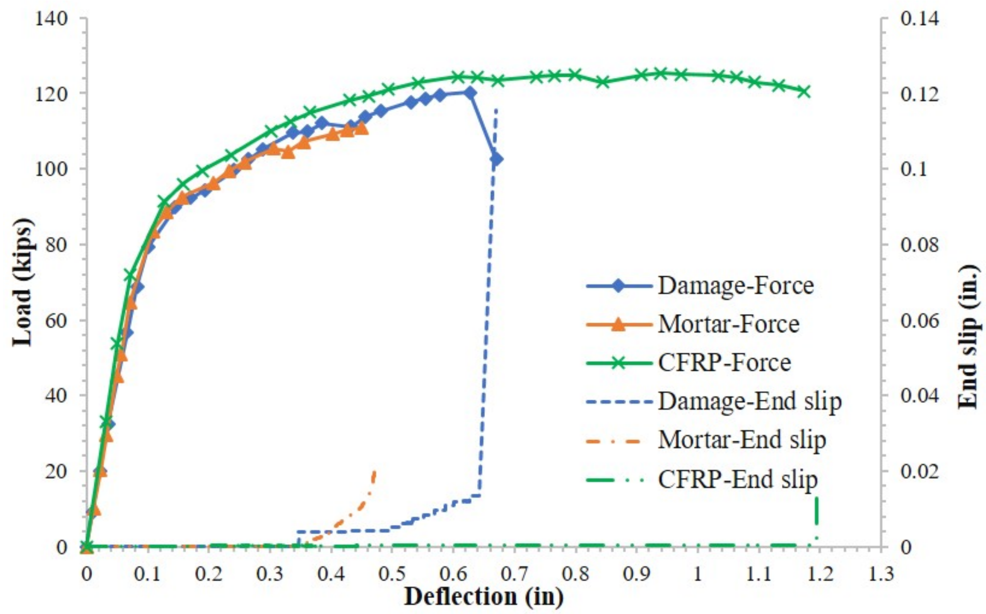

Figure 5.10. Load, end-slip vs. deflection curves.

5.4 DISCUSSION

5.4.1 Effect of Cover Damage and Mortar Repair

As shown in Figure 5.9, the removal of the concrete cover resulted in decreases of 14.4% and 22.2% in both initial stiffness and secant stiffness, as compared to the control case. However, the peak force only showed 1.2% reduction. This is mainly because the failure mode of Control and Damage was identical, which was the pull-out of the longitudinal strand. From Figure 5.11, it is observed that the bonded length starting from the girder end to the pull-out location of the strand was very close for both cases. Similar bonded length would yield similar pull-out force. As a result, the total force required to generate such pull-out force was also similar, which explained why the peak force of Control and Damage were close to each other. Moreover, the remaining base concrete could still undertake high stress within compression diagonal strut without showing any crushing of concrete. This is due to high concrete compressive strength, regardless of whether or not the concrete cover is present. Therefore, more inclined shear cracks were observed in Damage than in Control. The removal of the concrete cover showed more detrimental effect on stiffness and ductility than on peak load. The ductility of the damaged girder was reduced by 39.3% as compared to Control.

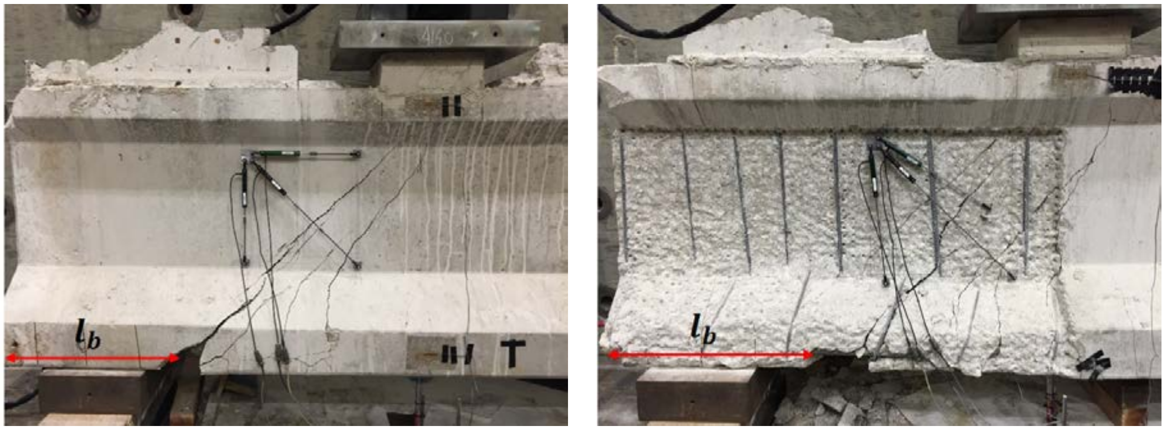

(a) Control case after failure (b) Damage case after failure

Figure 5.11. Failure mode of Control and Damage specimens.

From the load vs. deflection curves, it can be seen the Mortar repair case nearly coincided with the Damage case. Compared to Control case, the Mortar case showed a reduction of 8.6%, 15.3% and 20.0% in peak load, initial stiffness and secant stiffness at yielding point. The ductility of Mortar case was even worse than the Damage case with 53.5% reduction compared to the Control case. Based on the test results, it seemed that the mortar repair alone failed to restore the shear capacity and ductility of the girder. There are several reasons that might have caused such unexpected behavior. First, the bond between mortar mix and base concrete was not strong enough to allow stress transferred to mortar. Therefore, unlike the Control and Damage cases where more inclined shear cracks developed during loading, the Mortar repair case only showed one main shear crack as shown in Figure 5.12(a). Second, cracks developed in the mortar above the bearing plate were observed on both sides of the girder as shown in Figure 5.12(b). This is because the mortar surface was not on the same plane with the base concrete. As a result, the vertical reaction was originally resisted by the mortar cover until an even surface was achieved at bearing plate, which caused the cracking above the bearing plate, as shown in Figure 5.13. Such cracks jeopardized the integrity of the mortar cover and limited its participation in resisting shear stress. To prevent such cracks from developing, it is recommended that mortar repair should be terminated slightly above the bearing plate to prevent any contact with bearing plate. Unlike small-scale beams where mortar repair would recover partial shear capacity, mortar repair in full-scale girders showed negative effect and proved to be too insufficient to recover the shear capacity and ductility of the girder.

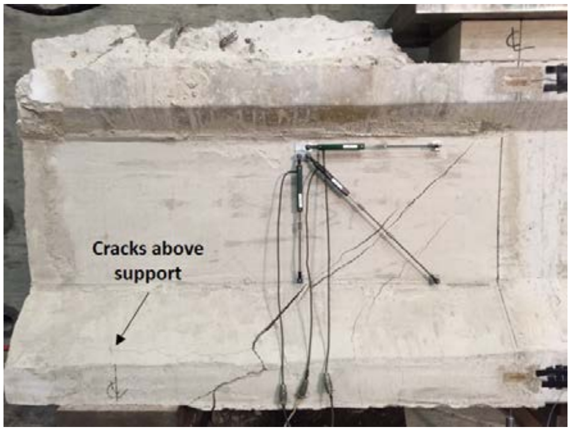

(a) Mortar after failure

(b) Cracks above bearing plate

Figure 5.12. Failure mode of Mortar specimen.

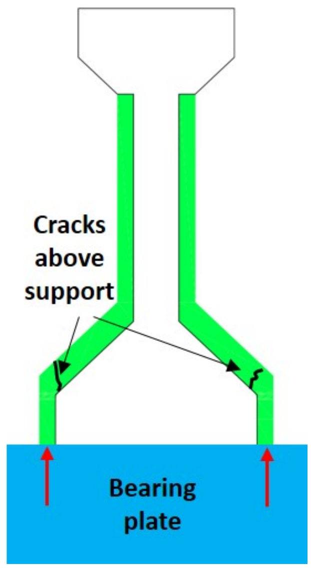

Figure 5.13. Cracks caused by uneven force transfer.

5.4.2 Discussion on the Effect of CFRP Laminate Repair

From Figure 5.9, it is observed that the overall behavior of the damaged girder was improved with CFRP laminate repair. Both peak load and ductility exceeded the Control case with an increase of 2.6% and 9.6%, respectively. Even though a small difference (2.3%) existed, the CFRP laminate repair was able to recover most of initial stiffness. This is mainly because the FRP laminate facilitated the mortar to get engaged in the shear behavior during early loading stage, which was not possible with the absence of FRP laminate in Mortar repair case. Overall debonding of FRP panel was not observed during the test with only partial debonding concentrated around the second and third panel (see Figure 5.14(a)). Longitudinal strip serving as anchorage system provided sufficient anchoring between vertical FRP panel and mortar cover and only showed debonding at its ends when the girder failed, as shown in Figure 5.14(b).

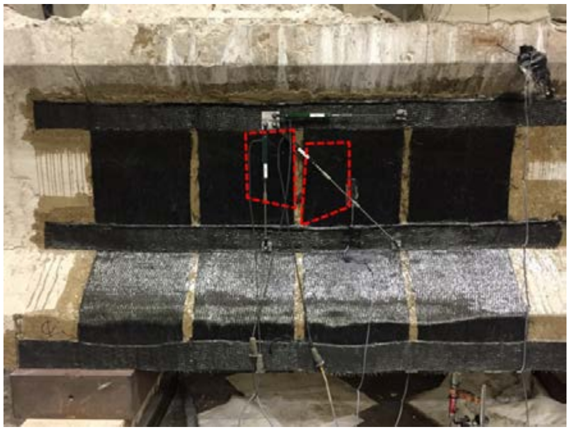

(a) Partial debonding of FRP laminate (b) Total debonding of longitudinal strip at ends

Figure 5.14. Debonding of CFRP laminates.

The failure mode of the CFRP case differed from the other cases by showing major flexural cracks under the loading point as shown in Figure 5.15(a). Significant shear crack was not observed on either side of the girder. This indicates that the CFPR laminate repair had strengthened the damaged end and enhanced its shear capacity of the girder because the failure mode was shifted from shear failure to flexural failure.

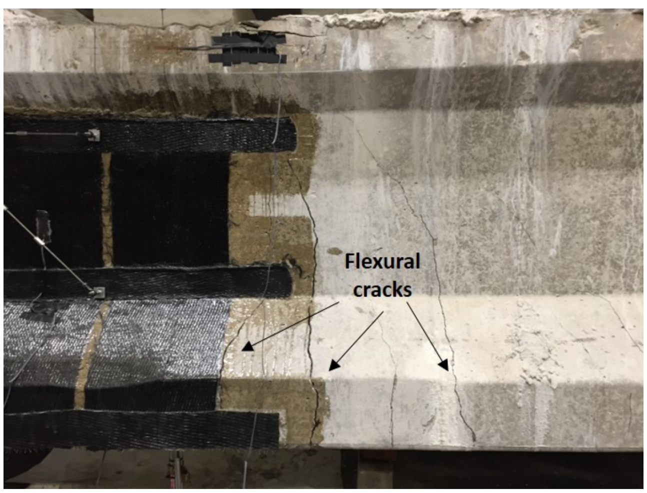

(a) Flexural cracks under loading point (b) Large cracking above bearing plate

Figure 5.15. Failure mode of CFRP case.

Figure 5.15(b) shows a large crack developed on the left side of the girder above bearing plate, which was caused by the same mechanism illustrated in Figure 5.13. However, based on load vs. deflection curve, the initial stiffness was mostly recovered as well as the ductility of the girder. This indicates that due to the adhesion between FRP laminate and mortar, the cracked mortar cover was held together and the integrity of the girder was ensured.

Based on the test results of full-scale girders, the mortar repair alone proved to be too ineffective to restore the capacity of the girder. The use of 2-sided wet layup CFRP laminates showed effectiveness in improving the peak load, stiffness, and ductility of the girder with damaged end region. Based on the positive repair results, applying FRP laminate repair to a short shear span has showed its potential and practical usage in field application.

CHAPTER 6: FINITE ELEMENT MODELING AND PARAMETRIC ANALYSIS

This chapter numerically investigates the use of FRP composite materials as a means of repairing and retrofitting the damaged ends of PC bridge girders using finite element (FE) modeling. First, a 3D FE model was created for the experimental shear pull off testing previously performed on unaged and aged CFRP externally bonded laminate specimens. The bond-slip behavior was calibrated to the experimental data. This model was then utilized in a 3D FE analysis of a full-scale PC bridge girder to study the effectiveness of various types of externally bonded CFRP laminate shear repairs at the damaged end regions of PC bridge girders. In addition to modeling the CFRP laminate repairs, we investigated the effect on strength and stiffness of the girder due to end region damage. Because of accelerated aging we implemented reductions in stiffness and bond strength into the repaired PC bridge girder model. Our goal was to investigate the effectiveness of CFRP laminate shear repairs at the end region after long-term environmental exposure.

6.1 BOND-SLIP FINITE ELEMENT MODELING

The results of some of the shear pull-out tests presented in Chapter 3 were used to model the bond-slip behavior of unaged and aged CFRP laminates. Figure 6.1 summarizes the results of the 101.6 mm (4 in.), 152.4 mm (6 in.), and 203.2 mm (8 in.) bond lengths of CFRP that were modeled. All FE modeling in this chapter was performed using the software program ABAQUS/CAE 6.13 (Dassault Systèmes 2013). Each model of the pull-out tests discussed in Chapter 3 was comprised of three geometrical components: a concrete prism, an FRP laminate, and a thin cohesive interface layer between the concrete and the FRP laminate.

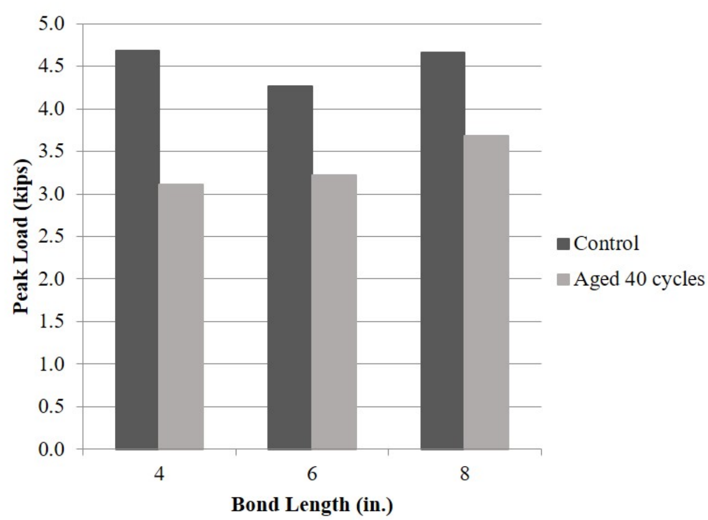

Figure 6.1. Peak loads for CFRP laminate specimens modeled.

6.1.1 Concrete Block

The 89 mm x 89 mm x 305 mm (3.5 in. x 3.5 in. x 12 in.) concrete prism was modeled using C3D8 8-node linear brick elements. The eight nodes defining each brick element are each associated with three translational degrees of freedom. The concrete material model consisted of an isotropic linear elastic ascending branch, followed by plastic behavior defined through the concrete damaged plasticity model parameters. The concrete modulus of elasticity E_c was calculated as $4.73\sqrt{f'_c}$ ($57\sqrt{f'_c}$), or 31.7 GPa (4600 ksi). The compressive behavior was based on Todeschini et al. (1964) stress-strain model shown in Equation 6-1. The strain at maximum compressive stress is calculated using Equation 6-2 (MacGregor and Wight 2005), where f'_c is concrete stress (in MPa or ksi) at any given strain ε and ε_0 is strain at maximum compressive strength f'_c (in MPa or ksi). The tensile behavior of concrete is defined by a linear ascending branch up to the modulus of rupture (taken as $0.622\sqrt{f'_c}$ ($0.0075\sqrt{f'_c}$), or 4.17 MPa (0.6 psi)), followed by a descending linear branch. The value for ultimate strain is typically specified as the lowest value that will allow for convergence of the model. The stress-strain curve used in this analysis is shown in Figure 6.2.

$$f_c = \frac{2f'_c(\frac{\varepsilon}{\varepsilon_0})}{1+(\frac{\varepsilon}{\varepsilon_0})^2} \tag{6-1}$$

$$\varepsilon_0 = \frac{1.71f'_c}{E_c} \tag{6-2}$$

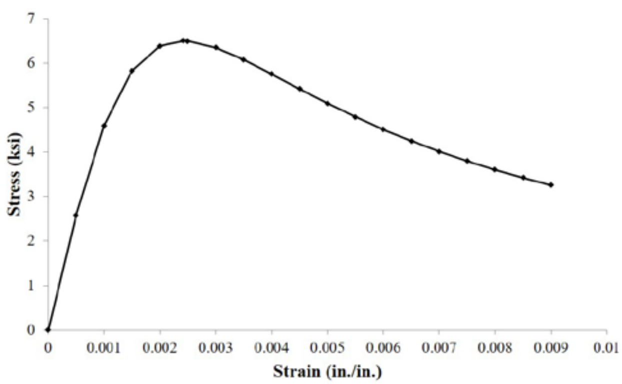

(a) Compressive stress-strain curve

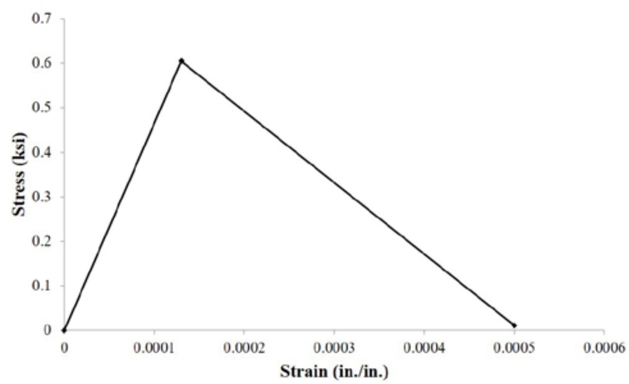

(a) Tensile stress-strain curve

Figure 6.2. Concrete stress-strain behavior used in the analysis.

6.1.2 FRP Laminate

The FRP laminate sheets were modeled using S4 4-node linear shell elements. Orthotropic plane stress linear elastic behavior was used to define the FRP material, which requires parameters E_1, E_2, ν_{12}, G_{12}, G_{13}, and G_{23}. The properties of the unidirectional carbon fiber composite and epoxy matrix were taken from the manufacturer's data (QuakeWrap 2016 a, b). The specified $E_1$and E_2 correspond to the elastic moduli in the longitudinal (parallel to fibers) and transverse (perpendicular to fibers) directions in the laminate. E_1 (elastic modulus of carbon fibers laminated with epoxy resin), was defined as 89.6 GPa (13000 ksi) while E_2 (elastic modulus of the epoxy resin only) was defined as 2.0

GPa (290 ksi). The volume fraction of fibers, V_f, was calculated as 0.383 using Equation 6-3 and the known elastic moduli for the carbon fibers (E_f = 231 GPa (33500 ksi)), epoxy matrix (E_m = 2.0 GPa (290 ksi)), and resulting composite laminate (E = 89.6 GPa (13000 ksi)).

$$E = \left(1 - V_f\right)E_m + V_f E_f \tag{6-3}$$

Using the charts for carbon/epoxy composites in Younes et al. (2012), the values for ν_{12}, G_{12}, G_{13}, and G_{23} were approximated as 0.32, 4.1 GPa (595 ksi), 4.1 GPa (595 ksi), and 2.8 GPa (406 ksi), respectively. The composite layup tool was used to assign and appropriately orient the material properties to the laminate part and specify a thickness of 1.24 mm (0.049 in.).

6.1.3 Cohesive Interface

When modeling FRP composites that are bonded to concrete, it is crucial to include some sort of cohesive interaction or interface between the two substrates. This is needed in order to accurately model the delamination/debonding failure mode that is often prevalent in this application. For this model, a thin layer was placed between the FRP laminate and concrete block, meshed with COH3D8 8-node three-dimensional cohesive elements. The cohesive behavior was modeled through a traction-separation response.

Once the stresses at a node reach the damage initiation criteria, degradation begins. The damage initiation criteria used was the maximum nominal stress criterion, in which damage initiates when any of the maximum stress values assigned are reached. Three maximum stress values were prescribed: normal stress whose direction is perpendicular to the interface, shear stress whose direction is in the longitudinal direction of the shear plane, and shear stress whose direction is in the horizontal direction of the shear plane. The maximum normal stress value was chosen as the modulus of rupture for concrete. This represents the delamination failure mode that is caused by concrete cracking and occurs just below the surface of the concrete substrate. The maximum shear stresses were calibrated based upon the results from the experimental testing. In addition to the damage initiation criteria, uncoupled traction-separation moduli were assigned (E_{nn}, E_{ss}, E_{tt}). The uncoupled traction-separation moduli and cohesive layer thickness were adjusted during the calibration process to achieve a good fit with the experimental data. The damage evolution used in this model is characterized by a linear branch from the point of damage initiation to zero stress at a specified failure displacement, which is another parameter that was adjusted during the calibration process.

6.1.4 Model Assembly

Tie constraints were used to affix either side of the cohesive layer to the concrete block and FRP laminate. A finer mesh was generated on the cohesive layer, as this was the slave surface when applying the tie constraints to the concrete and FRP laminate. The length of the cohesive layer was varied between 101.6 mm (4 in.), 152.4 mm (6 in.), and 203.2 mm (8 in.) to model each of the tested experimental bond lengths. Displacement was applied at top end of the laminate, while end-slip was measured at the opposite end. A fixed boundary condition was applied to the top of the concrete block on the end where displacement was applied. Figure 6.3 shows several of these model assemblies.

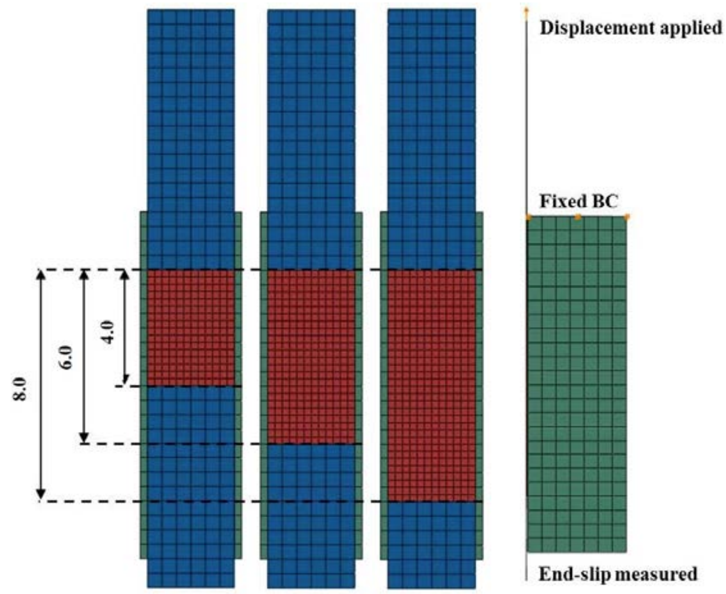

(a) Plan view showing bond length (in.) (b) Side view

Figure 6.3. Shear pull off models with varying bond lengths.

6.1.5 Model Calibration

In order to represent the experimental results, several parameters of the cohesive element layer had to be calibrated. These parameters include the traction-separation moduli (E_{nn}, E_{ss}, E_{tt}), maximum bond shear stresses (τ_1, τ_2), and displacement at failure (δ_u). The calibration process involved several iterations. After each iteration, the force vs. end-slip behavior was plotted and compared to that of the experimental results. The interface stiffness was assumed isotropic, so all three traction-separation moduli were calibrated with a single value E. Likewise, the maximum bond shear stress in either direction was set to the same value τ_{max}. Table 6.1 summarizes these calibrated parameters for the unaged and aged CFRP specimens. Figure 6.4 compares the force-slip curves generated from the model calibration with those obtained experimentally for the unaged and aged specimens for the intermediate bond length.

Table 6.1. Calibrated Cohesive Layer Parameters

Model	Bond length, mm (in.)	τ_{max}, MPa (psi)	τ_{max} reduction	E, MPa (ksi)	E reduction
C1[a]-Unaged	101.6 (4)	3.09 (448)	--	100.0 (14.5)	--
C1-Aged	101.6 (4)	1.93 (280)	37.5%	58.6 (8.5)	51.2%
C2-Unaged	152.4 (6)	2.04 (296)	--	94.5 (13.7)	--
C2-Aged	152.4 (6)	1.43 (207)	29.7%	55.2 (8.0)	41.4%
C3-Unaged	203.2 (8)	1.90 (276)	--	147.3 (21.4)	--
C3-Aged	203.2 (8)	1.35 (196)	29.0%	81.6 (11.8)	41.6%
Avg. Reduction		--	32.1%	--	44.7%

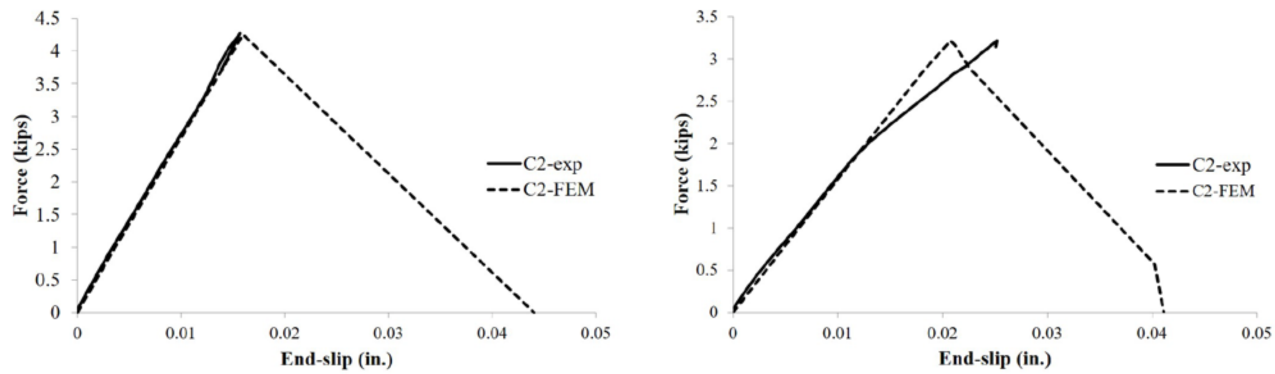

(a) Unaged, 152.4 mm (6 in.) bond length (b) Aged, 152.4 mm (6 in.) bond length

Figure 6.4. Force vs. end-slip of CFRP laminate shear pull off experimental tests and calibrated FEM models.

6.2 PC I-GIRDER FINITE ELEMENT MODEL

6.2.1 Model Description and Calibration

The model of the PC I-girder analyzed in this study was based on experimental tests performed by Andrawes and Pozolo (2011). The I-girder model included several geometrical parts: high strength steel prestressed strands, mild steel bars and stirrups, the concrete girder, and the loading/support plates. To reduce computational demand, half of the I-girder cross-section is modeled with a symmetric boundary condition placed on the inner face of the girder.

6.2.2 Prestressing Strands and Mild Steel

The prestressing strands and mild steel bars and stirrups were modeled using T3D2 2-node linear 3-D truss elements. The prestressing strands have a cross-sectional area of 98.7 mm^2 (0.153 in^2), elastic modulus of 197.9 GPa (28700 ksi) and ultimate strength of 1862 MPa (270 ksi). The nonlinear stress-strain curve is a simplified version of that typically seen with high strength prestressing strands, with yielding occurring at 90% of the ultimate strength, or 1675 MPa (243 ksi). Prestress was applied by imposing a negative predefined temperature field on the strands. Effective prestressing of approximately 1140 MPa (165 ksi) is transferred to the concrete in the first step of the analysis, inducing camber in the girder. Mild steel was modeled as elastic-perfectly plastic with an elastic modulus of 200 GPa (29000 ksi) and a yield strength of 414 MPa (60 ksi). Exact size and location of longitudinal bars and stirrups can be found in Andrawes and Pozolo (2011). All of the mild and prestressing steel was embedded within the concrete girder.

6.2.3 Concrete Girder

The same element type and material models for compressive and tensile behavior that were used in the pull off test, were used for the I-girder. Figure 6.5(a) shows the cross-sectional dimensions of the girder (without the added slab) and the layout of the prestressing strands. Figure 6.5(b) shows a meshed cross-section of the FE model including the strand locations. The girder measures 14.63 m

(48 ft.) in length. The concrete compressive strength $\sqrt{f'_c}$ was specified as 41.8 MPa (6.06 ksi), which is 90% of the $\sqrt{f'_c}$ of I-Girder 2 as tested in Andrawes and Pozolo (2011). The 10% reduction in compressive strength accounts for the difference between cylinder and member strength. The 203 mm x 762 mm (8 in. x 30 in.) slab portion that was cast on top of the I-girder was assumed to have the same compressive strength. To account for the casting of the slab after transfer of prestress, a positive predefined temperature field is applied to the slab portion of the model and the longitudinal rebar contained within the slab portion. This creates compression in the slab, which counteracts the tension produced in the slab by the cambering of the girder in the prestressing step.

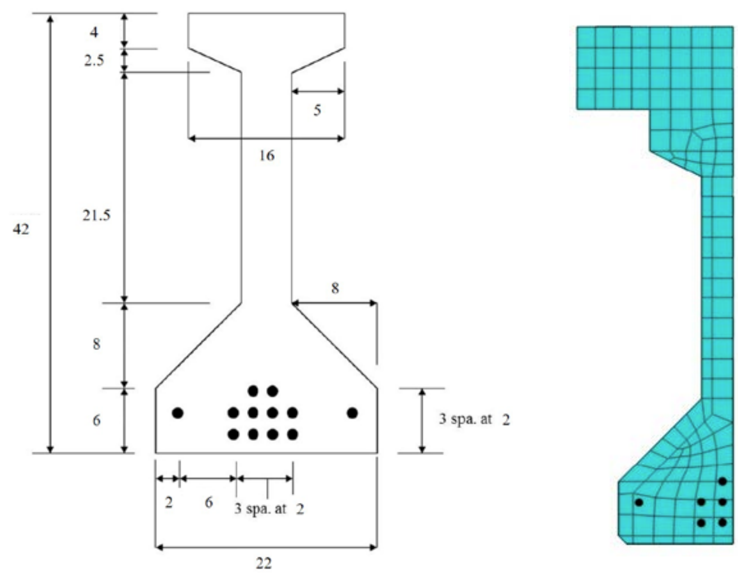

(a) Dimensions (in.) (b) FE mesh

Figure 6.5. Cross-section of I-girder (Andrawes and Pozolo 2011).

6.2.4 Loading and Support Plates

The loading and support plates used the same material model as the mild steel, but with C3D8 8-node linear brick elements. The exact width and depth of the support plates and loading plate used in Andrawes and Pozolo (2011) were used in this model in order to recreate boundary conditions as close as possible to the experimental test. The supports were tied to the concrete surface on one face, and boundary conditions representing either a pin or roller were applied along the center line of the opposite face of the plate. The same concept was applied to the loading plate, but with a downward displacement along the center line of the plate instead of a boundary condition.

6.2.5 Model Calibration

Before performing damage and CFRP repair studies on the I-girder, it was necessary to first calibrate the model to the experimental data. The loading plate and support locations were placed in the three-point loading position of Test 7 in Andrawes and Pozolo (2011), which has a shear span of 1.47 m (4.8 ft.) and a support-to-support distance of 10.84 m (35.6 ft.). Figure 6.6 shows the model test setup. Deflection was measured under the point of loading, and the load-deflection curve obtained from analysis was compared to that from the test (Figure 6.7). While the initial stiffness of the FEM model is slightly greater than the experimental test, the load-deflection behavior correlates reasonably well, overall.

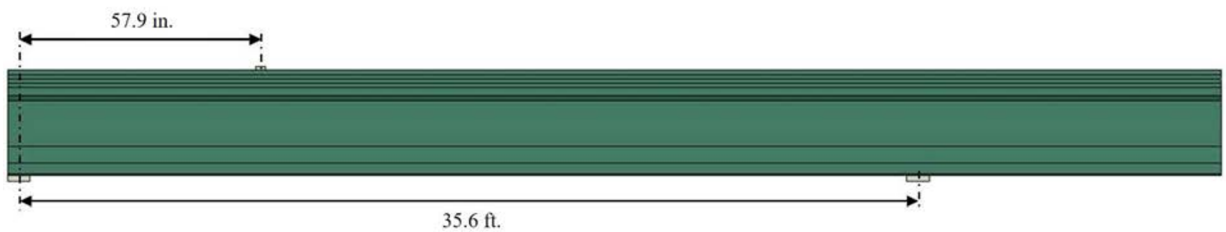

Figure 6.6. Model assembly for three-point bending calibration.

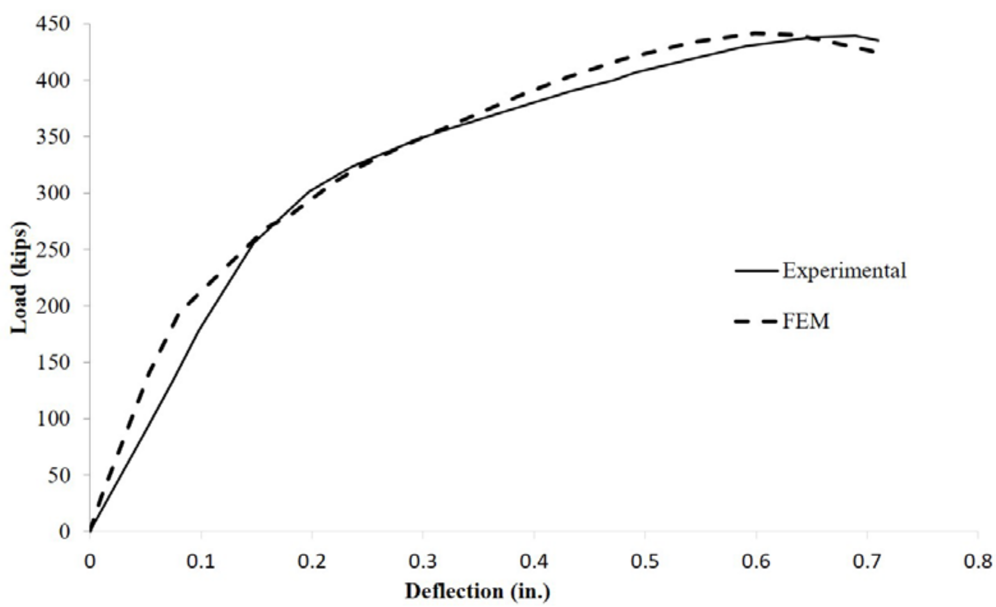

Figure 6.7. Load-deflection plots for model calibration to Andrawes and Pozolo (2011).

6.3 DAMAGE AND MORTAR REPAIR ANALYSIS

After calibrating the I-girder model, the effect of end region damage was investigated. The goal of this part of the study was to apply damage to the model in a way that was representative of the type of end region damage that could be expected in the field. The goal was also to compare the behavior of the damaged beam with that of the control case. In addition to investigating the effect of damage, the recovery effect of a mortar repair on the damaged end region is explored. This is important because mortar repair is a common repair technique used in the field.

Because of the localized nature of the end region damage, shear failure is the primary concern. Since the damage may not progress much more than the beam depth from the end, the behavior of the beam in a short shear span test should be investigated. For this reason, the shear span was chosen as

1.3 of the beam depth, or 1.52 m (5 ft.), for all the I-girder models performed in this section and beyond. The supports were placed at the ends of the girder, to represent the configuration used in the field of a simply supported beam with no cantilever.

The end region damage observed in the field largely affects the cover concrete of the girder. In severe cases, the stirrups may be corroded and the cover concrete can be completely spalled off. Damage progression starting from the end of the girder is taken into account by partitioning the damaged region into three 508 mm (20 in.) wide zones, and prescribing different levels of damage to each zone. In Zone 1 (closest to the end), the compressive strength of cover concrete is reduced to $0.0f'_c$ and the area of the stirrups is reduced to $0.5A_v$, where A_v is the undamaged cross-sectional area of the stirrups. In Zone 2, the compressive strength of cover concrete is reduced to $0.2f'_c$ and the area of the stirrups is reduced to $0.8A_v$. In Zone 3, the compressive strength of cover concrete is reduced to $0.5f'_c$ and the area of the stirrups is left at $1.0A_v$. Figure 6.8 illustrates this progressive damage scheme. Figure 6.9 shows the reduced compressive strength stress-strain curves for the cover concrete.

(a) Cover damage profile

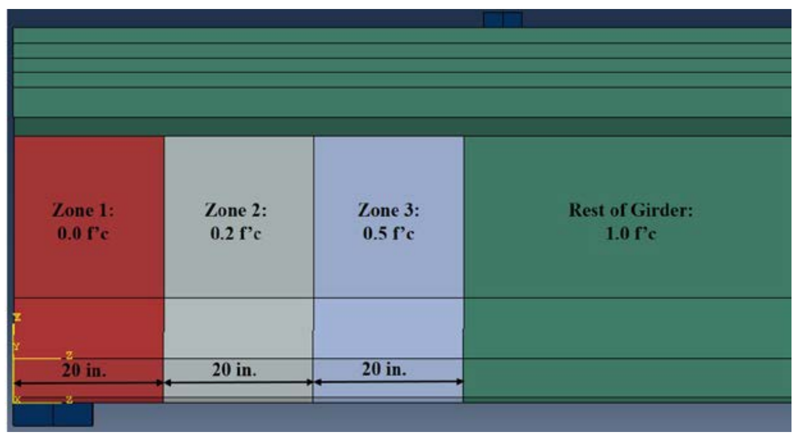

(b) Cover damage zones

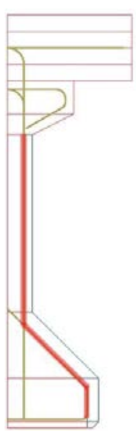

(c) Stirrups damage profile

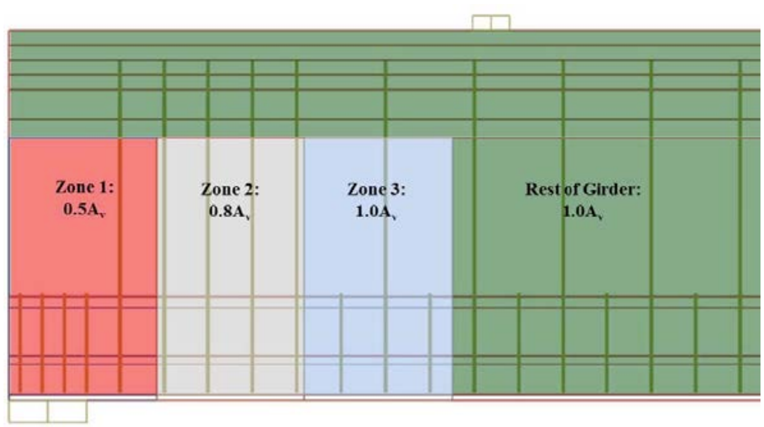

(d) Stirrup damage zones

Figure 6.8. Progressive end region damage scheme.

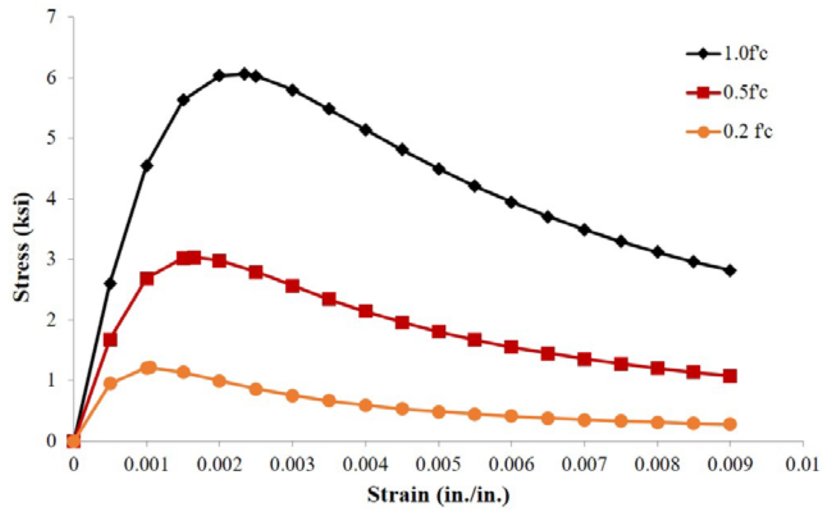

Figure 6.9. Reduced strength cover concrete stress-strain curves.

Next, a model was created to represent a typical mortar repair to the damaged end region of the girder. High strength repair mortars can achieve strengths in excess of 50 MPa (7 ksi), but early set strengths tend to be in the range of 20-30 MPa (3-4.5 ksi). The cold joint between the mortar repair and existing concrete may also limit the ability of the mortar to contribute to the shear strength of the girder. For these reasons, the mortar strength was approximated as 20.9 MPa (3.03 ksi) for the purpose of this study. In this model, the cover concrete strength in Zones 1 and 2 is increased to 20.9 MPa (or $0.5f'_c$) and Zone 3 is left at $0.5f'_c$. The reduced area stirrups in Zones 1 and 2 are left as is to represent a scenario in which mortar is placed over the corroded stirrups without additional steel reinforcement being provided. Figure 6.10 shows the load-deflection plots for the control, damaged, and mortar repaired I-girder models. The damaged case resulted in a 21.5% decrease in strength and 17% loss in stiffness compared to the control case. Secant stiffness values are compared at the onset of nonlinear behavior at a deflection of approximately 4 mm (0.16 in.). The mortar repaired case saw a 15.8% decrease in strength from the control (recovered 5.7%), but stiffness recovery was negligible. This study shows supplementary reinforcement, in addition to a basic mortar repair, is necessary to regain the capacity of the control girder. It is important to note that due to the short shear span-to-depth ratio investigated in this study, failure of the girder occurs due to arch action, not conventional beam action shear failure.

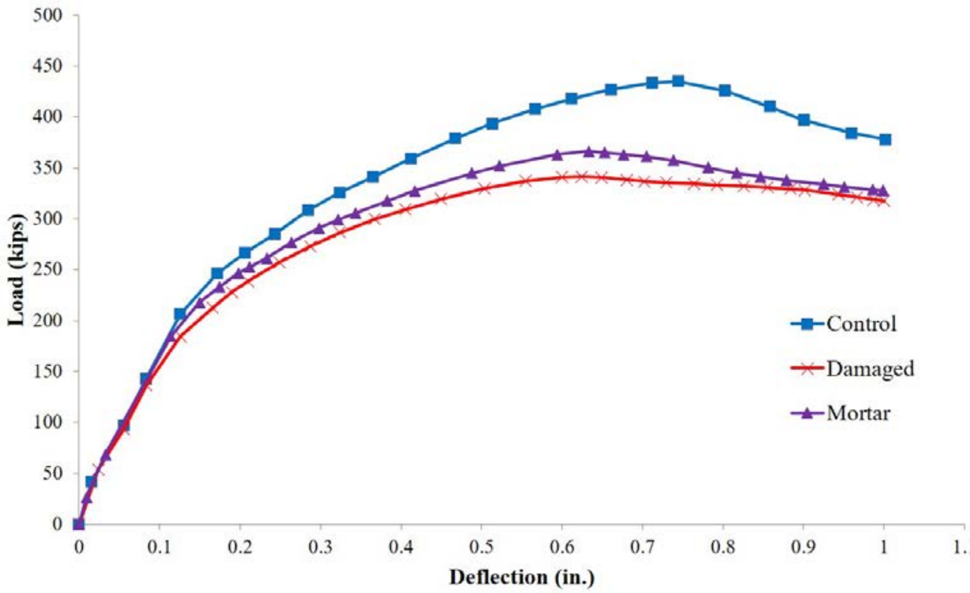

Figure 6.10. Load-deflection plots for control, damaged, and mortar repaired girder.

6.4 CFRP LAMINATE REPAIR ANALYSIS: PARAMETRIC STUDY

After concluding a mortar repair alone is insufficient to regain the original strength and stiffness of the I-girder, CFRP laminate repair studies were conducted. First, an appropriate cohesive bond stress-slip model was chosen from the literature. Lu et al. (2005) proposed three bond stress-slip models based on a database of existing pull tests. These models, particularly the bilinear model, have been used in many FE models to model the debonding failure at the FRP/concrete interface. One drawback to this model is the difficulty in interpreting a geometrical constant that relates the width of the FRP laminate to the width of the concrete prism to which it is attached. For FRP shear reinforcement applications, this value cannot be easily determined. Sato and Vecchio (2003) proposed a similar bilinear model that solely depends on the concrete strength and assumes failure within the thin layer of concrete below the FRP/concrete interface. This model has been validated in FE modeling of FRP shear reinforced PC girders by both You et al. (2011) and Qapo et al. (2014). Therefore, this model was chosen to model the FRP/concrete interface. Equations 6-6 through 6-9 define the bilinear bond-slip curve used in this study, where τ_{max} is the maximum bond stress, S_0 is the slip at τ_{max}, S_u is the ultimate slip, and G_f is the fracture energy.

$$\tau_{max} = (54f_c')^{0.19}\ (MPa)\ (\tau_{max} = (0.0147f_c')^{0.19}\ (ksi)) \tag{6-6}$$

$$S_0 = 0.057\sqrt{G_f}\ (mm)\ (S_0 = 0.0297\sqrt{G_f}\ (in.)) \tag{6-7}$$

$$S_u = \frac{2G_f}{\tau_{max}}\ (mm\ or\ in.) \tag{6-8}$$

$$G_f = (\frac{\tau_{max}}{6.6})^2\ (N/mm)\ (G_f = (\frac{\tau_{max}}{4})^2\ (kip/in)) \tag{6-9}$$

The f'_c was chosen as 20.9 MPa (3.03 ksi), the assumed strength of the cover concrete after mortar repair. To incorporate the effect of accelerated aging, the average reductions in the maximum bond stress and stiffness of the interface from Table 6.1 are applied to the Sato and Vecchio model to generate an aged bond stress-slip curve. The unaged and aged bond stress-slip models used in this study are shown in Figure 6.11.

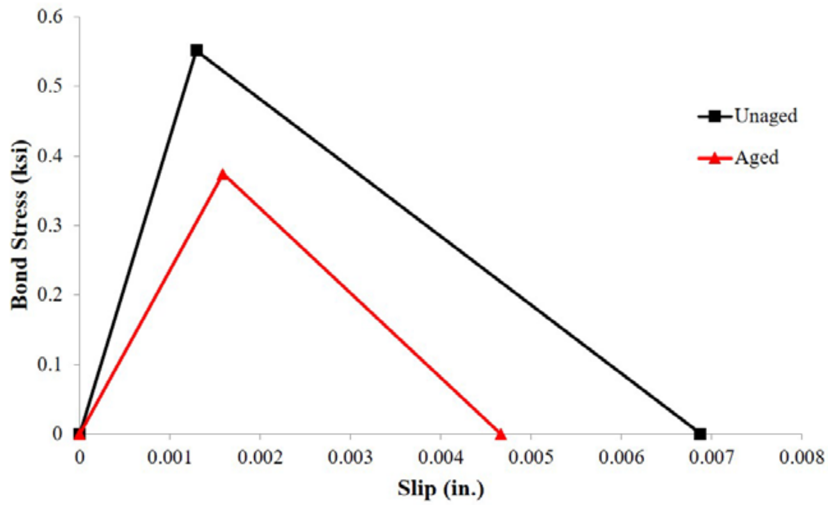

Figure 6.11. Bond stress-slip model used for FRP/concrete interface.

The goal of this portion of the study was to determine if CFRP laminates could be effective in restoring the original capacity of the girder when tested at a low shear span-to-depth ratio (1.3). Then investigate different web anchoring schemes using longitudinal CFRP laminates to determine the most efficient and effective use of material for this application. All the models run in these parametric series are summarized in Table 6.2.

Table 6.2. Test Matrix for All Parametric Series

Model	# of Plies	Width of CFRP Laminate, mm (in.)	Long. CFRP Web Anchors	Peak Load, kN (kips)	% of Control
P1-1	1	508 (20)	--	1702.2 (382.7)	87.9%
P1-2	1	1016 (40)	--	1813.6 (407.7)	93.7%
P1-3	1	1524 (60)	--	1983.7 (446.0)	102.5%
P1-F	1	1721 (67.8)	--	1978.5 (444.8)	102.2%
P1-3-wa	1	1524 (60)	Yes	2043.5 (459.4)	105.6%
P2-F	2	1721 (67.8)	--	2011.2 (452.1)	103.9%
P1-F-Aged	1	1721 (67.8)	--	1945.9 (437.5)	100.5%

The first four models in the parametric series (P1-1, P1-2, P1-3, and P1-F) used one 1.24 mm (0.049 in.) thick ply of unidirectional CFRP oriented vertically as shear reinforcement with no web anchorage and with varying extent of coverage from the end of the beam. The purpose of this series is to determine how much of the damaged end region is necessary to be repaired with CFRP. Figure 6.12

shows the various CFRP layouts of this series. The load-deflection plots for this series are shown in Figure 6.13.

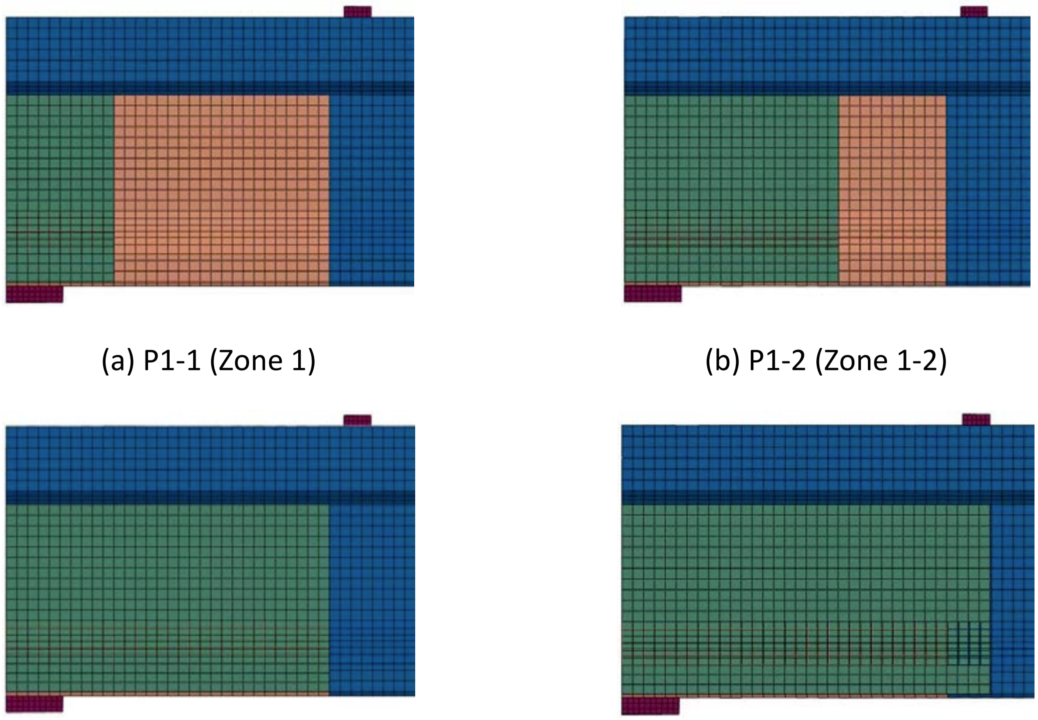

(a) P1-1 (Zone 1)

(b) P1-2 (Zone 1-2)

(c) P1-3 (Zone 1-3)

(d) P1-F (Full span, support to loading plate)

Figure 6.12. Extent of CFRP shear reinforcement in P1-1 through P1-F models.

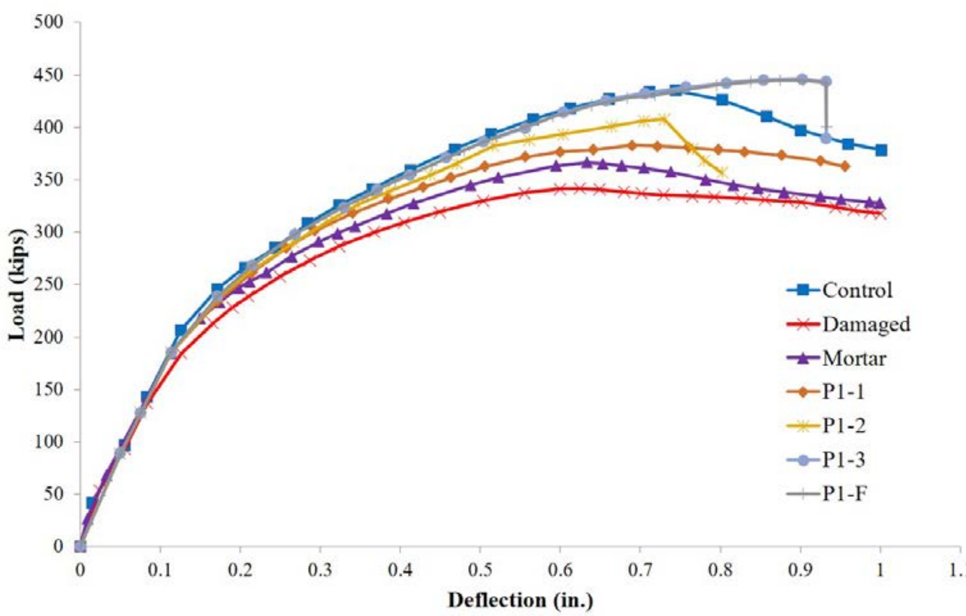

Figure 6.13. Effect of FRP reinforcement on load-deflection response of P1-1 through P1-F models.

There were interesting test results in the control case before debonding of the CFRP occurred. It was found that P1-3 and P1-F were able to recover the stiffness of the control girder and achieved peak loads of 102.5% and 102.2%, respectively. Figure 6.14 shows the stress contours of the cohesive interface at the moment of debonding for P1-1, P1-2, and P1-3. The onset of debonding in P1-1 and P1-2 occurs on the right side of the CFRP sheet due to tensile cracking in the web coinciding with the termination point of the laminate. For the laminates that extend further, debonding initiates near the top of the laminate, where tensile cracking in the web meets the top flange of the girder. For all cases, there is also a stress concentration located at the web/bottom flange junction on the left side of the laminate. This stress concentration, as well as the debonding at the top of the laminate, is addressed in the next study with the introduction of longitudinal CFRP web anchors.

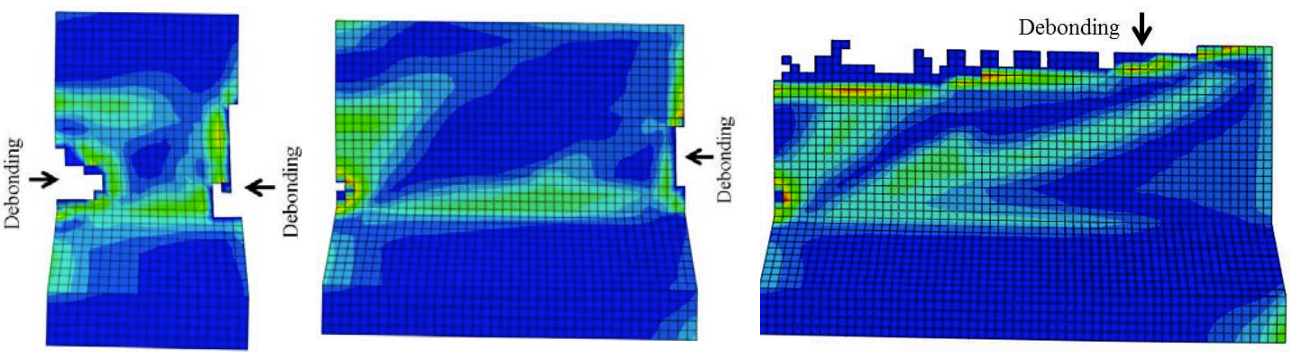

(a) P1-1 (b) P1-2 (c) P1-3

Figure 6.14. Cohesive interface debonding (region of debonding onset indicated).

Next, the effect of using longitudinal web anchors at the top and bottom of the web was studied in the P1-3-wa model in an attempt to delay debonding and improve the effectiveness of the shear CFRP laminates. In this model, 76 mm (3 in.) wide longitudinal CFRP anchors are placed at the top and bottom of the web. In order to develop the CFRP anchors, some bonded area to the concrete is needed. These anchors have a 152 mm (6 in.) extension past the shear CFRP panel on the right side, but at the end of the beam a 51 mm (2 in.) bond length was prescribed, which should allow for development of the anchor at the beam end with only a minor loss of shear CFRP coverage at the very end of the beam. The amount of shear CFRP used in this model is equal to that used in P1-3. The anchors are tied to the shear CFRP where they overlap and are connected to the concrete through a cohesive layer where they extend past the shear CFRP. Figure 6.15(a) shows this configuration. The load-deflection plot for this model is shown in Figure 6.16.

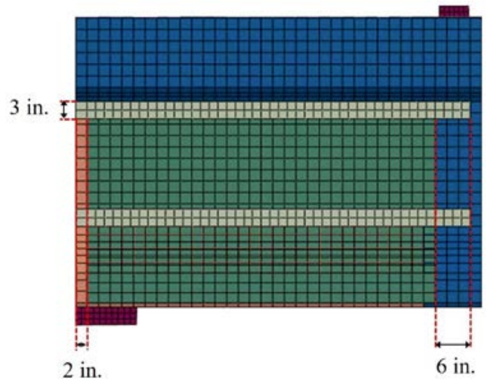

(a) Web anchor layout

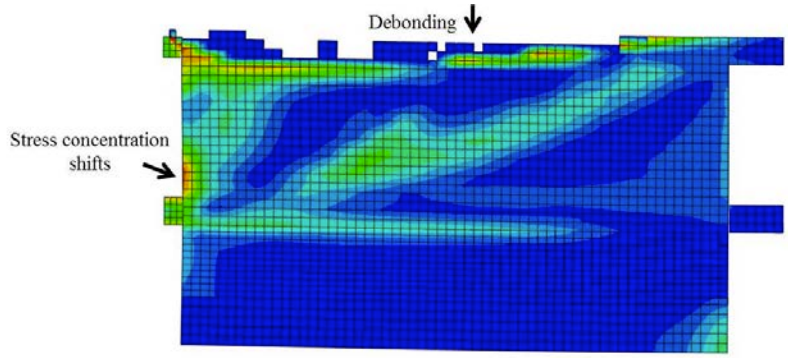

(b) Cohesive interface debonding (P1-3-wa)

Figure 6.15. Web anchor effect.

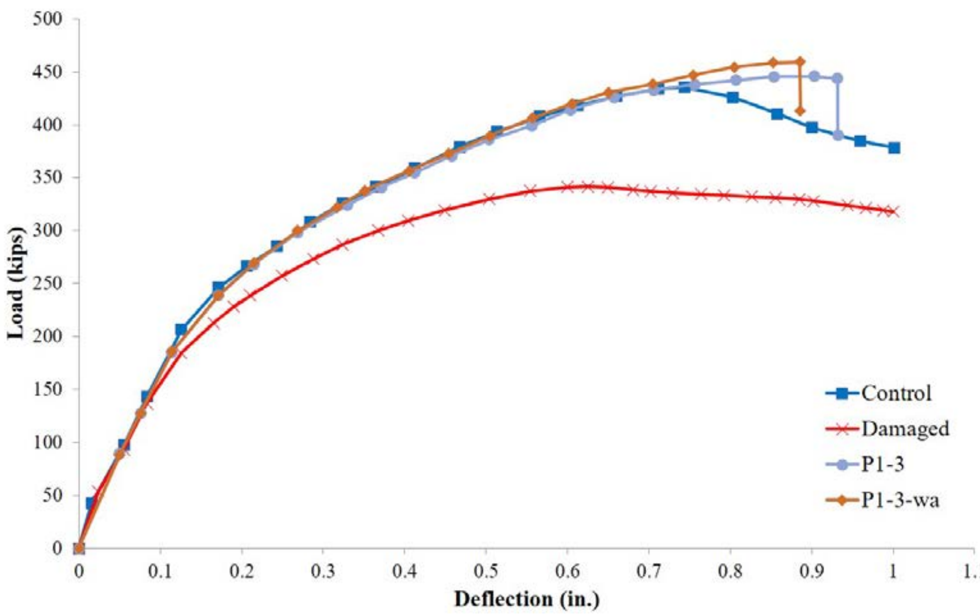

Figure 6.16. Effect of adding web anchorage on load-deflection response.

The addition of longitudinal web anchors proved beneficial in increasing the peak load to 105.6%, which is an increase of 3.1% over P1-3 in the control case. The stiffness did not change significantly with the addition of anchors, although debonding did occur at a slightly lower deflection than P1-3 (22.5 mm (0.89 in.) vs 23.7 mm (0.93 in.)). The debonding failure mode is similar to that of P1-3 in that it starts at the top of the shear CFRP near the middle of the shear span and proceeds towards the end of the beam (Figure 6.15(b)). However, the bottom web anchor does somewhat relieve the stress concentration in the shear CFRP at the web/bottom flange junction near the end of the beam.

Finally, the effects of increasing the FRP thickness by using 2 plies of shear CFRP as well as the effect of accelerated aging were studied. Model P2-F is identical to P1-F except that the CFRP laminate thickness is increased to 2.48 mm (0.098 in.) to represent 2 plies. The aged bond stress-slip model was applied to the model P1-F-Aged, which is otherwise identical to P1-F. The load-deflection plots from these models are shown in Figure 6.17.

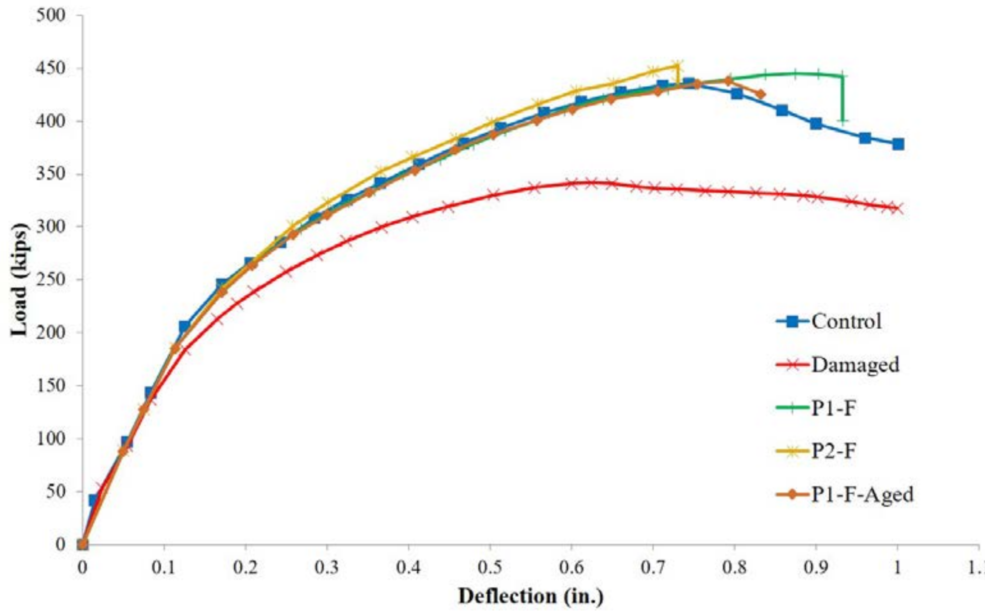

Figure 6.17. Effects of FRP thickness and aging on load-deflection response.

The addition of an extra ply of CFRP slightly increased the stiffness and peak load of the girder, but with a significant decrease in ductility. This concept is noted in the ACI 440 (2008) design equations for FRP contribution to shear strength, where additional bonded face plies decrease the active bond length, which in turn decreases the effective strain of the FRP at debonding. P1-F-Aged followed the load-deflection curve of P1-F, but debonding initiated at a lower load/deflection. This model was still able to reach 100.5% of the peak load of the control girder (only 1.6% less than the unaged case) without suffering a loss in member stiffness. This shows that despite the significant reduction in stiffness of the bond stress-slip model for the aged FRP/concrete interface, the global stiffness of the girder was unaffected.

CHAPTER 7: PROPOSED DESIGN METHODOLOGY

The final task of this project is to propose a design methodology for repairing and retrofitting end damage girders with short shear spans. The proposed design methodology is discussed in the following sections along with two numerical examples. The layout of FRP laminate repair system is illustrated in Figure 7.1.

7.1 PROPOSED DESIGN STEPS

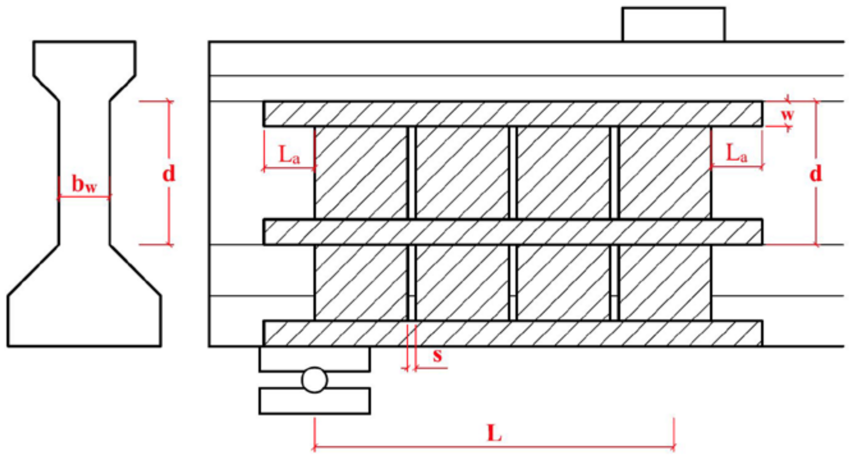

Figure 7.1. Proposed layout of FRP laminate repair system.

Step 1: Estimate the total loss of shear capacity, ΔF using any method or by using Equation 7-1, which assumes that the loss of shear capacity is mainly due to the cracking of concrete in the web.

$$\Delta \boldsymbol{F} = \boldsymbol{f_r} \times \boldsymbol{l} \times \boldsymbol{c} \tag{7-1}$$

Where f_r is the modulus of rupture of concrete, c is the thickness of the damaged concrete, and l is the longitudinal projection of initial shear crack. The initial shear crack appears mainly in the web, and for simplicity, is assumed to be at an angle of approximately $45°$ with respect to longitudinal axis of the beam as shown in Figure 7.2.

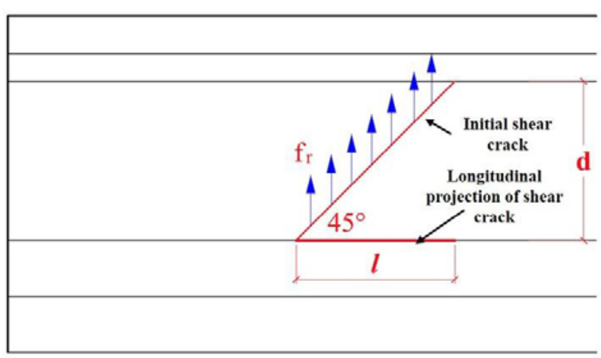

Figure 7.2. Tensile force loss.

Step 2: Determine the average longitudinal tensile strain in the web, $\boldsymbol{\varepsilon_x}$ (see Figure 7.3) using Equation 7-2. It is noted that Equation 7-2 is used for the case where the shear reinforcement satisfies the minimum requirement of shear reinforcement specified in AASHTO (2017).

Table B5.2-1 from AASHTO-LRFD (2017) is used to perform iterations to obtain $\boldsymbol{\theta}$ and $\boldsymbol{\beta}$ that are used in Equation 7-2.

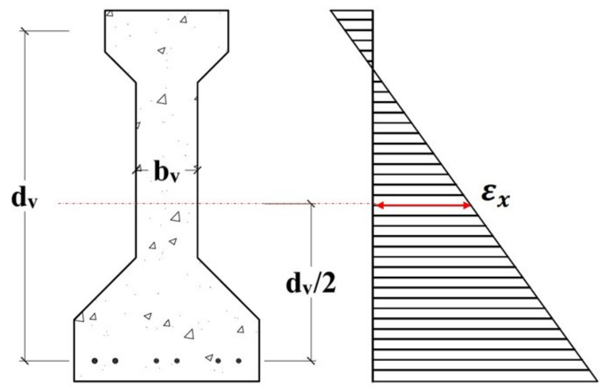

Figure 7.3. Average tensile strain in the web.

$$\boldsymbol{\varepsilon_x = \frac{\frac{|M_u|}{d_v} + 0.5N_u + 0.5|V_u - V_p|cot\theta - A_{ps}f_{p0}}{2(E_sA_s + E_pA_{ps})}} \tag{7-2}$$

Where $\boldsymbol{\theta}$ is an angle between diagonal compressive stress and longitudinal axis of the beam as shown in Figure 7.4; $\boldsymbol{\beta}$ is a factor relating to the effect of longitudinal strain on the shear capacity of concrete. $\boldsymbol{M_u}$ is factored moment and is not taken less than $\boldsymbol{V_u d_v}$; $\boldsymbol{V_u}$ is factored shear force; $\boldsymbol{N_u}$ is factored axial force; $\boldsymbol{V_p}$ is component in the direction of the applied shear of the effective prestressing force; $\boldsymbol{d_v}$ is effective shear depth. $\boldsymbol{A_s}$ and $\boldsymbol{A_{ps}}$ are the area of non-prestressing tensile reinforcement and area of prestressing steel, respectively; $\boldsymbol{E_s}$ and $\boldsymbol{E_p}$ are the Young's modulus of non-prestressing tensile reinforcement and prestressing steel, respectively. $\boldsymbol{f_{p0}}$ is a parameter taken as modulus of elasticity of prestressing tendons multiplied by the locked-in difference in strain between the prestressing tendons and surrounding concrete, for the usual levels of prestressing, a value of 0.7$\boldsymbol{f_{pu}}$ is appropriate (AASHTO 2017).

Step 3: Plug $\boldsymbol{\varepsilon_x}$, $\boldsymbol{\theta}$ into the Equation 7-3 to compute principal tensile strain ($\boldsymbol{\varepsilon_1}$).

$$\boldsymbol{\varepsilon_1 = \varepsilon_x + [\varepsilon_x + 0.002(1 - \sqrt{1 - \frac{v_u}{f'_c}\frac{0.8+170\varepsilon_1}{sin\theta cos\theta}})]cot^2\theta} \tag{7-3}$$

Where $\boldsymbol{v_u}$ is average factored shear stress in the concrete.

Step 4: Obtain vertical component ($\boldsymbol{\varepsilon_y}$) of $\boldsymbol{\varepsilon_1}$ by multiplying $\boldsymbol{\varepsilon_1}$ by $\boldsymbol{cos\theta}$. The directions of $\boldsymbol{\varepsilon_1}$ and $\boldsymbol{\varepsilon_y}$ are shown in Figure 7.4. The FRP design strain ($\boldsymbol{\varepsilon_{FRP}}$) is computed by dividing $\boldsymbol{\varepsilon_y}$ by a factor $\boldsymbol{\mu}$ (see Equation 7-4). The factor, $\boldsymbol{\mu}$ is defined as the ratio between the vertical component of ultimate strain calculated using Equations 7-2 and 7-3 and the strain of FRP laminate at peak force. Based on the small-scale and full-scale beam tests, the value of $\boldsymbol{\mu}$ was found to be on average equal to 6.0. If the computed $\boldsymbol{\varepsilon_{FRP}}$ is found to be greater than 0.004, a value of 0.004 should be used to design FRP laminate.

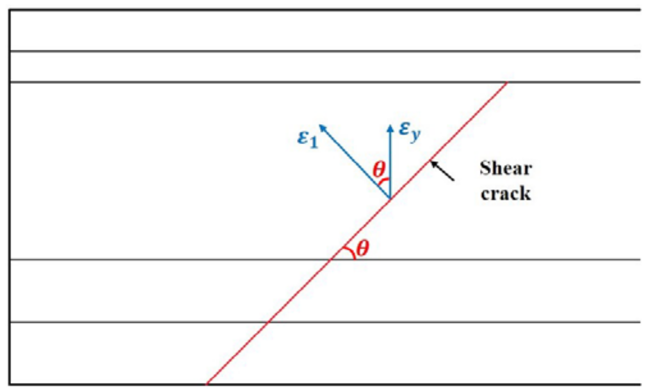

Figure 7.4. Direction of ε_1 and ε_y.

$$\boldsymbol{\varepsilon_{FRP}} = \frac{\varepsilon_y}{\mu} = \frac{\varepsilon_1 \times cos\theta}{\mu} \tag{7-4}$$

Step 5: Choose the material type of FRP system and calculate the amount of FRP material (thickness of FRP layer, *t*) needed using Equation 7-5.

$$\boldsymbol{t} = \frac{\Delta F}{E_{FRP} \times L \times \varepsilon_{FRP}} \tag{7-5}$$

Where $\boldsymbol{E_{FRP}}$ is the Young's modulus of the selected FRP material, $\boldsymbol{L}$ is the length of shear span as shown in Figure 7.1.

Step 6: Determine the width of longitudinal strip ($\boldsymbol{w}$), spacing ($\boldsymbol{s}$) between panels and anchor length ($\boldsymbol{L_a}$) (see Figure 7.1).

It is recommended to place 3 longitudinal strips: at the top of the web, the bottom of the girder, and the joint between web and bottom flange. Based on the testing of full-scale girders, the width of the strips is recommended to be at least 3 in. The spacing ($\boldsymbol{s}$) between FRP panels is suggested to be at least 1.0 in. to ensure sufficient bond between anchor strip and concrete. For girders with sufficient space around end region, longitudinal strip could be looped around the end of the girder similar to the case in the testing of small-scale beam in Chapter 4. For girders with inadequate space around end region, the longitudinal strips could be terminated at girder end with sufficient anchorage length using the same layout of full-scale girder testing in Chapter 5. For both cases, the anchorage length ($\boldsymbol{L_a}$) needs to be equal or greater than 6 in. It is important to note that detailing values ($\boldsymbol{w}$, $\boldsymbol{s}$ and $\boldsymbol{L_a}$) recommended herein are primarily based on the limited tests that were carried out during this study. More tests are recommended to further optimize these values.

7.2 DESIGN EXAMPLE USING SMALL-SCALE BEAMS

The small-scale beam test conducted in Chapter 4 is used as a design example following the proposed design method. The cover of the small-scale beam is 12.7 mm (0.5 in.) in thickness and the concrete compressive strength is 49.4 MPa (7.16 ksi). The length of shear span $\boldsymbol{L}$ equals to 508 mm (20 in.) and the height ($\boldsymbol{d}$) and thickness ($\boldsymbol{b_w}$) of the web is 190 mm (7.5 in.) and 76.2 mm (3 in.) respectively. The area of prestressing strands ($\boldsymbol{A_{ps}}$) is 296.1 mm^2 (0.459 in^2). The area of mild steel bars ($\boldsymbol{A_s}$) is 189.7 mm^2 (0.294 in^2). The effective shear depth ($\boldsymbol{d_v}$) is calculated as 377 mm (14.83 in.). Factor $\boldsymbol{f_{p0}}$ is taken as 0.7$\boldsymbol{f_{pu}}$ which is 1303 MPa (189 ksi). The Young's moduli of mild steel and prestressing strand are 200 GPa (29000 ksi) and 196 GPa (28700 ksi), respectively. The FRP design process is shown below:

Step 1: calculate the tensile force loss ($\Delta\boldsymbol{F}$)

$$\Delta F = f_r \times l \times c = \frac{7.5\sqrt{7160}}{1000} \times 7.5 \times 0.5 = 2.4\ kips$$

Step 2: compute average longitudinal tensile strain ($\boldsymbol{\varepsilon_x}$) in the web

$\boldsymbol{M_u}$ and $\boldsymbol{V_u}$ of the small-scale beams are calculated as 205.9 kN-m (151.8 kip-ft) and 94.3 kN (21.2 kips). Through iterations using AASHTO Table B5.2-1, $\boldsymbol{\theta}$ and $\boldsymbol{\beta}$ are 36.4 and 2.23, respectively. Since there is no axial load or draped strand, $\boldsymbol{N_u}$ and $\boldsymbol{V_p}$ are zero.

$$\varepsilon_x = \frac{\frac{|M_u|}{d_v} + 0.5|V_u|cot\theta - A_{ps}f_{p0}}{2\left(E_sA_s + E_pA_{ps}\right)} = \frac{\frac{151.8 \times 12}{14.83} + 0.5 \times 21.2 \times cot36.4^\circ - 0.459 \times 189}{2(29000 \times 0.294 + 28700 \times 0.459)} = 0.001164$$

Step 3: plug $\boldsymbol{\varepsilon_x}$ into Equation 7-3 and solve for principal tensile strain ($\boldsymbol{\varepsilon_1}$), $\boldsymbol{\varepsilon_1 = 0.003740}$.

Step 4: obtain FRP design strain ($\boldsymbol{\varepsilon_{FRP}}$)

$$\varepsilon_{FRP} = \frac{\varepsilon_y}{\mu} = \frac{0.003740 \times cos36.4^\circ}{6.0} = 0.00050$$

Step 5: choose FRP material and compute the number of FRP layers

CFRP laminate is selected as repair material. From Table 4.2, the Young's modulus $\boldsymbol{E_{CFRP}}$ is 86.9 GPa (13000 ksi) and the thickness of each CFRP layer is 1.24 mm (0.049 in.).

$$t_{CFRP} = \frac{\Delta F}{E_{CFRP} \times L \times \varepsilon_{FRP}} = \frac{2.4}{13000 \times 20 \times 0.00050} = 0.019\ in.$$

Hence, one layer of CFRP laminate is selected.

7.3 DESIGN EXAMPLE USING FULL-SCALE GIRDERS

Full-scale girder tested in Chapter 5 is used as another design example following the proposed design method. The cover of the full-scale beam is 31.75 mm (1.25 in.) in thickness and the concrete compressive strength is 60.3 MPa (8.75 ksi). The length of shear span $\boldsymbol{L}$ equals to 1079 mm (42.5 in.) and the height ($\boldsymbol{d}$) and thickness ($\boldsymbol{b_w}$) of the web is 431.8 mm (17 in.) and 152.4 mm (6 in.) respectively. The area of prestressing strands ($\boldsymbol{A_{ps}}$) is 592.3 mm^2 (0.918 in^2). The effective shear depth ($\boldsymbol{d_v}$) is calculated as 830 mm (32.7 in.). Factor $\boldsymbol{f_{p0}}$ could be taken as 0.7$\boldsymbol{f_{pu}}$ which is 1303 MPa (189 ksi). The Young's moduli of mild steel and prestressing strand are 200 GPa (29000 ksi) and 186 GPa (27000 ksi), respectively. The FRP design process is shown below:

Step 1: calculate the tensile force loss ($\boldsymbol{F}$)

$$\Delta F = f_r \times l \times c = \frac{7.5\sqrt{8750}}{1000} \times 17 \times 1.25 = 14.9\ kips$$

Step 2: compute average tensile strain ($\boldsymbol{\varepsilon_x}$) in the web

$\boldsymbol{M_u}$ and $\boldsymbol{V_u}$ of the full-scale beams are calculated as 797.4 kN-m (587.8 kip-ft) and 378.1 kN (85.0 kips). Through iterations using AASHTO Table B5.2-1, $\boldsymbol{\theta}$ and $\boldsymbol{\beta}$ are 36.4 and 2.23. Since there is no axial load or draped strand, $\boldsymbol{N_u}$ and $\boldsymbol{V_p}$ are zero.

$$\varepsilon_x = \frac{\frac{|M_u|}{d_v} + 0.5|V_u|cot\theta - A_{ps}f_{p0}}{2(E_sA_s + E_pA_{ps})} = \frac{\frac{587.8 \times 12}{32.7} + 0.5 \times 85.0 \times cot36.4° - 0.918 \times 189}{2(27000 \times 0.918)}$$
$$= 0.002015$$

Step 3: plug $\boldsymbol{\varepsilon_x}$ into Equation 7-3 and solve for principal tensile strain ($\boldsymbol{\varepsilon_1}$), $\boldsymbol{\varepsilon_1 = 0.00614}$.

Step 4: obtain FRP design strain ($\boldsymbol{\varepsilon_{FRP}}$)

$$\varepsilon_{FRP} = \frac{\varepsilon_y}{\mu} = \frac{\varepsilon_1 \times cos\theta}{\mu} = \frac{0.00614 \times cos36.4°}{6.0} = 0.00082$$

Step 5: choose FRP material and compute the number of FRP layers

CFRP laminate is selected as repair materials. From Table 4.2, the Young's modulus $\boldsymbol{E_{CFRP}}$ is 86.9 GPa (13000 ksi) and the thickness of each CFRP layer is 1.24 mm (0.049 in.).

$$t_{CFRP} = \frac{\Delta F}{E_{CFRP} \times L \times \varepsilon_{FRP}} = \frac{14.9}{13000 \times 42.5 \times 0.00082} = 0.033\ in.$$

Hence, one layer of CFRP laminate is selected.

CHAPTER 8: SUMMARY, CONCLUSIONS AND RECOMMENDATIONS

8.1 ACCELERATED AGING AND PULL-OUT TESTS

The primary goal of this research was to determine if externally bonded FRP sheets or NSM FRP bars could be effectively used as long-term repair solutions for damaged end regions of PC bridge girders. First, direct shear pull-out tests were performed on GFRP and CFRP laminate and NSM bar concrete specimens. Some of these specimens were subjected to an accelerated aging protocol consisting of freeze/thaw cycling in the presence of a deicing salt solution. The purpose of these tests was to determine what effect, if any, the aging process had on the bond-slip behavior and capacity of the FRP/concrete interface. From these tests, the following conclusions were drawn:

- The NSM bar method offers more efficient usage of FRP material than externally bonded FRP laminates with regards to the percentage of ultimate strength of the FRP materials that can be achieved and average bond stress. This is due to the fact that the capacity of a FRP laminate interface is determined by its effective bond length, regardless of the bonded length of the interface. On the other hand, the NSM bars can achieve strengths as high as the tensile strength of the FRP itself if the bonded length is sufficient.
- For externally bonded FRP laminates, GFRP performed better on average than CFRP after undergoing freeze/thaw cycling in the presence of a deicing salt solution, both in terms of decrease in pull-out force and stiffness of the FRP/concrete interface.
- For externally bonded GFRP laminates, degradation of the FRP/concrete interface occurred mainly in the first 40 cycles of aging.
- GFRP NSM bars saw a negligible decline in performance after accelerated aging for the bond lengths investigated. Failure mode was either FRP bar rupture or failure at the epoxy/bar interface at stress levels close to the rupture strength of the bar and was not affected by aging.
- Some CFRP NSM bar specimens saw a shift in failure mode from the epoxy/bar interface to the epoxy/concrete interface after accelerated aging. Epoxy/concrete interface failure was caused by concrete cracking along the bonded length, which was induced by the scaling damage incurred at the concrete surface. Specimens that shifted failure mode saw a large decrease in pull-out force, while specimens that retained the epoxy/bar failure mode did not see a decrease in pull-out force.
- From these limited tests, the NSM technique for repair and retrofit of concrete structures with FRP appears to be superior to externally bonded laminates in terms of material efficiency and resistance to environmental effects.

8.2 FLEXURAL TESTS OF SMALL-SCALE BEAMS

Three-point bending tests were performed on small-scale PC beams to examine the effect of using mortar-only and mortar in conjunction with various FRP repairs in restoring the shear capacity of damaged end regions of these beams. Concrete cover damage was imposed at the beam ends to simulate deterioration caused by long-term environmental exposure. A quick setting mortar repair was applied to the damaged region to investigate the effectiveness of a typical field mortar repair. Externally bonded GFRP and CFRP laminate systems and a CFRP NSM bar system were used in conjunction with the mortar repair as additional shear reinforcement in an effort to regain the shear capacity of the undamaged beam. From these tests, the following conclusions were drawn:

- A mortar repair alone is not sufficient enough to regain the strength and stiffness of a girder with diminished shear capacity due to loss of cover concrete in the web. The cold joint between the existing concrete and mortar limits the engagement of the mortar repair in shear and provides a weak interface along which shear cracks will propagate.
- Externally bonded FRP shear reinforcement can be used to regain and even exceed the shear capacity of the undamaged girder, even when using a low shear span-to-depth ratio for testing.
- Longitudinal FRP anchors placed over the FRP shear laminates can be effective in preventing complete delamination of the shear laminates and increasing the effective FRP strain at delamination. For AASHTO I-girders, these anchors can specifically prevent debonding at the interface between the web and the bottom flange.
- The CFRP laminate repair method was able to exceed the strength and stiffness of the control beam. GFRP laminates were able to regain the strength of the control beam, but showed no stiffness recovery.
- The FRP NSM bar repair method is not suitable for situations requiring an extensive mortar repair. The interface between the mortar repair and the base concrete inhibits the transfer of stress to the FRP bars located within the mortar repair.

8.3 FLEXURAL TESTS OF FULL-SCALE GIRDERS

Three-point bending tests were performed on full-scale prestressed girders using the same procedure adopted in small-scale beam testing. The only difference was that severe end region damage was simulated by removing the concrete cover to the centerline of the stirrups from web all the way through the bottom flange. Afterwards a quick set mortar was applied to damaged region to restore the shape of the girder, followed by CFRP laminate application. The purpose of conducting three-point bending test on full-scale girders was to validate whether the repair technique that was effective in repairing small beams could also be applied effectively for full-scale girders. The following conclusions were drawn for the tests:

- A mortar repair alone is not sufficient enough to recover the shear strength and ductility of the girder with damaged end. Weak bond surface between mortar and base concrete and cracks developed above bearing plates diminished the repair effect from mortar.
- Longitudinal FRP anchors proved to be effective in preventing the overall debonding of FPR laminates. As long as sufficient bond length was guaranteed on both ends, FRP anchor strips could be terminated at girder end in the cases when space around girder end is limited.
- It is verified that the externally bonded CFRP shear reinforcement repair that is effective in repairing small beams could also be applied effectively for full-scale girders. This could recover or even exceed the shear capacity and ductility of the undamaged girders.

8.4 FINITE ELEMENT AND PARAMETRIC STUDY

Finally, a finite element analysis was utilized in this study to investigate the damaged end regions of PC I-girders and the effectiveness of CFRP laminate shear reinforcement repairs under a low shear span-to-depth ratio. The results of the shear pull-out tests on unaged and aged CFRP laminates were used to predict reduction in bond stress-slip properties of the FRP/concrete interface layer. A Parametric study was performed to determine the most effective use of externally bonded CFRP laminates to restore the capacity of a full-scale PC I-girder with a severely damaged end region. From this analysis, the following conclusions were drawn:

- A conventional mortar repair is not sufficient enough to regain the strength and stiffness of a girder with a severely damaged end region, especially if the stirrups have experienced section loss due to corrosion.
- FRP shear reinforcement should extend past the point of expected cracking in the web in order to prevent premature debonding failure of the FRP in middle of the web. If FRP is extended far enough, debonding will initiate at the top of the web.
- Longitudinal FRP anchors at the top and bottom of the web can slightly delay debonding and help achieve higher shear strengths than with FRP shear reinforcement alone.
- In the case of a low shear span-to-depth ratio, the addition of more plies of FRP may not be an economical or effective use of material. It can severely reduce the ductility of the FRP/concrete joint for relatively minor gains in strength and stiffness of the member.
- Even after a 32.1% reduction in the peak bond stress and a 44.7% reduction in stiffness of the FRP/concrete interface due to environmental aging, externally bonded CFRP laminates could regain the original stiffness and load capacity of the PC I-girder with a severely damaged end region.

8.5 RECOMMENDATIONS

Based on the results of this study, the following recommendations are made for future application of FRP as repair method for PC girders with damaged end regions:

- The application of FRP laminates in general is effective in performing repairs for PC girders with damaged end regions. The method presented in Chapter 7 is recommended for the design of the FRP laminates.
- At girders' end regions where the application of U-shape FRP laminates is not feasible, it is recommended to apply the FRP laminates on the sides of the girder in addition to using anchorage system to prevent early debonding of the laminates. The anchorage system should be applied at a minimum to the top and bottom ends of the laminates as well as at the bottom of the girder's web.
- In the case of minor damage repairs when small amount of FRP layers is needed, both CFRP and GFRP laminates could achieve effective repair in regaining the strength of the damaged girders. However, for more severe damage conditions, CFRP is recommended as it will require laminates with smaller thickness, which is proven to be more effective when using longitudinal anchorage strips.

- The selection of anchorage system mainly depends on the thickness of FRP laminates. In the case of small FRP laminate thickness (e.g. 1 or 2 layers), an anchorage system of longitudinal FRP strips could be used. If more layers of FRP laminates are used, the use of longitudinal strips might not be as sufficient. If this happens, mechanical anchorage system (e.g. fasteners) is recommended instead.
- At girder ends, the longitudinal strips could be either wrapped around the end when sufficient space is available or terminated at the end when space is limited.
- The use of mortar/grout only as a repair measure is insufficient and does not restore the strength and/or stiffness of the damaged girder.
- To achieve the desired effectiveness of the FRP repair, the applied FRP laminates should cover the entire damaged region, not just a portion of it.
- If mortar/grout is used to restore the shape of the girder prior to applying the FRP, it is recommended to terminate the mortar at least ¼ inch above the bearing plate to avoid early cracking of the mortar.

REFERENCES

AASHTO (2017), Guide Specification for Design of Bonded FRP Systems for Repair and Strengthening of Concrete Bridge Elements, American Association of State Highway and Transportation Officials; Washington, D.C., USA.

ACI 440 (2008), ACI 440.2R-08: Guide for the Design and Construction of Externally Bonded FRP Systems for Strengthening Concrete Structures, American Concrete Institute; Farmington Hills, MI, USA.

Alkhrdaji, T. (2015), 'Strengthening of Concrete Structures Using FRP Composites", STRUCTURE magazine, June.

Al-Mahmoud, F., Castel, A., Minh, T.Q. and François, R. (2015), "Reinforced Concrete Beams Strengthened with NSM CFRP Rods in Shear", *Advances in Structural Engineering*, **18**(10), 1563-1574.

Al-Mahmoud, F., Mechling, J. and Shaban, M. (2014), "Bond Strength of Different Strengthening Systems – Concrete Elements Under Freeze-Thaw Cycles and Salt Water Immersion Exposure", *Construction and Building Materials*, **70**, 399-409.

Andrawes, B. and Pozolo, A. (2011), "Transfer and Development Lengths in Prestressed Self-Consolidating Concrete Bridge Box and I-Girders", Research Report No. ICT- 11-092; University of Illinois at Urbana-Champaign, Urbana, IL, USA.

ARTBA. (2016). American Road and Transportation Builders Association. Retrieved November 27, 2017 from: http://www.artba.org/economics/2016-u-s-deficient-bridges/

Ary, M.I. and Kang, T.H.K. (2012), "Shear-Strengthening of Reinforced & Prestressed Concrete Beams Using FRP: Part I – Review of Previous Research", *International Journal of Concrete Structures and Materials*, **6**(1), 41-47.

ASTM C666/C666M-15 (2015), Standard Test Method for Resistance of Concrete to Rapid Freezing and Thawing, ASTM International; West Conshohocken, PA, USA.

ASTM C672/C672M-12 (2012), Standard Test Method for Scaling Resistance of Concrete Surfaces Exposed to Deicing Chemicals, ASTM International; West Conshohocken, PA, USA.

ASTM D3039/D3039M-14 (2014), Standard Test Method for Tensile Properties of Polymer Matrix Composite Materials, ASTM International; West Conshohocken, PA, USA.

ASTM D7205/D7205M-06 (2011), Standard Test Method for Tensile Properties of Fiber Reinforced Polymer Matrix Composite Bars, ASTM International; West Conshohocken, PA, USA.

ASTM D7565/D7565M-10 (2010), Standard Test Method for Determining Tensile Properties of Fiber Reinforced Polymer Matrix Composites for Strengthening of Civil Structures, ASTM International; West Conshohocken, PA, USA.

Belarbi, A., Bae, S., Ayoub, A., Kuchma, D., Mirmiran, A. and Okeil, A. (2011), “Design of FRP Systems for Strengthening of Concrete Girders in Shear”, NCHRP Report No. 678; National Cooperative Highway Research Program, Washington, D.C., USA.

Bianco, V., Barros, J.A.O. and Monti, G. (2010), “New Approach for Modeling the Contribution of NSM FRP Strips for Shear Strengthening of RC Beams”, *ASCE Composites for Construction Journal*, **14**(1), 36–48.

Bianco, V., Monti, G. and Barros, J.A.O. (2014), “Design Formula to Evaluate the NSM FRP Strips Shear Strength Contribution to a RC Beam”, *Composites: Part B*, **56**, 960-971.

Bousselham, A. and Chaallal, O. (2006), “Effect of Transverse Steel and Shear Span on the Performance of RC Beams Strengthened in Shear with CFRP”, *Composites: Part B*, **37**, 37-46.

Chen, J.F. and Teng, J.G. (2001), “Anchorage Strength Models for FRP and Steel Plates Bonded to Concrete”, *Journal of Structural Engineering*, **127**(7), 784-791.

Chen, J.F. and Teng, J.G. (2003), “Shear Capacity of FRP-Strengthened RC beams: FRP Debonding”, *Construction and Building Materials*, **17**, 27-41.

Coelho, M.R.F., Sena-Cruz, J.M. and Neves, L.A.C. (2015), “A Review on the Bond Behavior of FRP NSM Systems in Concrete”, *Construction and Building Materials*, **93**, 1157-1169.

Colombi, P., Fava, G. and Poggi, C. (2009), “Bond Strength of CFRP-Concrete Elements Under Freeze-Thaw Cycles”, *Composite Structures*, **92**, 973-983.

CSA (2012), S806-12: Design and Construction of Building Structures with Fibre- Reinforced Polymers, Canadian Standard Association, Toronto, ON, Canada.

CTS Cement (2016), Product Data Sheet: Fast-Setting High Strength Mortar, CTS Cement, Inc.; Cypress, CA, USA.

Darby, A., Clarke, J., Shave, J. D. and Ibell, T. (2012), “Design Guidance for Strengthening Concrete Structures Using Fibre Composite Materials”, Technical Report 55; The Concrete Society.

Dassault Systèmes (2013), Abaqus 6.13 Documentation Collection; Dassault Systèmes Simulia Corp., Providence, RI, USA. http://129.97.46.200:2080/v6.13/index.html

Davalos, J.F., Kodkani, S.S., Ray, I. and Lin, C. (2008), “Fracture Evaluation of GFRP Concrete Interfaces for Freeze-Thaw and Wet-Dry Cycling”, *Journal of Composite Materials*, **42**(14), 1439-1466.

De Lorenzis, L. (2004), “Anchorage Length of Near-Surface Mounted Fiber-Reinforced Polymer Rods for Concrete Strengthening —Analytical Modeling”, *ACI Structural Journal*, **101**(3), 375-386.

De Lorenzis, L. and Nanni, A. (2002), “Bond Between Near-Surface Mounted FRP Rods and Concrete in Structural Strengthening”, *ACI Structures Journal*, **99**(2), 123-133.

De Lorenzis, L. and Teng, J.G. (2006) “Near-Surface Mounted FRP Reinforcement: An Emerging Technique for Strengthening Structures”, *Composites: Part B*, **38**, 119- 143.

De Lorenzis, L., Lundgren, K. and Rizzo, A. (2004), “Anchorage Length of Near-Surface Mounted Fiber-Reinforced Polymer Bars for Concrete Strengthening-Experimental Investigation and Numerical Modeling”, *ACI Structural Journal*, **101**(2), 269-278.

De Lorenzis, L., Rizzo, A. and La Tegola, A. (2002) “A Modified Pull-out Test for Bond of Near-Surface Mounted FRP Rods in Concrete”, *Composites: Part B*, **33**, 589- 603.

Dias, S.J.E. and Barros, J.A.O. (2009), “Performance of Reinforced Concrete T Beams Strengthened in Shear with NSM CFRP Laminates”, *Engineering Structures*, **32**, 373-384.

Dias, S.J.E. and Barros, J.A.O. (2012), “NSM Shear Strengthening Technique with CFRP Laminates Applied in High-Strength Concrete Beams with or without Precracking”, *Composites: Part B*, **43**, 290-301.

Dias, S.J.E. and Barros, J.A.O. (2013), “Shear Strengthening of RC Beams with NSM CFRP Laminates: Experimental Research and Analytical Formulation”, *Composite Structures*, **99**, 477-490.

FIB (2001), “Externally Bonded FRP reinforcement for RC Structures”, Bulletin 14; International Federation for Structural Concrete (*fib*).

Garzón-Roca, J., Sena-Cruz, J.M., Fernandes, P. and Xavier, J. (2015), “Effect of Wet-Dry Cycles on the Bond Behaviour of Concrete Elements Strengthened with NSM CFRP Laminate Strips”, *Composite Structures*, **132**, 331-340.

Hilti (2014), 2014 Hilti North American Product Tech Guide, Hilti, Inc.; Tulsa, OK, USA.

Hughes Brothers (2011a), Glass Fiber Reinforced Polymer (GFRP) Rebar – Aslan 100 series, Hughes Brothers, Inc.; Seward, NE, USA.

Hughes Brothers (2011b), Carbon Fiber Reinforced Polymer (CFRP) Rebar – Aslan 200 series, Hughes Brothers, Inc.; Seward, NE, USA.

Hutchinson, R. L., and Rizkalla, S. H. (1999), “Shear Strengthening of AASHTO Bridge Girders Using Carbon Fiber Reinforced Polymer Sheets”, *ACI Special Publications*, **188**, 945–958.

Islam, A.K.M.A. (2008), “Effective Methods of Using CFRP Bars in Shear Strengthening of Concrete Girders”, *Engineering Structures*, **31**, 709-714.

Khalifa, A., Belarbi, A., and Nanni, A. (2000), “Shear Performance of RC Members Strengthened with Externally Bonded FRP Wraps”, *Proceedings*, 12th World Conference on Earthquake Engineering, Auckland, New Zealand.

Lee, D., Cheng, L. and Hui, J.Y. (2013), “Bond Characteristics of Various NSM FRP Reinforcements in Concrete”, *Journal of Composites for Construction*, **17**(1), 117-129.

Lu, X.Z., Teng, J.G., Ye, L.P. and Jiang, J.J. (2005), “Bond-Slip Models for FRP Sheets/Plates Bonded to Concrete”, *Engineering Structures*, **27**, 920-937.

MacGregor, J. and Wight, J. (2005), *Reinforced Concrete: Mechanics and Design*, (4th Edition), Prentice Hall, Upper Saddle River, NJ, USA.

Miller, O.A. (2006), “Repair of Impact-Damaged Prestressed Concrete Bridge Girders Using Carbon Fiber Reinforced Polymer (CFRP) Materials”, Master’s Thesis, Department of Civil Engineering, North Carolina State University, Raleigh, NC.

Nanni, A. (2004), “Strengthening of an Impact-Damaged PC Girder”, Concrete Repair Bulletin, May/June.

Nanni, A., Di Ludovico, M. and Parretti, R. (2003), “Shear Strengthening of a PC Bridge Girder with NSM CFRP Rectangular Bars”, *Advances in Structural Engineering*, **7**(4), 97-109.

Novidis, D.G. and Pantazopoulou, S.J. (2008), “Bond Tests of Short NSM-FRP and Steel Bar Anchorages”, *Journal of Composites for Construction*, **12**(3), 323-333.

Mojarrad, P. (2015), “Composites in Structural Rehabilitation - Advances and Experiences”, *Composites Australia and CRC-ACS Conference*, Gold Coast, Australia, April.

Ouezdou, M.B., Bae, S. and Belarbi, A. (2008), “Effective Bond Length of Externally Bonded FRP Sheets”, *Fourth International Conference on FRP Composites in Civil Engineering*, Zurich, Switzerland, July.

Pellegrino, C. and Sena-Cruz, J. (2015), “Design Procedures for the Use of Composites in Strengthening of Reinforced Concrete Structures”, STAR 234-DUC; RILEM, Paris, France.

Qapo, M., Dirar, S., Yang, J. and Elshafie, M.Z.E.B. (2014), “Nonlinear Finite Element Modelling and Parametric Study of CFRP Shear-Strengthened Prestressed Concrete Girders”, *Construction and Building Materials*, **76**, 245-255.

QuakeWrap (2016a), Product Data Sheet: QuakeBond J300SR Saturating Resin, QuakeWrap, Inc.; Tucson, AZ, USA.

QuakeWrap (2016b), Product Data Sheet: QuakeWrap TU27C Carbon Fabric for Structural Strengthening, QuakeWrap, Inc.; Tucson, AZ, USA.

QuakeWrap (2016c), Product Data Sheet: QuakeWrap VU27G Glass Fabric for Structural Strengthening, QuakeWrap Inc.; Tucson, AZ, USA.

Ramseyer, C. and Kang, T.H.K. (2012), "Post-Damage Repair of Prestressed Concrete Girders", *International Journal of Concrete Structures and Materials*, **6**(3), 199-207.

Rizzo, A. and De Lorenzis, L. (2007), "Behavior and Capacity of RC beams Strengthened in Shear with NSM FRP Reinforcement", *Construction and Building Materials*, **23**, 1555-1567.

Sato, Y. and Vecchio, F.J. (2003), "Tension Stiffening and Crack Formation in Reinforced Concrete Members with Fiber-Reinforced Polymer Sheets", *Journal of Structural Engineering*, **129**(6), 717-724.

Schuman, P. M. (2004), "Mechanical Anchorage for Shear Rehabilitation of Reinforced Concrete Structures with FRP: An Appropriate Design Approach", Ph.D. Thesis, Department of Structural Engineering, University of California, UCSD, San Diego, CA.

Silva, M.A.G., Cidade, M.T., Biscaia, H. and Marreiros, R. (2014), "Composites and FRP Strengthened Beams Subjected to Dry/Wet and Salt Fog Cycles", *Journal of Materials in Civil Engineering*, **26**(12), 1-12.

Soliman, S.M., El-Salakawy, E. and Benmokrane, B. (2011), "Bond Performance of Near- Surface-Mounted FRP Bars", *Journal of Composites for Construction*, **15**(1), 103-111.

Subramaniam, K.V., Ali-Ahmad, M. and Ghosn, M. (2008), "Freeze-Thaw Degradation of FRP-Concrete Interface: Impact on Cohesive Fracture Response", *Engineering Fracture Mechanics*, **75**, 3924-3940.

Todeschini, C.E., Bianchini, A.C. and Kesler, C.E. (1964), "Behavior of Concrete Columns Reinforced with High Strength Steels", *Journal of the American Concrete Institute*, **61**(6), 701-716.

Yao, J., Teng, J.G. and Chen, J.F. (2004), "Experimental Study on FRP-to-Concrete Bonded Joints", *Composite: Part B*, **36**, 99-113.

You, Y., Ayoub, A. and Belarbi, A. (2011), "Three-dimensional Nonlinear Finite-Element Analysis of Prestressed Concrete Beams Strengthened with FRP Composites", *Journal of Composites for Construction*, **15**(6), 896-907.

Younes, R., Hallal, A., Fardoun, F. and Chehade, F.H. (2012), "Comparative Review Study on Elastic Properties Modeling for Unidirectional Composite Materials", InTech, Rijeka, Croatia.

Zureick, A.H., Ellingwood, B.R., Nowak, A.S., Mertz, D.R. and Triantafillou, T.C. (2010), " Recommended Guide Specification for the Design of Externally Bonded FRP Systems for Repair and Strengthening of Concrete Bridge Elements", NCHRP Report No. 655; National Cooperative Highway Research Program, Washington, D.C., USA.

APPENDIX A: FRP NSM BAR SPECIMEN FAILURE PATTERNS

This appendix contains figures of the post-failure surfaces of all GFRP and CFRP NSM bar specimens.

(a) G-b-4-A0

(b) G-b-6-A0

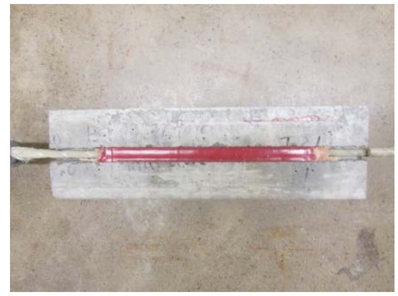

(c) G-b-8-A0

(d) G-b-4-A40

(e) G-b-6-A40

(f) G-b-8-A40

(g) G-b-4-A100

(h) G-b-6-A100

(i) G-b-8-A100

Figure A.1. GFRP NSM bar failure surfaces.


(a) C-b-4-A0

(b) C-b-6-A0

(c) C-b-8-A0


(d) C-b-4-A40

(e) C-b-6-A40
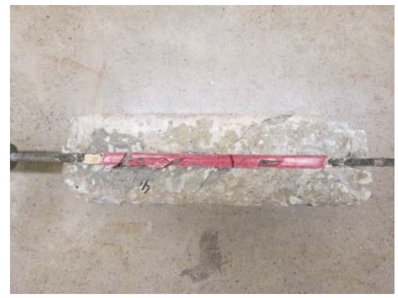
(f) C-b-8-A40


(g) C-b-4-A100

(h) C-b-6-A100

(i) C-b-8-A100

Figure A.2. CFRP NSM bar failure surfaces.

APPENDIX B: DETAILS OF SMALL-SCALE BEAMS

This appendix contains figures of the cross-sectional dimensions of the small-scale beam and details of steel reinforcement.

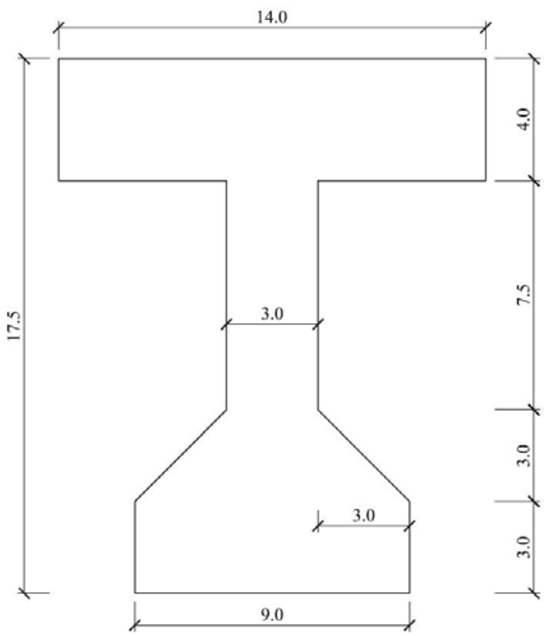

(a) Beam dimensions (in.)

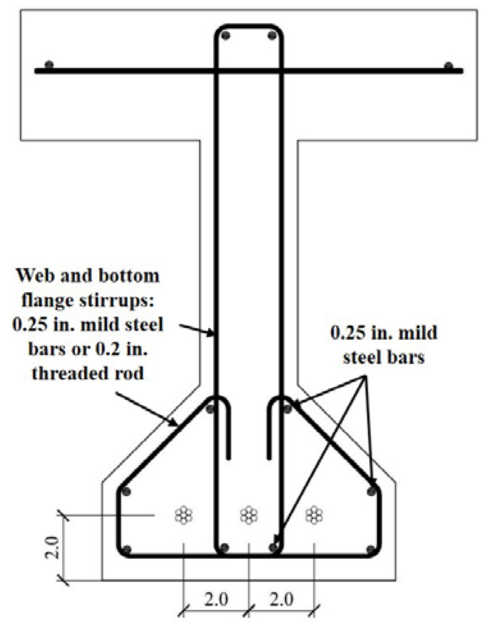

(b) Reinforcement detail (in.)

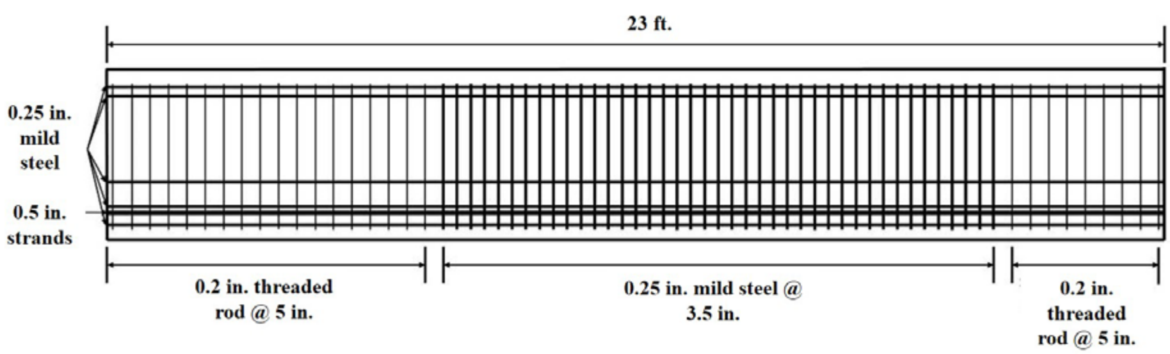

(c) Elevation view

Figure B.1. Small-scale beam cross-section and elevation.

APPENDIX C: DETAILS OF FULL-SCALE GIRDERS

This appendix contains figures of the cross-sectional dimensions of the full-scale girder and details of steel reinforcement.

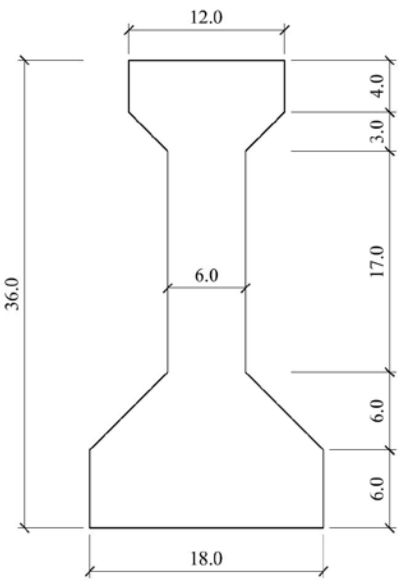

(a) Girder dimension (in.)

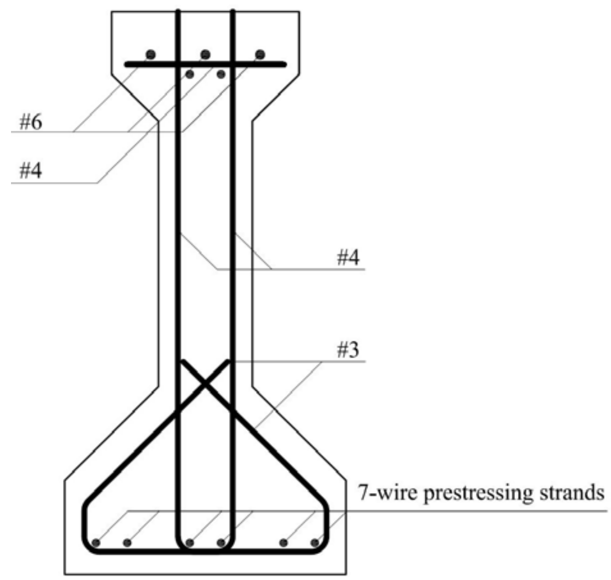

(b) Reinforcement details

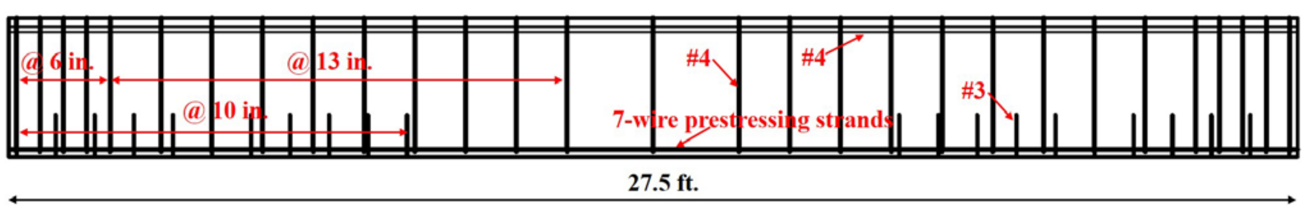

(c) Elevation view

Figure C.1. Full-scale girder cross-section and elevation.

Illinois Department of Transportation

ILLINOIS